

João Miguel Rosa Domingos

Geomagnetic and space weather variability modes in satellite data

Ph.D. thesis in Physics, Computational Physics,
supervised by Dr. Maria Alexandra Pais, Dr. Dominique Jault and Dr. Mioara Mandea
under a cooperation agreement for a joint supervision between the University of Coimbra and the University of Grenoble Alpes,
and presented to the Physics Department of the Faculty of Science and Technology of the University of Coimbra

December 2017



UNIVERSIDADE DE COIMBRA

Geomagnetic and space weather variability modes in satellite data

João Miguel Rosa Domingos

Department of Physics, University of Coimbra, Portugal

CITEUC, University of Coimbra, Portugal

ISTerre, University of Grenoble-Alpes, France

Under the supervision of

Dr. Alexandra Pais, University of Coimbra

Dr. Dominique Jault, University of Grenoble-Alpes

and Dr. Mioara Mandea, CNES

A thesis submitted for the degree of

Ph.D. in Physics, Computational Physics,

from the University of Coimbra

and the University of Grenoble-Alpes

December, 2017

"I was born not knowing and have had only a little time to change that here and there."

- Richard P. Feynman



UNIVERSIDADE DE COIMBRA



CENTRE NATIONAL D'ÉTUDES SPATIALES



Fundação para a Ciência e a Tecnologia
MINISTÉRIO DA CIÊNCIA, TECNOLOGIA E ENSINO SUPERIOR



Institut des Sciences de la Terre

Cofinanciado por:



UNIÃO EUROPEIA
Fundo Europeu
de Desenvolvimento Regional

Acknowledgments

This work would not have been possible, if not for all the people that helped me along the way. I would like to express my gratitude to all that made it possible. First to my supervisors, to Dr. Alexandra Pais, for constantly motivating me to continue and for endless patience and dedication even if at times I lacked them. To Dr. Dominique Jault, for making me feel welcome during my stay in Grenoble and always being ready to help, and to Dr. Mioara Manda, for always finding time to discuss and advise on the progress of the work, despite a very busy schedule. To everyone I had the pleasure to meet in Grenoble, who helped me adapt to the move. To all my friends in Coimbra, for providing the much needed distractions from work. To my family, for believing in me and inspiring me to aim higher, and especially to Magda, for your support and patience during this long endeavour. This would have been a much harder task if not for you.

Abstract

This work focus on the study of the South Atlantic Anomaly (SAA) of the main magnetic field from satellite data, aiming at identifying different sources of variability. This is done by first applying the Principal Component Analysis (PCA) method to particle flux and *dark noise* data and then to Virtual Observatories (VOs) time series constructed from satellite magnetic records. Particle flux data are provided by three POES NOAA satellites (10, 12 and 15) and the Jason-2 satellite. *Dark noise* data, which can be interpreted as a proxy to particle flux, are provided by the CALIOP lidar onboard the CALIPSO satellite. The magnetic field information is used in the form of time series for VOs, which were computed from both CHAMP and Swarm data as two separate datasets. The two different groups of data provide different views of the South Atlantic Anomaly. Applying PCA to particle flux data on the SAA produces interesting modes that can be related with specific physical processes involved with the anomaly. The main sources that drive these modes are the Earth's magnetic field and the Sun. The Sun's 11-year cycle is a well-known quasi-period of solar activity. This work shows how it clearly affects the evolution of the energetic particles trapped in the inner Van Allen belt, by modulating both their total number and their distribution among different L-shells. The way particles become trapped and move near-Earth is also dictated by the main magnetic field geometry and intensity and so a good understanding of its variation allows for a better description of the evolution

of these particles. The main magnetic field, with origin in the Earth's liquid core, is responsible for a slow drift of the anomaly, associated with the Westward drift of several features of the main field. Changing the frame of reference to that of the eccentric dipole, we were able to identify two separate modes associated with the variability of the solar activity. On longer time-scales, we also observed a linear trend in the spatial evolution of the particle flux. A global analysis of variability modes of the Earth's magnetic field has not been often addressed. This study also contributes to fill this gap. By decomposing satellite records of the magnetic field into PCA modes, we retrieved modes of internal origin and modes with large external contributions, with no a-priori considerations. An annual signal has been identified and associated with mainly external sources. It exhibits an interesting geometry dominated by a zonal quadrupolar geometry. As for the internal source, three separate modes were obtained from the longest time series analysed. The first of these modes explains most of the variability of the field and represents the mean secular variation. It is closely modelled by an eccentric tilted dipole moving away from the Earth's center and toward under East Asia. As this study shows, this simple model turns out to be a useful tool that can be used both on regional studies of the SAA and on global studies of the geomagnetic field.

Keywords: South Atlantic Anomaly, Swarm mission, geomagnetism, space weather.

Resumo

Este trabalho foca-se no estudo da Anomalia do Atlântico Sul (SAA) do campo magnético da Terra a partir de dados de satélite, procurando identificar diferentes fontes de variabilidade. Isto é feito aplicando o método de Análise em Componentes Principais (PCA), primeiro a dados de fluxo de partículas e *dark noise*, e depois a séries temporais de Observatórios Virtuais (VOs) construídas a partir de dados geomagnéticos de satélites. Os dados do fluxo de partículas provêm de três satélites POES NOAA (10, 12 e 15) e do satélite Jason-2. Os dados de *dark noise*, que podem ser interpretados como aproximações ao fluxo de partículas, são obtidos do lidar CALIOP a bordo do satélite CALIPSO. Os dados de campo magnético são usados na forma de séries temporais de VOs, calculadas a partir de dados do satélite CHAMP e da constelação de satélites Swarm em duas séries distintas. Os dois tipos de dados evidenciam diferentes aspectos da Anomalia do Atlântico Sul. Aplicar PCA a dados do fluxo de partículas na SAA produz modos interessantes, que podem ser relacionados com processos físicos específicos associados com a anomalia. O campo magnético da Terra e o Sol são os motores principais que influenciam estes modos. O ciclo de 11 anos do Sol é um quasi período de actividade solar bem conhecido. Este trabalho mostra como ele claramente afecta a evolução das partículas energéticas presas no anel de Van Allen interior, tanto a nível de quantidade como a nível da distribuição em diferentes camadas-L. A forma como as partículas ficam aprisionadas e se movimentam perto da

Terra também é descrita em termos da geometria e intensidade do campo magnético, pelo que um bom entendimento das variações destes factores permite uma melhor descrição da evolução destas partículas. O campo magnético com origem no núcleo líquido da Terra, é responsável por um lento deslocamento da anomalia, associado com o *Westward drift* de várias estruturas do campo. Mudando o referencial para o do dipolo excêntrico, conseguimos separar o efeito da variação do campo magnético da Terra e identificar dois modos distintos, associados à variabilidade da actividade do Sol. Em escalas de tempo mais longas, observamos uma tendência linear na evolução espacial do fluxo de partículas. Não existem muitos trabalhos que realizem uma análise global dos modos de variabilidade do campo magnético da Terra. Este trabalho também contribui para corrigir esta ausência. Decompondo os dados de satélite do campo magnético em modos PCA, obtivemos modos com origem interna e modos com grandes contribuições externas, não sendo necessário fazer considerações *a-priori*. Um sinal anual, em particular, foi identificado e associado maioritariamente a fontes externas. Exibe uma geometria interessante dominada por uma geometria quadrupolar zonal. Considerando fontes internas, três modos distintos foram obtidos a partir da série temporal mais longa. O primeiro destes modos explica a maior parte da variabilidade do campo e representa a variação secular média. Este modo é aproximadamente representado por um modelo de dipolo excêntrico inclinado, deslocando-se para longe do centro da Terra em direcção à Ásia. Como se mostra neste trabalho, este modelo simples é uma ferramenta útil tanto para estudo locais da SAA como para estudos globais do campo geomagnético.

Palavras chave: Anomalia do Atlântico Sul, missão Swarm, geomagnetismo, meteorologia espacial.

Résumé

Ce travail porte sur l'anomalie de l'Atlantique Sud (SAA anglais). Nous avons étudié cette anomalie du champ magnétique principal à partir de données satellitaires afin de mieux connaître les différentes sources de ses variations temporelles. Nous avons appliqué l'analyse en composantes principales (PCA) à des données de flux de particules, de bruit d'un lidar embarqué et à des séries temporelles d'observatoires magnétiques virtuels - séries construites à partir de mesures satellitaires du champ géomagnétique. Les données de flux de particules proviennent de trois satellites de la série POES de la NOAA (POES 10, 12 et 15) ainsi que du satellite Jason-2 du CNES et de la NASA. Nous utilisons aussi le bruit affectant le lidar CALIOP du mini-satellite CALIPSO (CNES/NASA) comme substitut au flux de particules chargées heurtant ce satellite. Pour l'information géomagnétique, deux jeux de données d'observatoires virtuels construits à partir d'enregistrements des satellites CHAMP et Swarm ont été utilisés. Ces deux ensembles différents de données apportent des éclairages complémentaires sur l'anomalie de l'Atlantique Sud. L'analyse en composantes principales des données de flux de particules a permis de distinguer différents modes de variabilité, dus au soleil d'une part et au champ magnétique principal d'autre part. Le cycle solaire de 11 ans affecte à la fois le flux total de particules énergétiques à l'aplomb de l'anomalie de l'Atlantique Sud et leur distribution dans les différentes ceintures de radiation internes. Le champ magnétique principal, qui provient du noyau liquide

de la Terre, est responsable d'une lente dérive de l'anomalie de l'Atlantique Sud et par ricochet de la région où il y a un flux intense de particules énergétiques. Une fois déconvolué le rôle du champ magnétique principal, on distingue deux composantes que l'on peut associer sans ambiguïté au cycle solaire. Sur des temps plus longs, nous avons finalement pu mettre en évidence une tendance dans le flux total de particules dans la région de l'Atlantique Sud. Peu d'analyses globales des modes de variabilité du champ interne ont été entreprises. Notre étude vise aussi à combler ce manque. L'analyse en composantes principales permet d'extraire jusqu'à trois modes d'origine interne et un mode annuel combinant contributions interne et externe. Ce dernier mode a une géométrie principalement quadrupolaire et zonale. Le premier des modes purement internes explique l'essentiel de la variabilité du champ et correspond à la variation séculaire moyenne au cours de l'intervalle de temps étudié. Il s'interprète principalement comme la variation de la partie du champ géomagnétique représentée par un dipôle qui serait de plus en plus décalé par rapport au centre de la Terre en direction de l'Asie du Sud-Est et qui serait aussi incliné par rapport à l'axe de rotation. Ainsi, ce simple modèle nous a été utile à la fois pour rendre compte du flux de particule au dessus de l'anomalie de l'Atlantique Sud et pour interpréter la variation du champ géomagnétique à l'échelle globale.

Mots clé: Anomalie de l'Atlantique Sud, mission Swarm, géomagnétisme, météo spatiale.

Contents

Contents	xv
List of Figures	xix
List of Tables	xxix
1 Introduction	1
1.1 Outline	1
1.2 The Sun	4
1.2.1 Structure	4
1.2.2 CMEs & Flares	6
1.3 Sun-Earth interaction	8
1.3.1 Interplanetary Magnetic Field	8
1.3.2 Solar wind and geomagnetic effectiveness	9
1.4 Near-Earth effects	12
1.4.1 Magnetospheric currents	12
1.4.2 Van Allen radiation belts	13
1.4.3 Ionospheric currents	22
1.4.4 Thermospheric Density	23
1.5 Core field	24
1.5.1 Geodynamo	24
1.5.2 Secular Variation	26
1.6 South Atlantic Anomaly (SAA)	27

2	Geomagnetic Field Models	31
2.1	Spherical Harmonics	32
2.2	CHAOS-6	35
2.3	COV-OBS	36
2.4	Comprehensive Models	36
2.5	Dipole approximations	37
3	Satellite Data and Proxies	41
3.1	Energetic Particles	42
3.1.1	POES NOAA	42
3.1.2	CALIOP	43
3.1.3	Jason-2	43
3.2	Geomagnetic Field	44
3.2.1	CHAMP	44
3.2.2	Swarm	46
3.3	Geomagnetic activity	48
3.3.1	Solar activity proxies	48
3.3.2	Geomagnetic indices	49
4	Principal Component Analysis (PCA)	53
4.1	Introduction	53
4.2	PCA applied on vector data	55
4.3	PCA modes with and without the mean	57
4.3.1	The vector of mean values is an eigenvector of \mathbf{C}_X . . .	60
4.3.2	The symmetric matrix of the mean is much larger than \mathbf{C}_X	60
5	Application of PCA to the SAA	63
5.1	Reference frames	63
5.1.1	Eccentric dipole reference frame	64
5.1.2	L-shell reference frame	64
5.2	South Atlantic Anomaly throughout the solar cycle	67
5.2.1	The first mode: modulation of the global flux of trapped protons by the solar cycle	71

5.2.2	The second mode: bipolar oscillation in the location of the maximum of proton flux	72
5.3	Discussion	74
6	The evolution of the SAA over the last 30 years	77
6.1	POES extended time series	77
6.2	Higher altitude data from Jason-2	86
6.3	Discussion	93
7	Application of PCA to the recent geomagnetic field	95
7.1	Virtual observatories (VO)	95
7.2	Data selection for PCA	97
7.3	Results	98
7.3.1	CHAMP	98
7.3.2	Swarm	102
7.3.3	Internal and External modes	105
7.4	Discussion	108
7.4.1	The linear mode from CHAMP and Swarm	110
7.4.2	The cubic polynomial mode from CHAMP	114
7.4.3	Annual oscillation modes from CHAMP and Swarm	115
8	Conclusions and Perspectives	119
	References	123
A	Application of PCA on simulated data	137
B	CHAMP and Swarm PCA modes	141

List of Figures

1.1	The structure of the Sun [Koskinen, 2011].	5
1.2	(a) The spectrum of total solar irradiance, compared with that of a 5770 K black body radiator. The blue dotted line shows the spectrum of radiation reaching the surface of the Earth. (b) The spectral variability of the irradiance defined as the fractional difference between the solar maximum and minimum values. The horizontal dashed line gives the corresponding value for the total solar irradiance that is the integral over all wavelengths ([Lockwood, 2005] after [Lean, 1991]).	7
1.3	Schematic representation of the magnetic field produced by the Sun [Luhmann et al., 2013].	8
1.4	The Sun’s heliospheric current sheet (Source: NASA).	9
1.5	A schematic diagram of the magnetosphere of the Earth. The incident solar wind plasma encounters the magnetic field of the Earth (at the magnetopause) which diverts plasma around it [Parks, 1991].	9
1.6	Geocentric solar magnetospheric (GSM) coordinate system, adapted from [Bhavnani and Vancour, 1991].	10
1.7	Convection in the magnetosphere when reconnection occurs. Reconnection at the tail end happens much further than represented, in the order of 20 to 100 Earth radius of distance. The bottom picture shows the motion of the numbered field lines at the ionosphere. [Koskinen, 2011]	11

1.8	A sketch of the close to Earth section of the magnetosphere (modified from [Kivelson and Russel, 1995]).	13
1.9	Representation of the Inner and Outer Van Allen radiation belts [Mitchell, 1994].	14
1.10	Representation of a particle's motion in a uniform magnetic field for $v_{\parallel} = 0$ [Prölss, 2004].	16
1.11	Particle motion in a uniform magnetic field for $v_{\parallel} \neq 0$. The pitch angle α describes the inclination of the helical trajectory to the magnetic field [Prölss, 2004].	17
1.12	Particle motion in a nonuniform magnetic field with a gradient along the magnetic field lines [Prölss, 2004].	18
1.13	Bounce motion in the Earth's dipole field [Prölss, 2004].	19
1.14	Particle motion in a nonuniform magnetic field. The field gradient is perpendicular to the magnetic field direction. For simplicity, the gradient is taken to be a sudden jump in the magnetic field strength at the dotted line, and the initial motion of the particles is assumed to be perpendicular to this discontinuity. [Prölss, 2004].	20
1.15	Composite motion of charge carriers in the inner magnetosphere. left panel: gyration and bouncing; right panel: bouncing and drift [Prölss, 2004].	21
1.16	Schematic representation of the main ionospheric currents (Source: GFZ Postdam).	23
1.17	Global mean neutral density at 400 km calculated from satellite drag in logarithmic scale [Solomon et al., 2013], and F10.7 solar index, representing the solar activity.	24
1.18	Magnetic field Intensity of Earth on June 2014. Map plotted from Swarm data (Source: ESA/DTU Space).	28
1.19	Map of 'Single Event Upsets' from the satellite Uosat-3 1990-1999 (Source: ESA).	29
2.1	Mauersberger-Lowes spectra for Earth, Mars, Moon, Jupiter and Mercury. [Hulot et al., 2010]	34

2.2	Schematic representation of how the position of the dipole was obtained (meridional plane on the left, equatorial plane on the right). Latitude calculation shown in the left and Longitude on the right. GN symbolises the Greenwich meridian.	37
2.3	Position of the 'SAA' according to three different approaches. CHAOS-6 minimum intensity for the period 1997-2014, the eccentric dipole antipodal position for the same period and POES maximum particle flux for the period 1986-2014. All show westward movement of the anomaly, with the initial position being on the right for all three plots. Note that POES position was obtained from real data, and has the superposed effect of the solar cycle which explains the rougher look of the trajectory.	38
2.4	Schematic representation of the calculation of a field line's L value.	39
3.1	Sunspot number over the 1990-2017 period (top), F10.7 index during the same period (middle) and thermospheric neutral density at 400 km (bottom) adapted from [Emmert, 2015]. Values shown are of monthly means.	49
3.2	Geomagnetic monthly means for the 1990-2017 period: Kp (top), Dst (middle) and RC (bottom).	50
3.3	Auroral Electrojet difference (AE) (top), westward electrojet (AL) (middle) and eastward electrojet (AU) (bottom) for the 1990-2017 period (monthly means).	51
5.1	POES particle flux data for December 2014 with eccentric dipole grid representation overlaid.	65
5.2	Contours of the particle flux anomaly (a). Representation of the L-shell reference frame construction process: removal of $L < 1.22$ contours as shown by dashed lines (b); new lines defined by interpolating lines in red (c); vertical axis created from thick red line of $ B _{min}$ together with other $ B $ contour lines (d).	67

5.3	The first three spatial patterns from the PCA analysis of POES data between 1998 and 2014, using the dipole reference frame and represented in the regular geographic grid. The x-axis is longitude and y-axis latitude. Percentage of variability, f_i , from the first to the last: 99.46, 0.38 and 0.11.	68
5.4	The first three spatial patterns from the PCA analysis of POES data between 1998 and 2014, using the L-shell reference frame and represented in the regular geographic grid. The x-axis is longitude and y-axis latitude. Percentage of variability, f_i , from the first to the last: 99.64, 0.28 and 0.02.	69
5.5	Time series corresponding to modes in figures 5.3 and 5.4 for the POES particle flux data. The x-axis is in years.	70
5.6	Modes amplitude for CALIOP dark noise data and POES particle flux data for the same time interval. The x-axis is in years.	71
5.7	Time series of the first PCA mode of POES L-shell reference frame and the thermospheric density. Atmospheric data retrieved from [Solomon et al., 2013].	72
5.8	Time series of the second mode for POES: comparison between a regular geographical grid (thinner dashed line), the dipole reference frame (thicker dashed line) and the L-shell reference frame (bold red line).	73
5.9	The spatial patterns from the second mode of the PCA analysis of POES data between 1998 and 2014, using the L-shell reference frame and represented in the $L-B_{min}$ grid. In this representation equation 5.2 is used, with i values ranging between 0-21 and the B_{step} equals 10.	74
6.1	POES 10,12,15 concatenated series with proton flux values normalized to 1. The vertical black lines represent the beginning and end of the time intervals of superimposed datasets.	79

- 6.2 First three PCA spatial modes for the POES 10,12,15 extended series. The x-axis is longitude and y-axis latitude. The fractions of variability of the three modes are 99.42%, 0.23% and 0.10% in order of importance. 80
- 6.3 First three PCA time series for the POES 10,12,15 extended series. The grey region is the envelope from scanning the factors $f_{15,12}$ and $f_{12,10}$ 81
- 6.4 Thermospheric density at 400 km altitude in logarithmic scale, obtained from orbit data for yearly running averages. Adapted from [Emmert, 2015]. 83
- 6.5 Results of the calculations detailed in equation 6.4. Oscillation results presented on the left and trend results on the right. Four different instants are presented, beginning of 1990, 1992, 1995 and 1998, in order. This corresponds to solar maxima, transition to solar minima, solar minima and transition to solar maxima, respectively. The cycle between high and low values repeats until the end of the available interval. The x-axis is longitude and y-axis latitude. 85
- 6.6 Jason-2 63 MeV spatial mode (left), Jason-2 292 MeV spatial mode (right). The x-axis is longitude and y-axis latitude. 88
- 6.7 Time series of the associated spatial modes in figure 6.6. Jason-2 63 MeV time series (left), Jason-2 292 MeV time series (right). Note that for both the first modes, the amplitude scale is smaller than POES (black), 50 % and 10% for mode 1 and 2 respectively. 89
- 6.8 Periods of the signals in figures 6.7. A period of 59.1 days is observed at both modes. For mode 1, a period of 11.33 to 12.95 months is observed, while for mode 2 the period is centered at 12.95 months. A period at 3.94 months for mode 2. All periods are marked with a black vertical line. 90

6.9	Annual signal from figures 6.7 shown for each year of the series. 63 MeV results shown on the left for mode 1 (red) and mode 2 (blue). 292 MeV results shown on the right for mode 1 (red) and mode 2 (blue).	91
6.10	Jason-2 63 MeV spatial mode (left), Jason-2 292 MeV spatial mode (right) , represented in the L - B_{min} grid. In this representation equation 5.2 is used, with i values ranging between 0-21 and the B_{step} equals to 10. In the bottom, POES 15 mode 2 is plotted in the same grid (see figure 5.9)	92
7.1	a) Distribution of the virtual observatories over the globe. The altitude of the VOs is 300km for CHAMP and 500 km for Swarm. Red dots represent the global coverage (total of 498), while blue squares represent the VOs in the sub-auroral region (total of 424).	97
7.2	Fraction of variability of standard PCA modes from CHAMP and associated standard deviation. The two plots are for PCA applied to the global spherical grid (red) or eliminating points at super-auroral latitudes (blue).	99
7.3	Representation of the spatial charts (B_r , B_θ and B_ϕ) of the first five modes of the PCA decomposition, for the global grid, using data from CHAMP. The color scale ranges from -5 to 5 (normalised values).	100
7.4	A_i^k time series corresponding to the spatial modes in figure 7.3, for the global grid (red) and sub-auroral grid (blue). . . .	101
7.5	Fraction of variability of standard PCA modes from Swarm and associated standard deviation. The two plots are for PCA applied to the global spherical grid (red) or eliminating points at super-auroral latitudes (blue).	102
7.6	Representation of the spatial charts (B_r , B_θ and B_ϕ) of the first four modes of the PCA decomposition, for the global grid, using data from Swarm. The color scale ranges from -5 to 5 (normalised values).	104

7.7	Time series corresponding to the spatial modes in figure 7.6, for global grid (red) and sub-auroral grid (blue).	105
7.8	Misfit values to a harmonic field fit, both internal (left) and external (right)	107
7.9	Spectra of the harmonic field models, internal (left) and external (right), fitted to different PCA modes.	108
7.10	Representation of the spatial charts (B_r , B_θ and B_ϕ) of the first mode of the PCA decomposition, for the global grid, using data from Swarm (top). Secular Variation due to translation and rotation of the eccentric dipole, for the first half of 2010 (bottom). The color scale ranges from -5 to 5 (normalised values) on the top row and from -100 to 100 (normalised values) on the bottom row.	113
7.11	Correlation between CHAMP (left) and Swarm (right) spatial features of PCA modes with the SV from the model based on the movement and rotation of the eccentric dipole. This was computed with the CHAOS-6 model, between 1997 and 2016.	113
7.12	Representation of the spatial charts (B_r , B_θ and B_ϕ) of the third mode of the PCA decomposition, for the global grid, using data from CHAMP. The color scale ranges from -5 to 5 (normalised values).	114
7.13	Representation of the spatial patterns (B_r , B_θ and B_ϕ) from CHAMP mode 4 (top), the results of the fit to CHAMP considering an external harmonic field (top-middle), Swarm mode 3 (bottom-middle) and the results of the fit to Swarm considering an external harmonic field (bottom). The color scale ranges from -5 to 5 (normalised values).	116
A.1	First three PCA spatial features from the gaussian test models. Drift (D) only test (top), intensity (I) only test (top middle), size (S) only mode (bottom middle) and all three behaviours (D-I-S) together (bottom).	138

A.2	First three PCA time series from the gaussian test models. Drift (D) only test (top), intensity (I) only test (top middle), size (S) only mode (bottom middle) and all three behaviours (D-I-S) together (bottom).	140
B.1	Representation of the spatial features (B_r (top two rows), B_θ (middle two rows) and B_ϕ (bottom two rows)) of PCA mode 1 for the global (1 st , 3 rd and 5 th rows) and sub-auroral (2 nd , 4 th and 6 th rows) grids from CHAMP data.	142
B.2	Representation of the spatial features (B_r (top two rows), B_θ (middle two rows) and B_ϕ (bottom two rows)) of PCA mode 2 for the global (1 st , 3 rd and 5 th rows) and sub-auroral (2 nd , 4 th and 6 th rows) grids from CHAMP data.	143
B.3	Representation of the spatial features (B_r (top two rows), B_θ (middle two rows) and B_ϕ (bottom two rows)) of PCA mode 3 for the global (1 st , 3 rd and 5 th rows) and sub-auroral (2 nd , 4 th and 6 th rows) grids from CHAMP data.	144
B.4	Representation of the spatial features (B_r (top two rows), B_θ (middle two rows) and B_ϕ (bottom two rows)) of PCA mode 4 for the global (1 st , 3 rd and 5 th rows) and sub-auroral (2 nd , 4 th and 6 th rows) grids from CHAMP data.	145
B.5	Representation of the spatial features (B_r (top two rows), B_θ (middle two rows) and B_ϕ (bottom two rows)) of PCA mode 5 for the global (1 st , 3 rd and 5 th rows) and sub-auroral (2 nd , 4 th and 6 th rows) grids from CHAMP data.	146
B.6	Representation of the spatial features (B_r (top two rows), B_θ (middle two rows) and B_ϕ (bottom two rows)) of PCA mode 1 for the global (1 st , 3 rd and 5 th rows) and sub-auroral (2 nd , 4 th and 6 th rows) grids from Swarm data.	147
B.7	Representation of the spatial features (B_r (top two rows), B_θ (middle two rows) and B_ϕ (bottom two rows)) of PCA mode 2 for the global (1 st , 3 rd and 5 th rows) and sub-auroral (2 nd , 4 th and 6 th rows) grids from Swarm data.	148

B.8 Representation of the spatial features (B_r (top two rows), B_θ (middle two rows) and B_ϕ (bottom two rows)) of PCA mode 3 for the global (1st, 3rd and 5th rows) and sub-auroral (2nd, 4th and 6th rows) grids from Swarm data. 149

B.9 Representation of the spatial features (B_r (top two rows), B_θ (middle two rows) and B_ϕ (bottom two rows)) of PCA mode 4 for the global (1st, 3rd and 5th rows) and sub-auroral (2nd, 4th and 6th rows) grids from Swarm data. 150

List of Tables

1.1	Comparison of the gyration (τ_G), oscillation/bounce (τ_O) and drift (τ_D) periods for representative particle populations in the inner magnetosphere. Each L value corresponds to a different magnetic field value. *(multiplication factor for the periods) Adapted from [Prölss, 2004].	21
7.1	Normalising factors of PC time series for all five modes of CHAMP PCA decomposition (See equation 7.1).	102
7.2	Normalising factors of PC time series for all four modes of Swarm PCA decomposition.	103
7.3	Misfit values from internal and external SH fit of the PCA modes, for both CHAMP and Swarm.	106

Chapter 1

Introduction

1.1 Outline

Human activities have long since depended on space infrastructures that provide us with data that support everyday technologies and innovative research as well.

There were more than 4000 satellites [UNOOSA, 2017] orbiting the Earth as of 2016. They facilitate communications, provide us with navigation systems such as GMSS (Global mobile satellite system), and monitor our environment and weather in order to make the Earth an easier world to live in. Predicting the evolution of a meteorological storm, for example, helps save lives. These satellites are helpful if they provide high-accuracy information. This depends on the quality of the spacecraft itself, which we can control, to the external effects that might affect their functioning.

Space weather (SW) is the term used to describe the complex interconnection of magnetic fields and high energy particles coming from the Sun in the near-Earth space. The Sun-Earth's environment can suffer rapid and powerful changes and affect the human activity. Due to the intrinsic vulnerability of the electronic systems to magnetic fields and charged particles, space weather effects have become a great cause of concern.

Our complex web of orbiting satellites spreads over a region where ener-

getic particles circulate, creating a possible hazard for the satellites. In most cases, the risk is low, as the absorbing capacity of the atmosphere and the shielding of the instruments is more than sufficient to protect them. But in certain conditions, the flux of energetic particles can increase to dangerous levels and damage important electronic components on-board the satellites. In the era of space exploration there are continuously astronauts in orbit on-board of the International Space Station (ISS), and a direct risk exists for their health due to the biological effects of radiation. A more indirect risk for human life may occur if by any chance a manned space vessel is struck by a sufficiently energetic particle in the right conditions to disrupt a vital piece of equipment. To possibly predict and avoid such events, we need to investigate them.

Naturally, at higher altitudes of the atmosphere, the danger to satellites and humans is higher, but it is also significant at the Earth's surface. The main source of space weather threat is the Sun. With a relatively quiet activity, it can develop flares and coronal mass ejections (CME) that project great amounts of plasma into outer space. If the Earth is in its path, serious consequences can be envisaged.

A well-known event with strong consequences was the 1989 geomagnetic storm. On the 13th of March, a CME, led to a severe geomagnetic storm that hit the Earth four days later. The storm affected the Earth magnetic field so much that the sudden variations in the Québec region tripped circuit breakers on Hydro-Québec's power grid. This led to a nine hour blackout [Kappenman, 2012], a very serious and costly consequence of a space weather event. As would be expected, on this day, several satellites, which were at greater risk, were bombarded by an increased flux of energetic particles. For some, small anomalies were detected, while others, such as the GOES weather satellites had their communications cut off leading to a loss of data.

The strongest recorded event was in 1859 [Shea and Smart, 2006], the most powerful geomagnetic storm we have knowledge of, known as the Carrington event. It was caused by a CME. If something of the same magnitude happened today, studies show that it would severely cripple our heavily electronically dependent society. Luckily, no other CME of that size has hit

Earth since.

The magnetic field of Earth acts as an efficient shield, and it provides much protection from external events. But as we saw, solitary events from the Sun can be devastating for Earth if the right (or wrong in this case) conditions are met. The ability to control these events is far beyond us and we need to understand and predict them. A predictive ability of such events could lead to a timely warning system which could prevent major damages to both satellites and ground infrastructures.

The effect of the Sun's activity on Earth depends on the interaction of the Sun's magnetic field with the Earth's one. So it is important to monitor the Sun's activity and the geomagnetic field for understanding the space weather events. A particularly feature of the geomagnetic field is the so-called South Atlantic Anomaly (SAA), currently covering a region over the Southern Atlantic and South America, where the magnetic field is the weakest. A weaker magnetic field offers less resistance to harmful energetic particles. A large number of the effects of space weather seen on orbiting satellites occur in this region as it allows for more energetic particles to penetrate deep into Earth's environment.

The SAA is therefore a prime location to study the effects of space weather. For decades we have acquired information on particle flux levels from satellites. This information, coupled with an understanding of the geomagnetic field and the interplanetary magnetic field (IMF) powered by the Sun, gives us the necessary tools to study space weather events.

The most recent mission to space with the intent to study the magnetic field is the Swarm mission. It is composed of a cluster of three satellites and provides the most detailed information about the geomagnetic field to date. The study of the geomagnetic field using satellite data has been going on for decades since the 1960s [Olsen and Stolle, 2012]. Swarm adds to this long record with very accurate data that allow for a better separation of the internal and external components of the Earth's magnetic field. The external components vary quickly and require fast coverage of space with good time resolution and good precision, both available with Swarm. The study of space weather partly relies on the knowledge of the main geomagnetic field

and Swarm is the best effort in understanding every aspect of it.

In this study, we try to combine information from two different scientific areas. Space weather requires the study of both the geomagnetic field and of particle physics, two large areas of science which could only benefit from each other perspectives on this subject. The SAA has been widely investigated, but often, either the geomagnetic aspect of the anomaly or the particle flux anomaly was studied and not the two simultaneously. Some authors bridge this gap, and here, we shall follow their lead.

The thesis is organised as follows: the first chapter makes a general introduction of the Sun-Earth system with all appropriate definitions. The second chapter focuses on the geomagnetic field models used for this work. In the third chapter we introduce the satellite data analysed, and chapter four details the method used to decompose the data. In chapter five we begin to show the results obtained. Here we reproduced our published Principal Component Analysis (PCA) of a particle flux record from a single satellite. Chapter six deals also with particle flux using first a combination of satellite records to construct a long series and second a record from a satellite orbiting at an higher altitude above the Earth's surface. Chapter seven details the PCA analysis of magnetic field data and chapter eight concludes the work.

1.2 The Sun

1.2.1 Structure

The great giant of the solar system, the Sun, regulates the Earth's environment. It provides warmth to sustain the Earth and those who inhabit it, but it also affects us in a less obvious way. The Sun is the strongest contributor to the magnetic field we observe near Earth, other than the one produced by the Earth's liquid core. The Sun's magnetic field is generated by a dynamo process, similar to the Earth's, but in the case of the Sun, the convection of hot plasma fuels it.

In figure 1.1 we can see the simplified structure of the Sun. The source of its energy comes from nuclear reactions in the core, which spans over a quarter of the radius. Here, pressure can rise to 2×10^{16} Pa and temperature to about 1.5×10^7 K. Through radiative diffusion, energy from the core is propagated outwards to the surface. This is a very slow process, due to a high density of the radiative zone, taking around 170000 years for photons to travel 2 light seconds [Koskinen, 2011]. Above the radiative zone where this slow travel takes place, there is the convective zone. Here, energy transfer is much faster and most of the Sun's activity is generated. In this region the magnetic field of the Sun is produced due to the motion of plasma. The complex and sometimes chaotic behaviour of this layer of the Sun is the cause of the unpredictability of its activity with some impressive phenomena, as the coronal mass ejections (CME) and solar flares, due to the changing magnetic field produced by the plasma shell. Above the Convective zone, the

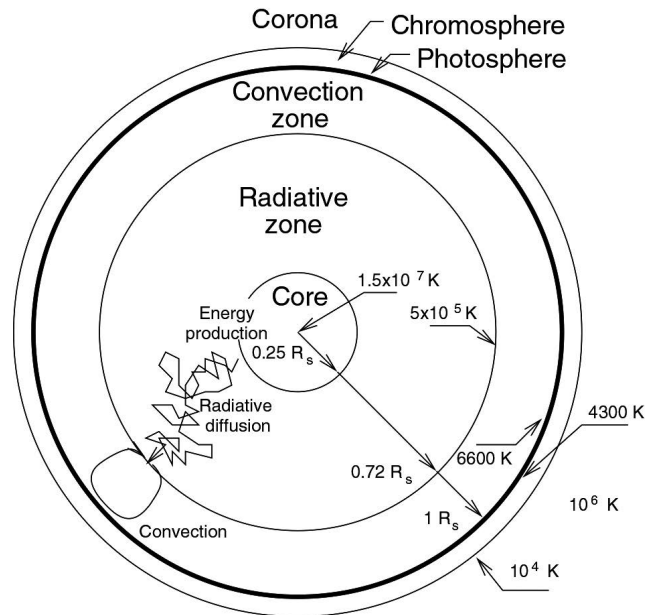


Figure 1.1 – The structure of the Sun [Koskinen, 2011].

Photosphere, is a region where the energy brought upwards from the core is radiated away. The temperature at the top of the photosphere is around 6000 K. Above the Photosphere, the Chromosphere is a region where the

temperature rises to values of the order of 25000 K. The last layer called Corona is characterised by temperatures reaching values of 10^6 K and an extremely low density [Koskinen, 2011]. The plasma in the Corona region is a big contributor to space weather effects.

1.2.2 CMEs & Flares

The plasma in the corona region is for most of the time contained but during certain conditions it can be pushed outwards and into a state where it escapes the strong gravitational field of the Sun. These are what are known as CMEs. CMEs occur when magnetic field lines breach the surface of the Sun and carry with them plasma. This plasma can then be ejected.

The outward movement of plasma from the Sun is known as solar wind, it occurs constantly through holes in the corona, but stronger bursts happen due to CMEs. It can dangerously affect the Earth if the CME event is strong enough. Solar flares are another kind of emissions from the Sun that affect the Earth. Instead of plasma ejection, they are comprised mainly of magnetic field disturbances and bursts of electromagnetic radiation (ranging from radio waves to γ -rays), which can reach the Earth. Solar flares and CMEs are often connected but not necessarily (e.g. [Koskinen, 2011]).

Plasma movements, in the Convective zone of the Sun produce magnetic field, as any charged particle or body would. The plasma from the solar wind is not different and it creates and drags across space this magnetic field. This is known as the Interplanetary Magnetic Field (IMF).

On decade time scales, we can identify a periodical variation of around 11 years in the strength of the solar activity. When counting sun spots, a very common proxy for the amount of solar activity, this period is quite clear. Longer than this, we can consider a 22-year cycle, as every 11 years the polarity of the Sun reverses. In figure 1.2 we can see the irradiance variability during the 11-year solar-cycle period. In the UV edge of the spectrum, we can see that the variability over the solar cycle is much larger than in the

visible and infrared region, up to a factor of 10 to 1000.

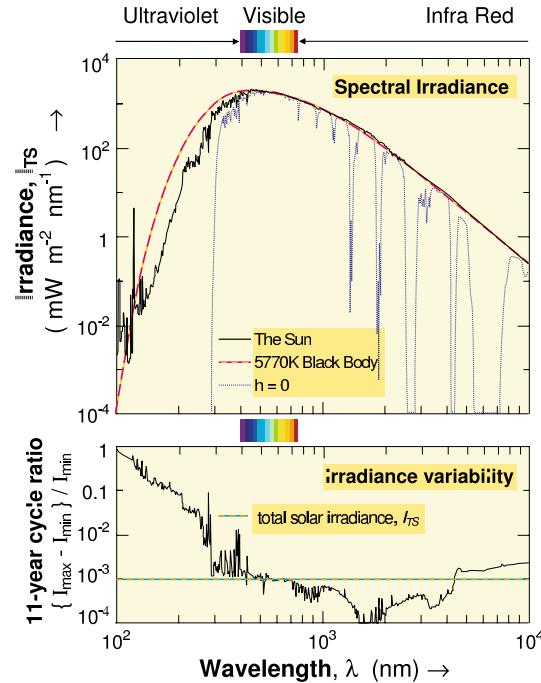


Figure 1.2 – (a) The spectrum of total solar irradiance, compared with that of a 5770 K black body radiator. The blue dotted line shows the spectrum of radiation reaching the surface of the Earth. (b) The spectral variability of the irradiance defined as the fractional difference between the solar maximum and minimum values. The horizontal dashed line gives the corresponding value for the total solar irradiance that is the integral over all wavelengths ([Lockwood, 2005] after [Lean, 1991]).

These highly energetic UV rays are absorbed in the thermosphere, and are responsible for the variation in density in the upper atmosphere. The ionosphere, which is the partially ionized part of the Atmosphere, including within it the thermosphere, has one of its sources in the same highly energetic UV rays, by means of photoionization. In contrast, due to the infrared variance being low in comparison, we do not see a significant effect in the temperature of the globe during the solar cycle. We can realistically study the long-term effects from the Sun. The unexpected events, such as solar flares and CMEs are important, but hard to predict, as they can occur at any time. They can distort the outer layer of the magnetic field, the magnetosphere can be compressed and plasma particles can penetrate deeper into the Earth's

environment. As important as they are, they are occasional events, and so, they do not provide much information on the long-term evolution of the system.

1.3 Sun-Earth interaction

1.3.1 Interplanetary Magnetic Field

The IMF is the component of the solar magnetic field that spans towards the solar system planets and therefore directly interacts with the Earth's magnetic field. The flow of the plasma out from the Sun creates a sheet-like current distribution close to the plane of the Sun's equator as can be seen in figures 1.3 and 1.4.

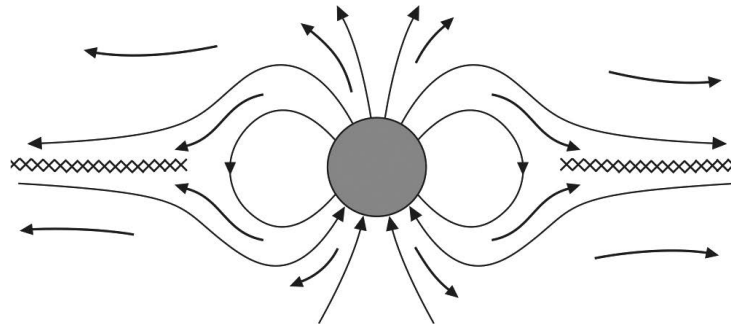


Figure 1.3 – Schematic representation of the magnetic field produced by the Sun [Luhmann et al., 2013].

The sheet like geometry of the IMF is due to the rotation of plasma around the Sun, which creates outward directed magnetic field lines on one side of the plasma sheet and inward on the other side [Koskinen, 2011]. In figure 1.4 we can see the current sheet produced by the moving plasma. It is not a straight plane, it has ripples that move around the Sun, creating the same effect in the field it produces. Occasional bursts from the Sun, CMEs that perturb this sheet field, quickly introduce large amounts of plasma and therefore magnetic field variation across the IMF.

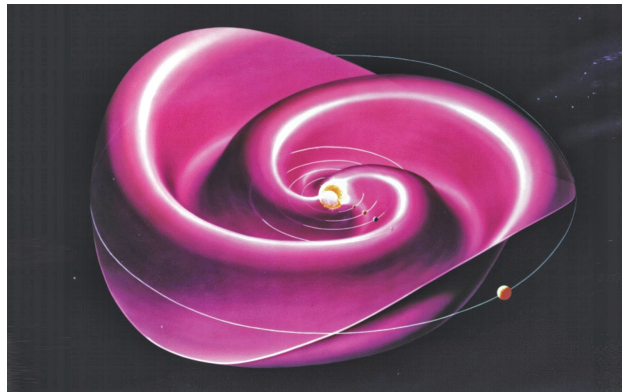


Figure 1.4 – The Sun’s heliospheric current sheet (Source: NASA).

1.3.2 Solar wind and geomagnetic effectiveness

The ejection of plasma from the Sun, either by CMEs or other events constitutes the solar wind. In the path of the solar plasma stands also the Earth. Its magnetic field is very much affected by the solar wind and the IMF. In figure 1.5 we can see how much the geomagnetic field is distorted due to the interaction with the IMF. There, a balance is reached between the pressure of the solar wind and the pressure of the geomagnetic field, which maintains some equilibrium.

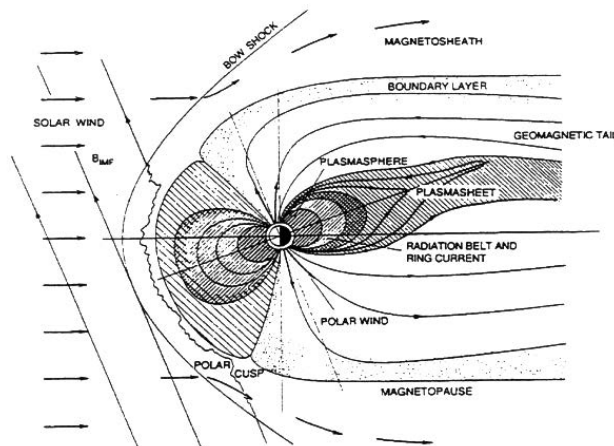


Figure 1.5 – A schematic diagram of the magnetosphere of the Earth. The incident solar wind plasma encounters the magnetic field of the Earth (at the magnetopause) which diverts plasma around it [Parks, 1991].

The first important interaction of the solar wind plasma is with the magnetopause (see figure 1.5), the outer most layer of Earth's magnetic field and the one that deflects most of the particles from solar wind. This is done by the formation of a bowshock upstream from the magnetosphere.

In certain conditions, large amounts of solar wind plasma can penetrate into the magnetosphere. This happens when the IMF carried by the solar wind has a significant component with opposite direction to the magnetospheric field lines [Koskinen, 2011].

The coordinate system considered here to describe the IMF is the Geocentric Solar Magnetospheric (GSM) coordinate system (see figure 1.6). In this system, the X-axis is pointing from the center of Earth to the Sun. The Z-axis stands in the plane of the X-axis and the geomagnetic axis of the Earth, being perpendicular to the X-axis. Finally, the Y-axis is perpendicular to both X and Z-axis, as can be seen in figure 1.6.

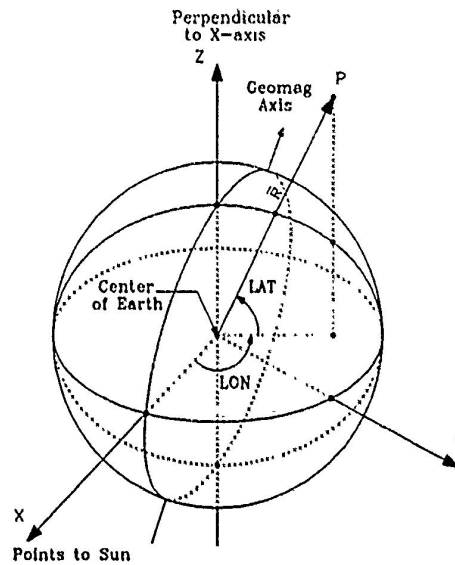


Figure 1.6 – Geocentric solar magnetospheric (GSM) coordinate system, adapted from [Bhavnani and Vancour, 1991].

In figure 1.7 we can see a representation of the reconnection effect, where magnetic field lines from originally distinct magnetic domains are spliced. The two field lines (1 and 1') connect and separate in a different geometry, allowing for plasma to be incorporated into the near Earth's system. This is

only possible if the IMF has the correct orientation. If the Z component of the IMF points southward, the chance of reconnection is greater, as the field lines from Earth point northward, as is illustrated in figure 1.7, and localised diffusion gets very high. The same figure shows how reconnection moves flux from the dayside to the nightside, following the stages 1 to 9. Field lines from the IMF and Earth reconnect (1-2), creating field lines that connect the solar wind directly with the ionosphere. These are called open field lines. The new field lines move to the nightside (3-5), where they reconnect again (6). The next steps (7-9) complete the circulation of the field lines by restoring the closed field lines and moving them to the front end of the magnetosphere. These open field lines allow for solar wind particles to move into the ionosphere and magnetosphere, in the polar cap area, as can be seen in the bottom part of figure 1.7. The precipitation of energetic particles caused by tail reconnection in the area of the poles, is the source of the aurorae which can be seen in the high latitude skies.

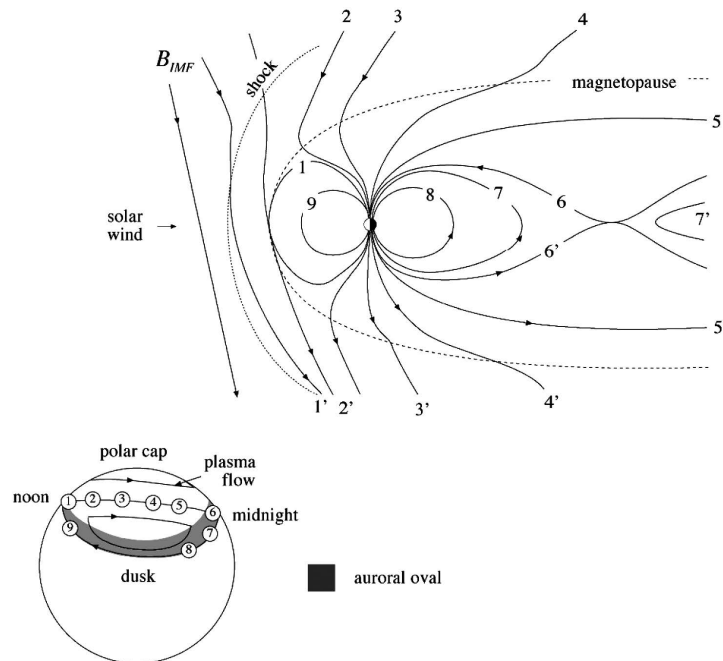


Figure 1.7 – Convection in the magnetosphere when reconnection occurs. Reconnection at the tail end happens much further than represented, in the order of 20 to 100 Earth radius of distance. The bottom picture shows the motion of the numbered field lines at the ionosphere. [Koskinen, 2011]

1.4 Near-Earth effects

The component of the geomagnetic field due to currents circulating in the magnetosphere and the ionosphere is called the external field. External currents are powered by the solar wind, photoionisation and photodissociation.

1.4.1 Magnetospheric currents

The magnetosphere is a region around the Earth where the geomagnetic field exists and determines the motion of the charged particles. We can also define the limit of the magnetosphere (magnetopause) as the region where the solar wind pressure balances the geomagnetic field pressure (equation 1.1) and the normal component of the geomagnetic field is zero (equation 1.2):

$$\frac{\mathbf{B}^2}{2\mu_0} = \rho_{sw} \mathbf{v}_{sw}^2 \quad (1.1)$$

$$B_n = 0 \quad (1.2)$$

where \mathbf{B} is the geomagnetic field, ρ_{sw} is the density of the solar wind and \mathbf{v}_{sw} is the solar wind velocity (see [Kallenrode, 2004] and [Prölss, 2004] for a more correct description).

The magnetosphere deflects most of the particles that are ejected towards the Earth. The tail of the magnetosphere extends further into the dark side as it is pushed away by the solar wind. We can also identify several currents that exist in the magnetosphere region. As the IMF interacts with the magnetosphere, it introduces plasma, and it is this addition and transfer of plasma that fuels magnetospheric currents. The ring current creating the greatest measurable effects at mid-latitudes on the Earth, exists in the equatorial plane of the geomagnetic dipole. After this, the magnetopause surface currents (or Chapman-Ferraro currents) and the cross-trail current are the most dominant [Koskinen, 2011]. There are also field aligned currents which are currents coupling the ionosphere and magnetosphere at high latitudes. They are crucial in the transfer of plasma between these two regions. When plasma is brought into the magnetosphere, it can be guided along the

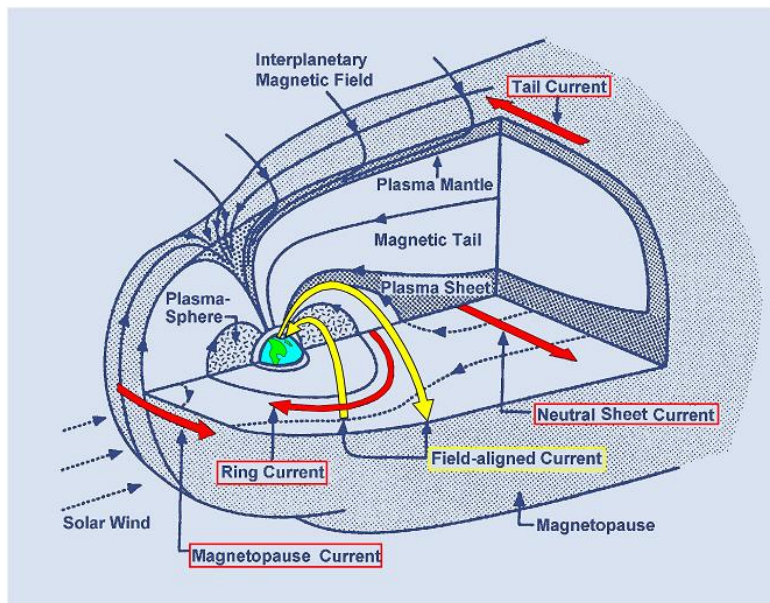


Figure 1.8 – A sketch of the close to Earth section of the magnetosphere (modified from [Kivelson and Russel, 1995]).

magnetic field lines, spiralling, within the magnetosphere all the way to the ionosphere, in the polar regions.

The most studied magnetospheric current is the ring current because of its simple geometry and relatively high intensity. The ring current coexists with the Van Allen radiation belts (see below), despite being composed of different energy particles coming from the sunward convection of the tail plasma.

1.4.2 Van Allen radiation belts

There are two main shells that encircle the Earth at two different levels where energetic particles are located, called Van Allen radiation belts (see figure 1.9). The inner belt at a distance of 1.15 to $3 R_e$ at the magnetic equator, dominated by the presence of protons between 0.1 and 40 MeV and also energetic electrons. The outer belt, at a distance of $> 4 R_e$ is constituted mainly of electrons in the keV to MeV energy range.

From interaction with magnetic fields, energetic particles may become trapped in more or less defined regions of space, if no outside force acts upon

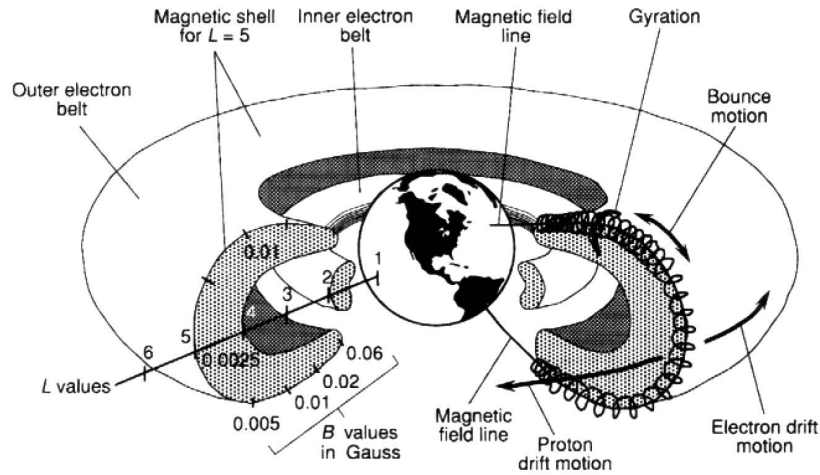


Figure 1.9 – Representation of the Inner and Outer Van Allen radiation belts [Mitchell, 1994].

them. These shells are constantly being refilled with particles coming from the Sun as plasma, or created by beta decay of neutrons in the upper atmosphere, and constantly losing particles by several different effects. The Van Allen radiation belts shield the Earth surface from incoming high energetic particles, by either trapping or deviating them.

Two main sources of particles feed the inner belt. The first one is the Sun, which constantly bombards the Earth with energetic particles in the form of solar wind. Some of these particles will become trapped and add to the belt's population. The other source is cosmic radiation. The highly energetic cosmic rays interact with atmospheric particles. Depending on the energy level and direction, the resulting particles of this collision can become trapped by the magnetic field and become part of the belts [Selesnick et al., 2014]. The outer belt is fed by the solar wind, but the energetic particles go through the reconnection process before being introduced into this region.

The belts population is constantly decreasing as particles collide with the neutral atmosphere and are ejected, but the constant supply from exterior sources, provides quick refilling. Both belts are constituted of fast moving particles that on top of spiralling along the magnetic field lines also drift across field lines along the planet.

Using the guiding center approximation [Roederer and Zhang, 2014] we can describe qualitatively the motion of a charged particle in the Earth's magnetic field. Here, we closely follow [Prölss, 2004]. We first need to identify the forces acting on each particle. These are, a velocity dependent magnetic force (\mathbf{F}_B) and velocity independent external forces (\mathbf{F}_j). In this scenario we neglect interactions with other particles. We need solutions for the equation of motion,

$$m \frac{d\mathbf{v}}{dt} = \mathbf{F}_j + q(\mathbf{v} \times \mathbf{B}) \quad (1.3)$$

where m is the mass of the particle, \mathbf{v} is the velocity, q the charge and \mathbf{B} the surrounding magnetic field. We first separate it into parallel (\parallel) and perpendicular (\perp) components in relation to \mathbf{B} .

$$m \frac{d\mathbf{v}_{\parallel}}{dt} = \mathbf{F}_{j\parallel} \quad (1.4)$$

$$m \frac{d\mathbf{v}_{\perp}}{dt} = \mathbf{F}_{j\perp} + q(\mathbf{v}_{\perp} \times \mathbf{B}) \quad (1.5)$$

Equation 1.4 is the equation of motion valid for neutral gas particles as well as charged. If external forces are time independent, we have:

$$\mathbf{v}_{\parallel}(t) = \mathbf{v}_{\parallel}(t_0) + \frac{\mathbf{F}_{j\parallel}}{m}(t - t_0). \quad (1.6)$$

The solution to equation 1.5 is more difficult to obtain as it depends on the configuration of the magnetic field. This is because the magnitude and direction of the magnetic force are functions of velocity. This prevents a direct separation of variables.

To tackle this problem, we need to separate the total motion into four individual motions. Each of the individual motions has a very different time scale and so we can linearly add them later.

The individual motions are: Gyration: ($\mathbf{F}_{j\perp} = 0$, \mathbf{B} uniform); Oscillatory bounce motion from one hemisphere to the other: ($\mathbf{F}_{j\perp} = 0$, $\nabla B \parallel \mathbf{B}$); Gradient drift: ($\mathbf{F}_{j\perp} = 0$, $\nabla B \perp \mathbf{B}$); External force drift: ($\mathbf{F}_{j\perp} \neq 0$, \mathbf{B} uniform).

Gyration (cyclotron motion)

Considering $\mathbf{F}_{j\perp} = 0$ and \mathbf{B} uniform, the magnetic field produces an acceleration of charged particles perpendicular to their direction of motion without changing the magnitude of the velocity. In this case $\mathbf{v}_{\parallel} = 0$. Equation 1.5 becomes:

$$m \frac{d\mathbf{v}_{\perp}}{dt} = q(\mathbf{v}_{\perp} \times \mathbf{B}) \quad (1.7)$$

with

$$\mathbf{F}_{\mathbf{B}} = q(\mathbf{v}_{\perp} \times \mathbf{B}). \quad (1.8)$$

The magnetic force $\mathbf{F}_{\mathbf{B}}$ acts as a centripetal force that forces the particles into a spiral orbit with increasingly larger curvature. This results in a circular motion as can be seen in figure 1.10.

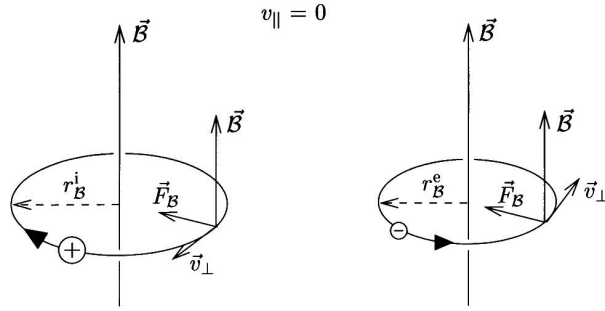


Figure 1.10 – Representation of a particle's motion in a uniform magnetic field for $v_{\parallel} = 0$ [Prölss, 2004].

The radius of the orbit can be obtained by equating,

$$|q|v_{\perp}B = mv_{\perp}^2/r_B, \quad (1.9)$$

and the gyroradius or Larmor radius is then:

$$r_B = \frac{mv_{\perp}}{|q|B}. \quad (1.10)$$

The circulation direction is dependent on the charge sign of the particle as we can see in figure 1.10. We can also compute the period associated with

this orbit, which is:

$$\tau_B = \frac{2\pi r_B}{v_\perp} = 2\pi \frac{m}{|q|B}. \quad (1.11)$$

We consider now the case where the particle also has a velocity parallel to the magnetic field ($v_\parallel \neq 0$). As the parallel velocity component is not affected by the magnetic field, we can linearly add it onto the gyromotion described before. This added motion can be seen in figure 1.11.

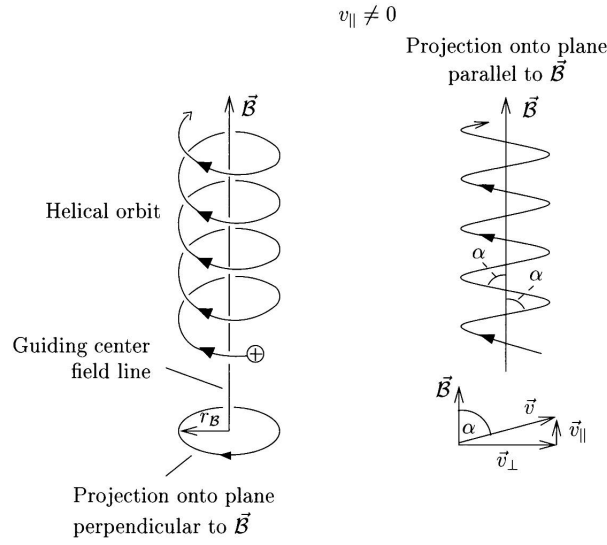


Figure 1.11 – Particle motion in a uniform magnetic field for $v_\parallel \neq 0$. The pitch angle α describes the inclination of the helical trajectory to the magnetic field [Prölss, 2004].

The inclination of the trajectory in relation to the magnetic field line is called the pitch angle (α). This angle allows us to write the two components of the velocity as:

$$v_\perp = v \sin \alpha \quad , \quad v_\parallel = v \cos \alpha. \quad (1.12)$$

Oscillatory motion

Considering now the case where $\mathbf{F}_j = 0$ and $\nabla B \parallel \mathbf{B}$, which represents a nonuniform magnetic field, with an intensity gradient along the field lines. In figure 1.12 we can see the effects on a charged particle of such a field.

The particle is now passing through regions where the magnetic field has both parallel and perpendicular components in relation to the guiding center

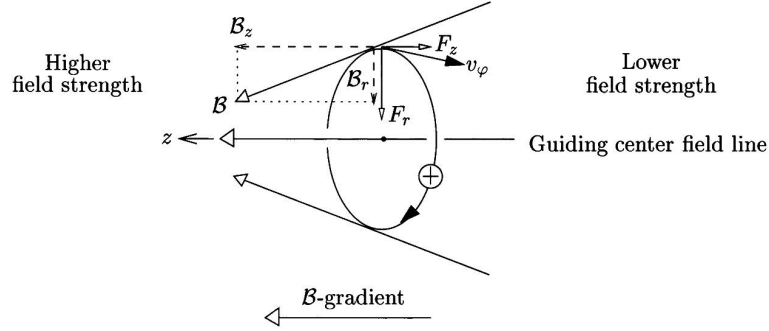


Figure 1.12 – Particle motion in a nonuniform magnetic field with a gradient along the magnetic field lines [Prölss, 2004].

field line. This in turn produces forces parallel and perpendicular to the guiding field line. The perpendicular force (F_r) is the source of the gyration and the parallel force (F_z) produces acceleration in the direction of the field lines, from the higher magnetic field strength to the lower. Using the notation from fig 1.12 in cylindrical coordinates, we can write this force as,

$$F_z = |q|v_\phi B_r. \quad (1.13)$$

From the Maxwell equation ($\nabla \cdot \mathbf{B} = 0$) we can write in cylindrical coordinates:

$$\nabla \cdot \mathbf{B} = \frac{1}{r} \frac{\partial}{\partial r}(rB_r) + \frac{\partial B_z}{\partial z} = 0. \quad (1.14)$$

Multiplying equation 1.14 by r and integrating, leads to

$$\int_0^r \frac{\partial}{\partial r'}(r'B_r)dr' = - \int_0^r r' \frac{\partial B_z}{\partial z} dr'. \quad (1.15)$$

Considering that $\partial B_z / \partial z$ is independent of r ,

$$B_r(r) = -\frac{r}{2} \frac{dB_z}{dz}. \quad (1.16)$$

Calculated at $r = r_B$ it becomes,

$$B_r(r_B) = -\frac{mv_\phi}{2|q|B_z} \frac{dB_z}{dz} \simeq -\frac{mv_\phi}{2|q|B} \frac{dB}{dz}. \quad (1.17)$$

Assuming that B_r is only a small perturbation, B_z can be approximated to B . The field-aligned component of the magnetic force is,

$$F_z = -\frac{mv_\phi^2}{2} \frac{1}{B} \frac{dB}{dz}, \quad (1.18)$$

or in vectorial form:

$$\mathbf{F}_{\parallel}^{\text{gr}} = -\frac{E_{\perp}}{B} \nabla_{\parallel} B. \quad (1.19)$$

where E_{\perp} is the kinetic energy. In figure 1.13 the resulting effect of these forces is presented in a simple dipolar field.

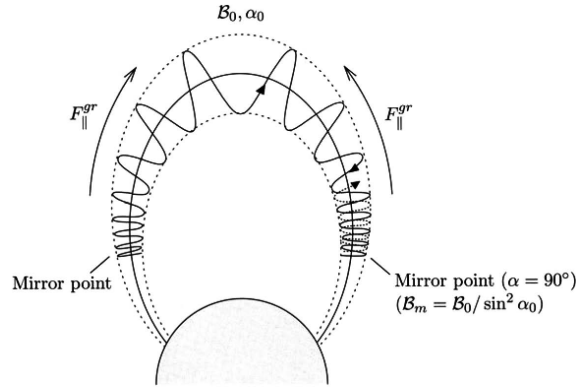


Figure 1.13 – Bounce motion in the Earth's dipole field [Prölss, 2004].

The particles bounce in a helical path following the guiding center field line. The gradient of the field lines makes it such that they accelerate when going away from the Earth and decelerate when approaching Earth. The point where a particle stops moving towards Earth, reaching a pitch angle of $\alpha = 90^\circ$ is called the mirror point. Each particle path has two mirror points, located at opposite magnetic hemispheres. The particle is trapped bouncing between the two mirror points. [Prölss, 2004] writes the oscillation period as

$$\tau_O = \frac{4LR_E}{v} s_1(\alpha_0) = \sqrt{8m} R_E s_1(\alpha_0) \frac{L}{\sqrt{E}} \quad (1.20)$$

with

$$s_1(\alpha_0) \approx 1.3 - 0.56 \sin \alpha_0 \quad (1.21)$$

where α_0 is the equatorial pitch angle and R_E the Earth radius. This is

not the exact formula but only an approximation. m and E are the mass and energy of the particle, respectively, and L is the L shell value (see [McIlwain, 1961]) for the corresponding field line.

Drift

In the case of the drift component of the motion, we note two main parts. The gradient drift ($\mathbf{F}_{j\perp} = 0$, $\nabla B \perp \mathbf{B}$) and the external force drift ($\mathbf{F}_{j\perp} \neq 0$, \mathbf{B} uniform). Details are not given for this latter case, for further information see [Prölss, 2004]. The gradient drift is the motion caused by the particles gyrating between different regions where the field has different values. The gyroradius is dependent on the field intensity and so it varies accordingly. This constant change of gyroradius produces a motion as depicted in figure 1.14.

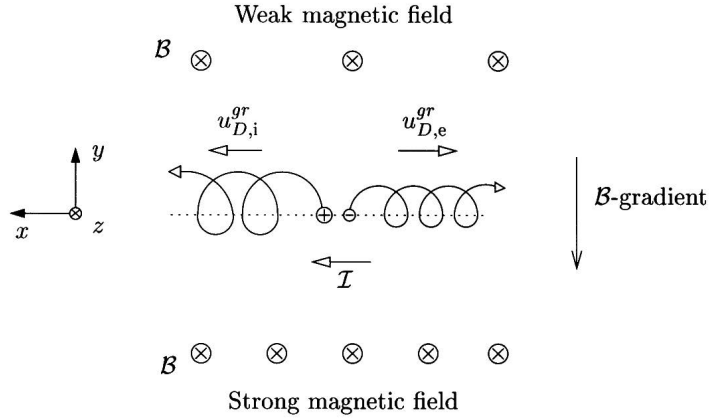


Figure 1.14 – Particle motion in a nonuniform magnetic field. The field gradient is perpendicular to the magnetic field direction. For simplicity, the gradient is taken to be a sudden jump in the magnetic field strength at the dotted line, and the initial motion of the particles is assumed to be perpendicular to this discontinuity. [Prölss, 2004].

The external force drift is mainly driven by the curvature drift, which is caused by centrifugal forces. Positively charged particles drift to the west while negatively charged particles drift to the east. This is the same directions caused by gradient drift, so the two constructively add, leading to the total drift we can identify.

The period of the total drift can be written as:

$$\tau_D = 2\pi R_E L / \langle u_D \rangle \approx \frac{2\pi}{3} R_E^2 |q| B_{00} \frac{1}{LE} \quad (1.22)$$

where u_D is the magnitude of the drift velocity and B_{00} is the field intensity at the apex (the point of maximum distance to Earth's surface) of the magnetic field line (see [Prölss, 2004]).

The composite motion of the particles is shown in figure 1.15 and takes into account the three separate motions described above. Table 1.1 shows the periods for each of those motions for different energy levels of protons and electrons. The periods are heavily dependent on the energy (except for the gyration period), most notably on the drift period (τ_D) where it can go from 45 years to just 2 minutes.

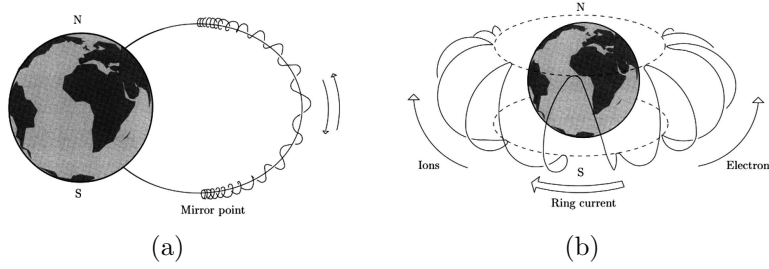


Figure 1.15 – Composite motion of charge carriers in the inner magnetosphere. left panel: gyration and bouncing; right panel: bouncing and drift [Prölss, 2004].

Particle type		Protons			Electrons*
Energy		0.6 eV	20 KeV	20 MeV	~
L		3	4	1.3	~
Period	τ_G	0.1 s	0.1 s	0.1 s	$5.4 \cdot 10^{-4}$
	τ_O	2 hours	1 min	0.5 s	$2.3 \cdot 10^{-2}$
	τ_D	45 years	9 hours	2 min	1

Table 1.1 – Comparison of the gyration (τ_G), oscillation/bounce (τ_O) and drift (τ_D) periods for representative particle populations in the inner magnetosphere. Each L value corresponds to a different magnetic field value. *(multiplication factor for the periods) Adapted from [Prölss, 2004].

1.4.3 Ionospheric currents

The ionosphere is a layer characterised by its high conductivity. This region is comprised of electrons and charged particles due to photoionisation that create an electrically conductive layer around the Earth. The initial interest in the study of the ionosphere came from its ability to reflect radio waves. Radio communications make use of this property to bounce waves off the ionosphere to reach greater distances on the Earth than would be possible with direct propagation. How the waves are reflected in the ionospheric layer depends of the specific composition of the ionosphere at the point where the radio waves hit, but also on the frequency of the incoming waves. This is not a point-wise reflection as in a mirror, but a gradual change in the propagation direction, due to a change in ionisation, that makes the waves curve back into the Earth. If there is not enough medium for the curving of the waves back to the Earth they eventually escape to outer space. With this knowledge, it is possible to tune the signal a specific band range to reach the desired destination [Koskinen, 2011].

The ionosphere is separated into different layers, by altitude. The region where most ionospheric currents circulate is named E region and it spans between 90 and 150 km altitude. The "E" comes from Electric, this being the layer where the electric properties of the ionosphere were initially identified. Examples of these currents are the auroral electrojets, the equatorial electrojet and the Sq (Solar quiet) current. These currents can be seen in figure 1.16. We can also see the field aligned currents that connect the ionosphere with the magnetosphere.

The Sq current is seen on the day side of the Earth. It results from the solar heating of the ionosphere. In figure 1.16 we can only see part of the Sq currents, as it is mimicked in the Southern hemisphere, but always on the Sun-facing side of the Earth. This circulation on the ionosphere has a consequence on the rest of the ionosphere. In the equatorial region the Northern and Southern hemisphere vortices combine to generate a strong eastward current, which is called equatorial electrojet.

There are two other currents designated as electrojets, the auroral elec-

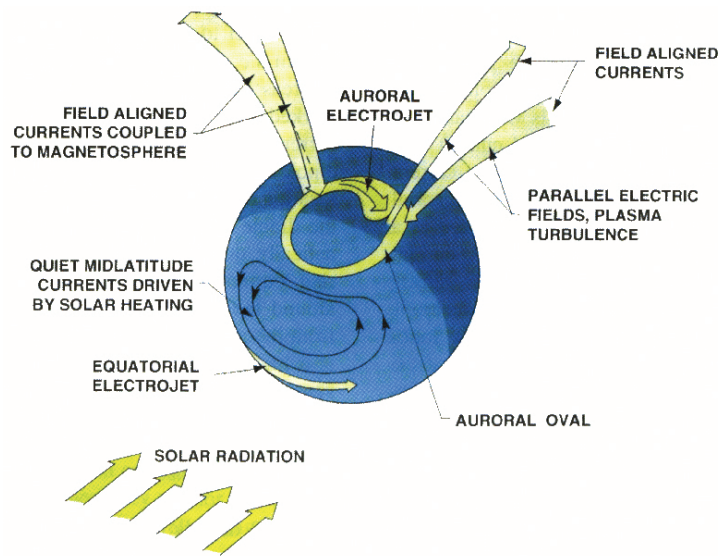


Figure 1.16 – Schematic representation of the main ionospheric currents (Source: GFZ Postdam).

trojets, one in the Southern polar region and another in the Northern one. They are relatively stronger than other currents located in the ionosphere due to the fact that the conductivity in the auroral regions is greater (due to the strong particle precipitation in the auroral zones), together with the electric field. These currents are relatively well defined in the auroral ovals, during quiet times. In case of a geomagnetic storm or other active periods the auroral electrojets expand into lower latitudes.

1.4.4 Thermospheric Density

The solar activity affects also the thermospheric density, which is governed by the absorption of extreme ultra-violet radiations. The globally averaged density of the thermosphere increases significantly with the solar activity. This can be clearly seen in figure (1.17) as we compare the 10.7 cm radio flux index (F10.7) and the thermospheric density for the same time period. The thermospheric density is represented in logarithmic scale as it changes a lot with varying solar activity. The 11-year oscillation in the solar activity is clearly present in the density values. The increase in density with solar activity is due to the expansion of the atmosphere, from the heating caused

by the increasing solar flux. As the lower layers rise, the density of the upper layers (above 200 km from the Earth's surface) increases. This build up of neutral particles will have strong effects on the population of energetic particles trapped near Earth. It highly increases the chance of ejection of an energetic particle after colliding with a neutral one, leading to the depletion of trapped particles in the Van Allen belts. This is the reason for the anti correlation between the solar activity and particle counts.

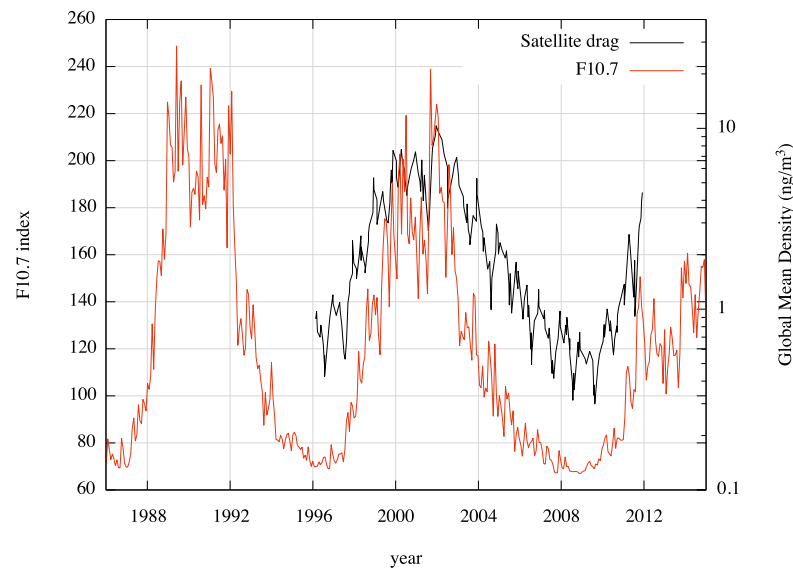


Figure 1.17 – Global mean neutral density at 400 km calculated from satellite drag in logarithmic scale [Solomon et al., 2013], and F10.7 solar index, representing the solar activity.

1.5 Core field

1.5.1 Geodynamo

As a consequence of the Earth's rotation and physical forces inside the fluid core (mainly buoyancy, Lorentz, Coriolis and pressure forces), the currents of molten metal have a complex geometry, which is why it is possible to sustain against Ohmic dissipation the magnetic field that we presently have. The Earth's outer core flow system can be studied making use of the Mag-

netohydrodynamic (MHD) equations. These equations make use of Fluid Dynamics, Electromagnetism and Thermodynamics.

A large part of the MHD approach is based on the Navier-Stokes equation (eq. 1.23), where both fluid velocity and magnetic field play a role.

$$\rho \left(\frac{\partial \vec{u}}{\partial t} + \vec{u} \cdot \nabla \vec{u} \right) + 2\rho(\vec{\Omega} \times \vec{u}) = -\nabla p + \vec{j} \times \vec{B} + \rho' \vec{g} + \mu \nabla^2 \vec{u} + \vec{f} \quad (1.23)$$

In this equation, ρ is the hydrostatic density, \vec{u} is the flow velocity in the rotating frame, p is the non-hydrostatic part of the pressure, $\vec{\Omega}$ ($\vec{\Omega} = \Omega \hat{z}$) is the Earth's rotation vector, \vec{j} is the electric current density, \vec{B} is the magnetic field, ρ' is the departure from the hydrostatic density, \vec{g} is the gravitational acceleration, μ is the dynamic viscosity and \vec{f} accounts for other body forces which may vary according to the considerations made about the system. The term $\vec{j} \times \vec{B}$ on the right-hand-side of equation 1.23 is called the Lorentz force, and it reflects the interaction between the magnetic field and the flow of the electrically conductive fluid.

The fluid in the outer core consists of an alloy of iron, nickel and other elements in small proportion. It is a good electrical conductor. The magnetic field is maintained by the geodynamo mechanism, in which the flow in the outer core generates a magnetic field. This process can be explained by the induction equation (1.24),

$$\frac{\partial \vec{B}}{\partial t} = \nabla \times (\vec{u} \times \vec{B}) + \eta \nabla^2 \vec{B} \quad (1.24)$$

where η is the magnetic diffusivity ($\eta = (\mu_0 \sigma)^{-1}$) and σ is the electrical conductivity. The first term on the right-hand-side accounts for both transport and stretching of the magnetic field. The latter mechanism is responsible for maintaining the magnetic field due to the flow's motion, and the second term is a dissipative term, which accounts for the loss of energy of the field. Equations 1.23 and 1.24 are coupled and, together with an energy equation, define the entire dynamic process [Holme, 2007]. Besides the fluid motion generating the magnetic field, if the magnetic field is strong enough it can affect the motion of the fluid, which is the case of the Earth's dynamo.

1.5.2 Secular Variation

Secular Variation is the name given to time variations of the core magnetic field of the Earth. The name suggests secular time scales, but yearly and decade variations are also studied. The main balance between advective and dissipative effects, which sustains the core field, occurs on long time scales of tens of thousands of years. But much quicker events can occur in the core, resulting in secular variation changes with timescale from 1 to 100 years. In this range, the energy spectrum of the magnetic field scales approximately as ω^{-4} where ω is the frequency ([Bouligand et al., 2016, Lesur et al., 2017]).

The spectrum of these rapid variations of the main field superimpose with that from external field sources, either ionospheric or magnetospheric, as these are typically of the order of one year or less. This superposition can make it hard to identify the events and to localize them as having source in the internal field.

The largest contribution of secular variation on a centennial timescale is the axial dipole decay. This accounts for the variation in intensity of the axial dipole part of the geomagnetic field. It has decayed at an average of 5% per century since 1840, when it was first measured accurately by Gauss and Weber [Barraclough, 1974]. This means that the intensity of our field is getting increasingly lower. Studies done for earlier periods (1590-1840) using archeointensity measurements ([Gubbins et al., 2006] based on [Korte et al., 2005]) found that the rate of decay might have been slower in previous epochs. Studying the entire available data suggests a fluctuating rate of evolution for the field intensity.

The Westward drift is a large feature of the secular variation, which cannot go unmentioned. For the past 400 years, the field at the Earth's surface has had a clear westward motion [Halley, 1692, Bullard et al., 1950]. Bullard initially concluded that the non-dipole part of the field moved west at a $0.18^\circ/\text{yr}$ rate. Today we know that this westward movement is not global, but depends on latitude [Jault et al., 1988]. There also seems to be a longitudinal dependence, as the Atlantic hemisphere is much more active than the Pacific hemisphere. A feature of the geomagnetic field where this mo-

tion is clearly seen is the South Atlantic Anomaly (SAA). This large scale region of minimum field intensity moves westward at $0.3^\circ/\text{yr}$. The westward drift is a decade to century time scale component of the secular variation. A much shorter feature of the secular variation, in the year time scale are the geomagnetic jerks. Geomagnetic jerks are sudden changes in the slope of the secular variation at the Earth's surface [Mandea et al., 2000, Balasis et al., 2016]. Since the first observation of these events, many moments where the trend in secular variation changed abruptly have been identified as geomagnetic jerks, for example in 1901, 1913, 1925, 1969, 1978, 1991, 1999 [Jackson and Finlay, 2007]. Jerks are not necessarily global features, some are only observed at specific locations and other times some delay is observed between different stations [Jackson and Finlay, 2007]. The occurrence of jerks is fully compatible with the ω^{-4} spectrum of the main magnetic field.

1.6 South Atlantic Anomaly (SAA)

Located in the South Atlantic region, above Brazil, is one of the most striking features of the present geomagnetic field. The South Atlantic Anomaly (SAA) as it is called is the region of space where the magnetic field intensity is much lower than the average value (see figure 1.18). There, the field intensity reaches less than 60% of the field strength at comparable latitudes. This is a large scale structure from the Earth's core field and as such, it can be observed even when considering a simple model of the field as the eccentric dipole. In fact, the eccentric dipole is a most useful tool in the study of this structure. The SAA is the largest feature of the geomagnetic field that shows the westward drift, with its point of minimum intensity having moved from Southern Africa to South America over the last 300 years [Mandea et al., 2007, Hartmann and Pacca, 2009]. The average velocity of this westward trend is $0.3^\circ/\text{yr}$ over the last 200 years [Hell, 2010], with higher and lower trends during the recorded history of this evolution. The evolution of the minimum depends on the spherical surface on which it is calculated. Using geomagnetic field models from the satellite era, an westward drift of

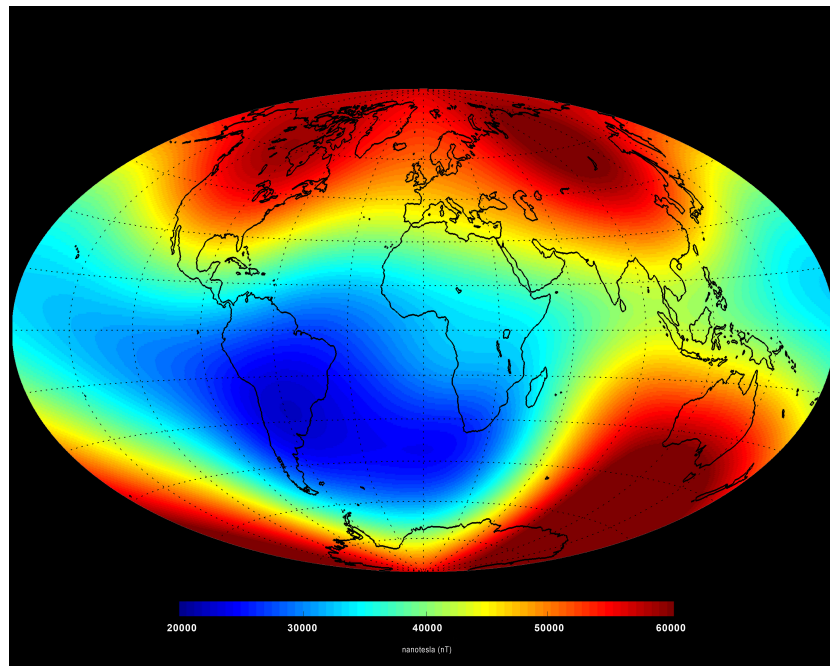


Figure 1.18 – Magnetic field Intensity of Earth on June 2014. Map plotted from Swarm data (Source: ESA/DTU Space).

$0.30^\circ/\text{yr}$ together with a slight northward drift of $0.008^\circ/\text{yr}$ and an intensity decrease of $20.98 \text{ nT}/\text{yr}$ can be identified at the Earth's surface. The same calculations at 800 km , give a westward drift of $0.17^\circ/\text{yr}$, a now southward drift of $0.020^\circ/\text{yr}$ and an intensity decrease of $8.90 \text{ nT}/\text{yr}$.

The existence of the SAA leads to another phenomenon. Because of the low intensity values of the field in the South Atlantic region, the mirror points in the Van Allen belts are located at lower altitudes. Therefore, high energetic particles that inhabit the inner Van Allen radiation belt reach lower altitude in this region. There are much more energetic particles trapped in the inner radiation belt reaching the altitude of low earth orbiting satellites ($400\text{-}1300 \text{ km}$) in this region than elsewhere. This is seen in figure 1.19 where a map of single events upsets (SEU) [Baker, 2004] is shown. SEUs occur when high energetic particles interact with electronic devices and cause bit flips.

The study of the SAA is an important study in itself. In order to be able to better predict its evolution and mitigate its negative effects in today's society, we first need a good description of its behaviour. An important part

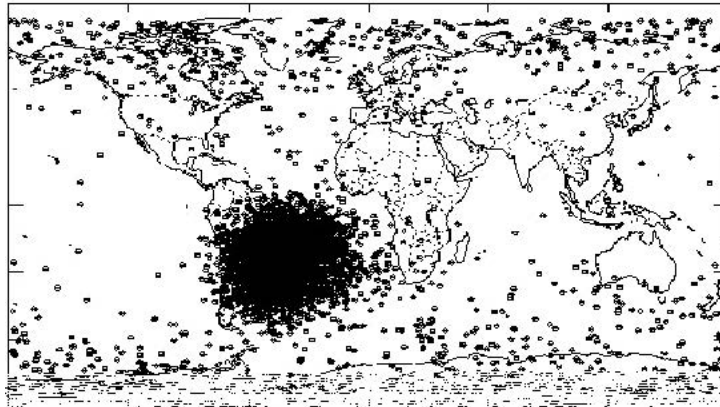


Figure 1.19 – Map of 'Single Event Upsets' from the satellite Uosat-3 1990-1999 (Source: ESA).

of this study is dedicated to this goal. In the literature, a reference to a South Atlantic Magnetic Anomaly (SAMA) can also be found [Hell, 2010], but we will not be using this terminology. Instead, we will use the designation SAA to refer to both the magnetic and particle flux anomalies.

Chapter 2

Geomagnetic Field Models

The magnetic field of the Earth is constantly changing. There are many observatories and satellites dedicated to measuring the field as precisely as possible and they provide an invaluable resource to those studying this area of science. The existent dataset covers several centuries [Jonkers et al., 2003, Manda and Mayaud, 2004]. By making use of mathematical methods, and using the large database of magnetic field observations, it is possible to construct magnetic field models. These models vary in degree of complexity, from the wide range of time periods they include to the amount of physical processes they try to represent [Hulot et al., 2015].

Some available models describe the global field over a long time period (one to four centuries), while others represent the field only for more recent years. Geomagnetic field models can represent solely the internal component of the field, which accounts for both the core and crustal components, taking them together or separately. The crustal component is a relatively small part of the field and constant over decadal timescales. It does not contribute to first differences of observatory data and as such it can be separated from the core contribution in field modelling. More complex models take into account the external components of the field as well as the internal component. These are known as comprehensive models [Sabaka et al., 2015].

Each different model is constructed in a different way, depending on the final application. A standard way to represent a field model is via the spher-

ical harmonic (SH) coefficients resulting from fitting the SH functions to the data. These allow for the observations to be reproduced very easily with only a relatively small amount of parameters. In this context, a field model is a set of SH coefficients for the field and its secular variation.

2.1 Spherical Harmonics

Spherical harmonics are a set of functions that are defined on the surface of a sphere, hence their name. The entire set of SH functions is orthogonal and thus, it is usually used to represent functions that are mapped on a spherical surface.

These functions are solutions of the so called Laplace's equation 2.1,

$$\nabla^2 f = 0, \quad (2.1)$$

which is a second-order partial differential equation, where f is a scalar function. Laplace's equation in spherical coordinates (r, θ, ϕ) , and considering specifically the potential field (V), where $B = -\nabla V$ (from $\nabla \times B = 0$) in a region that we suppose free from electrical currents yields:

$$\nabla^2 V = \frac{1}{r^2} \frac{\partial}{\partial r} \left(r^2 \frac{\partial V}{\partial r} \right) + \frac{1}{r^2 \sin \theta} \left(\sin \theta \frac{\partial V}{\partial \theta} \right) + \frac{1}{r^2 \sin^2 \theta} \frac{\partial^2 V}{\partial \phi^2} = 0. \quad (2.2)$$

The solution to this equation has two parts ($V^{total} = V^i + V^e$), one concerning internal sources where $r < a$ (equation 2.3) and another concerning external sources where $r > a$ (equation 2.4):

$$V^i = a \sum_{n=1}^{\infty} \sum_{m=0}^n \left(\frac{a}{r} \right)^{n+1} (g_n^m \cos(m\phi) + h_n^m \sin(m\phi)) P_n^m(\cos \theta) \quad (2.3)$$

$$V^e = a \sum_{n=1}^{\infty} \sum_{m=0}^n \left(\frac{r}{a} \right)^n (q_n^m \cos(m\phi) + s_n^m \sin(m\phi)) P_n^m(\cos \theta) \quad (2.4)$$

where P_n^m are the associated Legendre polynomials, $g_n^m, h_n^m, q_n^m, s_n^m$ are the spherical harmonic coefficients, n is the degree, m is the order and a is usually

taken as the Earth's mean radius but can also be the radius of a satellite orbit (see chapter 7).

Writing $B = -\nabla V$ in spherical coordinates, we get:

$$\mathbf{B} = -\frac{\partial V}{\partial r} \hat{\mathbf{r}} - \frac{1}{r} \frac{\partial V}{\partial \theta} \hat{\boldsymbol{\theta}} - \frac{1}{r \sin \theta} \frac{\partial V}{\partial \phi} \hat{\boldsymbol{\phi}} \quad (2.5)$$

which will give us the representation of the three field components (B_r , B_θ and B_ϕ) in terms of the spherical harmonics coefficients. For the internal part of V :

$$B_r^i = \sum_{n=1}^{\infty} \left[(n+1) \left(\frac{a}{r}\right)^{n+2} \sum_{m=0}^n (g_n^m \cos(m\phi) + h_n^m \sin(m\phi)) P_n^m(\cos \theta) \right] \quad (2.6)$$

$$B_\theta^i = - \sum_{n=1}^{\infty} \left[\left(\frac{a}{r}\right)^{n+2} \sum_{m=0}^n (g_n^m \cos(m\phi) + h_n^m \sin(m\phi)) \frac{dP_n^m(\cos \theta)}{d\theta} \right] \quad (2.7)$$

$$B_\phi^i = - \sum_{n=1}^{\infty} \left[\left(\frac{a}{r}\right)^{n+2} \sum_{m=0}^n (-g_n^m \sin(m\phi) + h_n^m \cos(m\phi)) \frac{m P_n^m(\cos \theta)}{\sin \theta} \right] \quad (2.8)$$

The components for the external part can be obtained in a similar manner. In practice, this summation over n cannot be done to infinity, a truncation value (n_{max}) must be chosen, and it will be determined by the available observations.

The problem is now how to obtain the SH coefficients from the observations of \mathbf{B} . This can be written in a simplified manner if we consider \mathbf{d} to be a vector of data values, and \mathbf{m} to be a vector containing all the unknown coefficients $\{g_n^m, h_n^m\}$:

$$\mathbf{d} = \mathbf{A} \mathbf{m} \quad (2.9)$$

where \mathbf{A} is the matrix containing the equations of the system. The direct problem is easy to solve, but the inverse problem, to obtain \mathbf{m} from \mathbf{d} , is much harder. The usual method to find the coefficients \mathbf{m} is to find a model that minimizes the least-squares difference between the model predictions and the observations [Jackson and Finlay, 2007]. This is a nonunique problem and as such, some further considerations need to be made about the system in order to get a single solution (see [Hulot et al., 2015]).

When applying SH to geomagnetic field data, the spectra of the spherical harmonics can be a useful tool to understand the components of the internal field. Equation 2.10 shows the contribution of SH coefficients to the spectra.

$$R_n = (n + 1) \left(\frac{a}{r} \right)^{2n+4} \sum_{m=0}^n ((g_n^m)^2 + (h_n^m)^2), \quad (2.10)$$

If the values of R_n are plotted against n we have the power spectra of a certain field. Figure 2.1 shows the power spectra for several large bodies. For Earth, a very straightforward observation to make is the separation of the two components of the internal field, the core and crustal fields. Since they represent signals with sources at different depths, they appear in the spectra as two segments with different slopes. The segment with strongest inclination contains the dominant dipolar contribution and subsequent multipoles up to degree $n = 13, 14$. The segment with weakest inclination is from the crustal field. This is only a crude way to separate the two components, but it shows at which point in the SH decomposition the crustal field starts to dominate the main field.

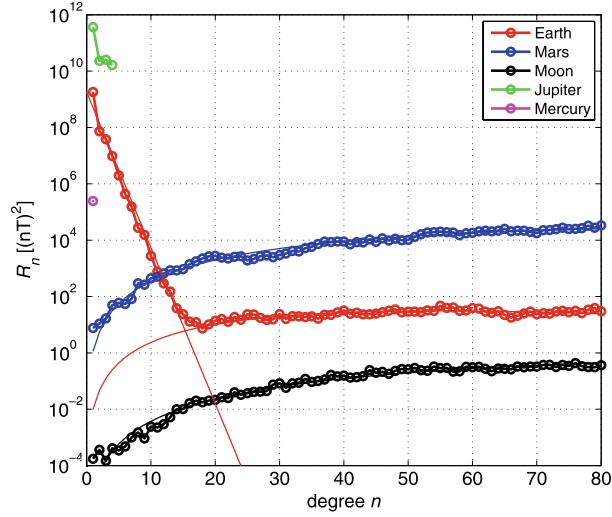


Figure 2.1 – Mauersberger-Lowes spectra for Earth, Mars, Moon, Jupiter and Mercury. [Hulot et al., 2010]

With this information, modellers can adjust which level of coefficients to use for their particular case. For Mars and the Moon, we only see the

crustal component of the field, as these bodies do not possess any dynamo or core field. Jupiter and Mercury are very little constrained due to limited data, this only allows to represent the large scale features of the field. Higher degrees would require a large coverage of data [Hulot et al., 2010]. Already, the Messenger mission has allowed to map accurately the magnetic field above half the surface of Mercury [Oliveria et al., 2014]. Measurements from the ongoing Juno mission are currently being analysed to constrain the depth of magnetic sources. Finally, the last measurements of Cassini may provide a much sharper picture of the field of Saturn.

2.2 CHAOS-6

The CHAOS-6 [Finlay et al., 2016] model is the latest in the CHAOS series of Earth magnetic field models [Olsen et al., 2006]. Data from around 160 ground observatories (annual differences of revised monthly means) were used together with satellite data. These include the most recent Swarm data, collected from a 3-satellite constellation in orbit since end of 2013 [Olsen et al., 2015]. The time variation of the field is described by cubic B-splines with 6 months knot spacing, from 1996 to 2016.5. The actual temporal resolution is not so high because of regularisation. The model is precise enough to resolve peaks of secular acceleration (second time derivative of the field) separated by about 3 years, up to harmonic degree $n = 9$. In order to produce a solely core field model, regularisation methods are applied to reduce crustal field influence. A regularisation of temporal variations is also done by penalising the second and third derivatives of the radial field B_r in the cost function (see [Finlay et al., 2016]). This amounts to a damping parameter. By damping the higher degrees starting at this point, the crustal component is tapered. This is a better approach than applying an abrupt cut-off, as that would completely eliminate smaller scale features from the field and produced ringing (Gibbs effect).

In this manuscript we have used CHAOS-6 to identify trends of the SAA that depend on the morphology of the main field, such as the latitude and longitude of the location of minimum field intensity and the time evolution

of this minimum. The used eccentric dipole model was also obtained from CHAOS-6.

2.3 COV-OBS

The most recent version of the COV-OBS field model [Gillet et al., 2015a] covers the period from 1840 to 2020. The dataset from CHAOS models is used for the time period which is common to both models and the dataset from [Jackson et al., 2000] is used for the earlier period [Gillet et al., 2013]. The time variation of the field is given by B-splines of order 4 with knot spacing of 2 years from 1838 to 2022 [Gillet et al., 2015a]. The extra points at the ends are introduced in order to reduce edge effects. Due to regularisation to remove mostly crustal field sources, we also lose information on the smaller scale structure of the core field. In order to counteract this effect, the COV-OBS model uses a stochastic approach [Gillet et al., 2009] instead of the commonly used regularisation that consists in penalising second and third order space and time derivatives [Finlay et al., 2016]. Therein, an ensemble of stochastic, time-correlated, small-scale magnetic field models are produced, based on the observed behaviour for the large scale structures. This stochastic ensemble allows to assess the small scale structure of the field. In [Gillet et al., 2015b] they proceed to invert this model to compute the flow of molten metal at the surface of the core. The inversion requires a good knowledge of the small scale features of the geomagnetic field, and it was with this in mind that the COV-OBS model was computed.

2.4 Comprehensive Models

Comprehensive Models (CM) [Sabaka et al., 2002] aim to represent every aspect of the field. They were developed by NASA and recently DTU (CM5) [Sabaka et al., 2015] to describe the near-Earth magnetic field. Core, crustal, ionospheric, magnetospheric, M2 semi-diurnal gravitational tidal, associated induced fields and ionospheric toroidal fields are all parameterised indepen-

dently. The most recent CM5 model goes from August 2000 to January 2013 and makes use of ground observatory data and satellite observations.

2.5 Dipole approximations

The large-scale geomagnetic field can be approximated to a tilted dipole, offset relative to the Earth's center [Fraser-Smith, 1987]. This is called the eccentric dipole approximation. This simple approximation explains most of the observed field. The key features of the geomagnetic field evolution are kept in the dipole approximation, such as the Westward drift and the decay of the dipole moment. The Westward drift is seen in many field structures, mainly in the Atlantic hemisphere and close to the equator. This drift is very well studied and long time series are available [Halley, 1692, Bullard et al., 1950]. One such method to calculate the westward drift is by looking at the evolution of the eccentric dipole position. The eccentric dipole is currently offset from the Earth's center by about 550 km in a direction approximately 22°N , 140°E . This distance is steadily increasing, moving outward around 45 km in the last 20 years. In figure 2.2 we can see how the variation of the position of the dipole was obtained by tracing a line from the center of the Earth to the surface and passing through the center of the dipole. The antipodal point of the intersection of this line with the surface provides the location of the dipole seen in figure 2.3.

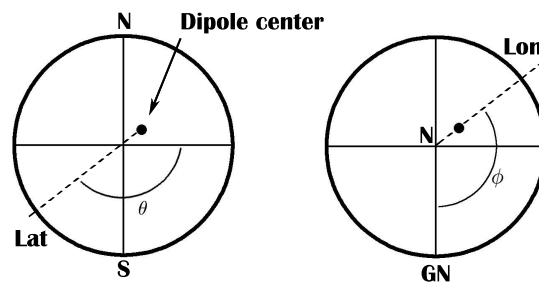


Figure 2.2 – Schematic representation of how the position of the dipole was obtained (meridional plane on the left, equatorial plane on the right). Latitude calculation shown in the left and Longitude on the right. GN symbolises the Greenwich meridian.

As can be seen there, it is drifting in the westward direction and slightly southward. Shown in figure 2.3 are also two other ways to track the evolution of the SAA. The tracking of the minimum of intensity of the magnetic field, here done using the CHAOS-6 field model and the tracking of the maximum of particle flux, done using data from three POES satellites (10, 12 and 15). For the antipodal location of the eccentric dipole, the westward drift obtained is $0.29^\circ/\text{yr}$ with a southward drift of $0.056^\circ/\text{yr}$. For the minimum of intensity from CHAOS-6, the westward drift is $0.16^\circ/\text{yr}$ with a southward drift of $0.020^\circ/\text{yr}$. The particle flux does not have a constant trend, but considering the initial and final position, the westward trend would be $0.24^\circ/\text{yr}$ with a northward trend of $0.037^\circ/\text{yr}$.

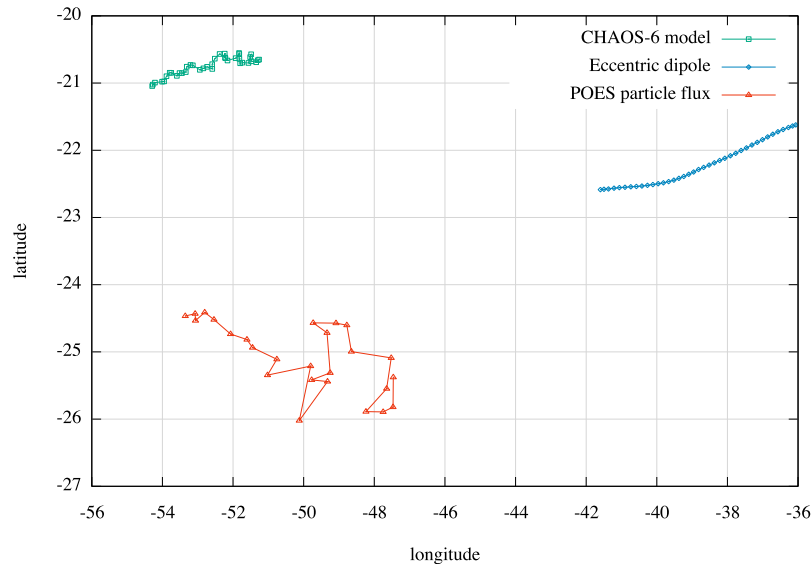


Figure 2.3 – Position of the 'SAA' according to three different approaches. CHAOS-6 minimum intensity for the period 1997-2014, the eccentric dipole antipodal position for the same period and POES maximum particle flux for the period 1986-2014. All show westward movement of the anomaly, with the initial position being on the right for all three plots. Note that POES position was obtained from real data, and has the superposed effect of the solar cycle which explains the rougher look of the trajectory.

The total dipole strength has diminished by 9% from 1840 to 2015. Presently, the decrease of the field intensity, which is accurately mapped from low Earth orbiting satellites, is also observed located in the Southern African - Southern Atlantic region [Finlay et al., 2016]. A strong point in

favour of the eccentric dipole simple approximation to the geomagnetic field in the context of this study is the fact that it allows to capture most of the structure and evolution of the South Atlantic Anomaly. The eccentric dipole part of the field depends only on spherical harmonic coefficients up to degree $n = 2$ [Fraser-Smith, 1987]. Note that there are other methods to pick up the eccentric dipole from the total field, as expounded by [Lowes, 1994].

The eccentric dipole model is more accurate further away from Earth, as the higher degrees of SH decrease faster with distance. Particles coming from outside the magnetosphere are strongly constrained by the dipolar component of the field without ever feeling the effects of small scale structures.

If we want to look at the evolution of the SAA from the particle flux perspective we need an extra coordinate parameter. The L parameter, or L-value [McIlwain, 1961] maps the field lines according to the intensity of the field at the geomagnetic equator. For a given field line, in a dipole field, the L parameter is defined according to:

$$L = \frac{(r/a)}{\cos^2 \lambda} \quad (2.11)$$

where r/a is the distance in Earth radii to each point in the field line and λ is the corresponding geomagnetic latitude (see figure 2.4). The distribution of trapped particles in the Van Allen radiation belts follows closely the geometry of constant L value shells (figure 1.9).

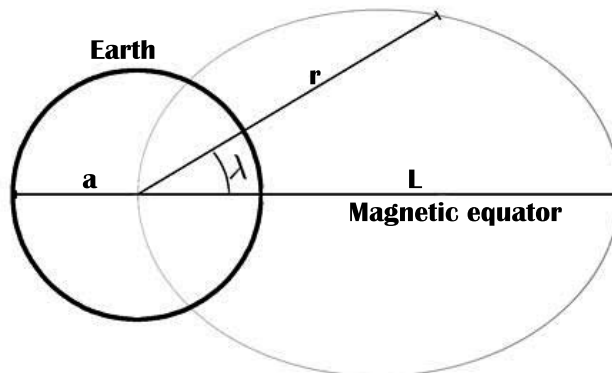


Figure 2.4 – Schematic representation of the calculation of a field line's L value.

Chapter 3

Satellite Data and Proxies

Most results in this study were derived from satellite observations, although geomagnetic field models and proxies built from geomagnetic and solar surface observations were also used. To study the evolution of the energetic particle flux over the SAA, data from five different satellites were required: three satellites of the POES NOAA (Polar Orbiting Environmental Satellites, National Oceanic and Atmospheric Administration) [Evans et al., 2008] series, the CALIPSO (Cloud-Aerosol Lidar and Infrared Pathfinder Satellite Observation) [Winker et al., 2007] and Jason-2 [Willis et al., 2016]. This group of satellites was selected in order to provide data in different energy ranges and at different altitudes. Besides particle flux data, magnetic field measurements from satellites were also used. The Earth's magnetic field is largely responsible for the distribution and the evolution of the particle flux in the atmosphere, and so, we also used magnetic field observations from the CHAMP satellite and the Swarm satellite constellation. In this case, the satellite data were processed beforehand into Virtual Observatories (VO) [Mandea and Olsen, 2006] and then analysed using PCA.

3.1 Energetic Particles

3.1.1 POES NOAA

The POES NOAA satellites are a series of polar orbiting satellites (i.e., their orbital plane almost crosses the poles) that were initially launched in 1970 with the objective of monitoring the weather. Over the years, different instruments were added to the payload, including the SEM (Space Environment Monitor) and SEM-2 (newer version) detectors. The SEM/SEM-2 are spectrometers that provide measurements of the flux of charged particles at the satellite altitude, which we use in our study. Having similar polar orbits, all the satellites of this series orbit at ~ 830 km. Due to its orbit, POES has a daily global coverage, with approximately 14 polar orbits per day (i.e., an orbital period of around 102 min) [eoPortal Directory, 2017d].

From the nineteen POES satellites launched to date, only three are operational as of this moment, POES 15, POES 18 and POES 19. For this work, data from three POES satellites were considered, POES 10, POES 12 and POES 15. The latter is the first of the 5th generation of POES satellites and was selected over the most recent ones as it has a longer time series of data while also having the newer version of the SEM detector (SEM-2). This satellite was launched on the 13th of May 1998 and is currently the secondary satellite in the morning orbit of the POES series, crossing the equator at about 7:30 AM local time.

POES 10 and POES 12 were chosen from the previous generation of satellites with the specific goal of providing an uninterrupted series of data over the entire period from 1986 to the present. POES 10 was launched on the 17th of September 1986 and was operational until September 1991, even though some instruments had already failed. The date selected to put POES 10 in standby mode coincided with the time POES 12 became fully operational. It was launched on the 14th of May 1991. These two satellites, from the 4th generation of POES satellites, had the SEM instrument onboard, instead of the SEM-2. This is the main difference among the three satellites as much like POES 12 was launched to replace POES 10 orbit, POES 15

was launched to replace POES 12 when it was put into standby as well [eoPortal Directory, 2017d].

The SEM and SEM-2 omni-directional detectors, which measure the proton flux from all directions at the location of the satellite, operate in certain ranges. For SEM, three energy bands are recorded (> 16 , > 36 and > 80 MeV), while for SEM-2 there are four bands (> 16 , > 36 , > 70 and > 140 MeV). Other detectors are included in the SEM instrument, which measure less energetic protons in narrow energy ranges. Here, we are most interested in the flux of high energy protons, which populate the inner radiation belts [eoPortal Directory, 2017d].

3.1.2 CALIOP

The CALIPSO satellite orbits at approximately 705 km altitude, about 100 km lower than the POES satellites. It completes approximately 14.5 orbits per day with an inclination of 98.05° . CALIPSO was launched on the 28th of April 2006 and for this work, we used a data series of almost 8 years of measurements, from 2006 to 2014 [eoPortal Directory, 2017a].

As an independent source of information to the particle flux provided by the POES mission, the CALIOP (Cloud-Aerosol Lidar with Orthogonal Polarization) instrument readings, on board of the CALIPSO mission were used. Data provided by the CALIOP instrument are not strictly particle flux, they are called dark noise. In photomultipliers and avalanche photodiodes used in detectors, there is always some background signal even in the absence of incident photons, caused by random generation of electrons in the system, which is called 'dark noise' and is handled in a statistical framework. The CALIOP detectors show a significant increase of dark noise in the region of SAA [Hunt et al., 2009]. This interference is caused by the particle flux increase in the region, so it can be used as proxy for energetic particles flux.

3.1.3 Jason-2

Jason-2 is the second satellite from an oceanographic mission managed by CNES and NASA. The initial satellite (Jason-1) was launched on the 7th of

December of 2001. Both of these satellites are successors of the oceanographic research mission, TOPEX/Poseidon, that ended in 2005.

Jason-2 was launched on the 20th of June of 2008 and designed to operate between 3 and 5 years [eoPortal Directory, 2017c]. It is still operational today with over 9 years of records available. Jason-2 has a non-sun-synchronous orbit at around 1336 km altitude and it takes 9.9 days to repeat the same orbit, covering all local times in 58.7 days [Zawadzki et al., 2016]. Its main mission is to monitor oceanographic events, thus contributing to the continuous record of observations from the previous missions. All the main instruments are dedicated to this main purpose, but some auxiliary instruments are designed to record other parameters that are important for the functioning of the satellite. This is true of the detectors Carmen-2 ('Caractérisation et Modélisation de l'Environnement'-2), which monitor space radiation and energetic particle flux. The strong particle flux intensity affects some of the instruments on board, as for example DORIS (Doppler Orbitography and Radiopositioning Integrated by Satellite). This instrument is responsible for the correct calculation of the position of the satellite in relation to Earth and has suffered from frequency shifts of its clock in areas of increased particle flux intensity as the SAA. The ICARE-NG instrument is one of the constituents of Carmen-2 and it measures electron and proton flux with 16 s resolution [Bourdarie et al., 2014]. For protons, the ICARE-NG provides either differential or integrated channels, but for this work we relied only on the integrated channels. From the 21 available channels (> 63, > 64, > 69, > 76, > 80, > 83, > 87, > 93, > 94, > 97, > 104, > 108, > 113, > 115, > 119, > 127, > 138, > 163, > 186, > 222 and > 292 MeV), we made use of the lower and higher ranges (> 63 and > 292 MeV).

3.2 Geomagnetic Field

3.2.1 CHAMP

The CHAMP (Challenging Minisatellite Payload) satellite mission was launched on the 15th of July of 2000 into a near-polar orbit [eoPortal Directory, 2017b].

It burnt up in the atmosphere on the 19th of September of 2010, having long outlived 5 years expected duration. It was planned with the intent of studying the Earth's magnetic field, the Earth's gravity field from orbit perturbations and atmospheric and ionospheric perturbations from GPS radio occultation and Langmuir probe measurements. For our study, only the geomagnetic field measurements are of interest. The satellite initial orbit was 454 km, and at the end of its life it dropped to around 300 km, with an orbit of about 94 minutes, providing a complete local time coverage every 131 days.

The instruments set responsible for the magnetic field measurements, called MIAS (Magnetometer Instrument Assembly System), was a package consisting of a Overhauser scalar magnetometer (OVM), two fluxgate vector magnetometers (FGM) and also two star imagers that provided the altitude information required for the FGM. The OVM, built by LETI in Grenoble, France, had a working range of 16000 to 64000 nT, a resolution of 0.1 nT and a sampling rate of 1Hz. It operated based on a proton Larmor precession in a weak field, which is directly proportional to the magnetic field and allows to retrieve the absolute magnetic field intensity of the Earth. The signal quality is improved through an Overhauser effect, whereby electron spins couple to the protons' thus increasing proton polarization. The magnetic field intensity from the OVM is then used to calibrate the FGM data. The two FGM and the star imagers were built by DTU, Copenhagen, Denmark. The FGMs had a working range of ± 64000 nT with a resolution between 1 and 2 nT. The FGMs measure the vector components of the field based on vector feedback geometry. This method consists of three coaxial coils with ferromagnetic cores mounted orthogonally around a sphere, and the current in each coil is a measure of one of the field components [eoPortal Directory, 2017b].

In this work, the data used from CHAMP have been converted into Virtual Observatories series by Chris Finlay and Magnus Hammer (see chapter 7). VOs provide a better dataset to which the PCA method can be applied, as measurements are interpolated to constant spatial positions and at regular intervals. This pre-analysis also removed undesired data during specific periods of time and events.

3.2.2 Swarm

Swarm is the latest in a series of satellite missions planned to study Earth's magnetic field. It follows Ørsted and CHAMP in the attempt to provide insight into the origin and evolution of the magnetic field, both the main component with origin inside the Earth and also the external components that affect human activities on the ground and in altitude, within the neighbouring space. Swarm is very different from previous missions as it consists of a three satellite constellation, Swarm-A, Swarm-B and Swarm-C [eoPortal Directory, 2017e].

The constellation is made of two satellites (Swarm-A and Swarm-C) flying at a lower altitude of 450 km, side-by-side at an inclination of 84.7° and recording the East-West gradient of the magnetic field. Swarm-B flies at a higher altitude of 530 km with inclination of 88° and different local time sector. The satellites cover 15 orbits every day. The constellation of satellites was launched into orbit on the 22nd of November 2013 to an initial altitude of 490 km, which was then corrected to the present configuration [eoPortal Directory, 2017e]. The two groups of satellites cover all local times every 9 months. The orbital plane of the satellite B continuously drifts with respect to the common orbital plane of the satellites A and C. The three satellites initially shared the same orbital plane and by the end of 2021, they will be in the same plane again but Swarm-B shall orbit in a direction opposite to the two other satellites.

Swarm was planned to bring insight into different problems of Geomagnetism. These include, core dynamics and core-mantle interaction, lithospheric magnetization, conductivity in the mantle and magnetospheric and ionospheric currents. Regarding the core, the increased spatial and temporal resolution of Swarm provides the next step in studying magnetohydrodynamic effects in the core on shorter time scales, from sub-annual to decadal [eoPortal Directory, 2017e]. As for the external components of the field, the simultaneous measurements at different altitudes and different local times provided by the constellation allow for a better separation between internal and external components. Knowing the structure of the external field is of

great value for space weather research, and also, clearly identifying the external parts of the observed field is key in data selection and comprehensive modelling to improve models of the internal field.

Each Swarm satellite has two different magnetic field measurement instruments [eoPortal Directory, 2017e]. The VFM (Vector Field Magnetometer) is responsible for measuring the vector magnetic field. It consists of three Camera Head Units (CHU) for precise altitude measurements and a CSC (Compact Spherical Coil) vector magnetometer sensor. The arrangement of the CHUs guarantees that neither the Sun nor the Moon interfere with all of them at any given time, providing detailed measurements during the entire duration of the mission. The VFM in Swarm is based on the fluxgate transducer and operates with an accuracy of 0.5 nT and a range of ± 65536 nT. The ASM (Absolute Scalar Magnetometer) developed by CNES and LETI, measures the total field intensity and is also used to calibrate the VFM, much like in CHAMP. The ASM has a range between 15000 nT and 65000 nT with a resolution of 0.1 nT. The ASM was developed in order to overcome some of the limitations detected in previous missions regarding the OVM instruments. The ASM is a pumped helium magnetometer, relying on an optical pumping process instead of the dynamic nuclear polarization previously used. Previously, the signal amplitude depended on the magnetic field strength, but with the optical pumping process, polarization is much more efficient and the signal amplitude is constant over the entire working range of the instrument. Before, there was a trade-off between omnidirectionality of the detector and the resolution, due to low polarizing efficiency. Now, with ASM, the magnetometer is always operating in optimal conditions providing accurate data.

Both ASM instruments of Swarm-C are not operational any more, but as the satellite orbits parallel to Swarm-A, the vector data are useful. Swarm has already had a great impact in magnetic field mapping, by allowing easier separation between different sources, obtaining higher resolution for known features of the Earth's core [Livermore et al., 2017] and also providing data for the highest resolution lithospheric magnetic field map to date [Olsen et al., 2017].

3.3 Geomagnetic activity

In order to broadly characterise the contribution of certain sources of geomagnetic activity, several indices have been developed over time. We chose to group them in two classes, solar activity proxies and geomagnetic indices in this work, leaving out many other indices that can be taken into account when studying the Sun-Earth interaction. The first group is made up from indices that give information on the strength of the Sun's activity, allowing to distinguish between solar active and quiet conditions. The second group and most important in geomagnetic field modelling are indices that determine the global geomagnetic storm activity, and are important for data selection prior to modelling. Also, this latter group includes indices that characterise high latitude currents that contribute to the external component of the field.

3.3.1 Solar activity proxies

The sunspot number is a measure of the solar magnetic activity. It was first thought out by Rudolf Wolf in 1848 and is still recorded today. It directly measures the number of sunspots and groups of sunspots on the surface of the Sun which are relatively dark regions on the photosphere, where the solar strong magnetic field opposes convection (see figure 3.1).

An alternative to the sunspot number, which also measures the Sun's activity is the F10.7 index. The name derives from the 10.7 cm wavelength of the solar emission spectrum, a radio wave originating in the high chromosphere and low corona of the Sun (see figure 3.1). The distinctive feature of this radiation is that it can be easily measured from ground, in all types of weather.

A third but less direct way of measuring the activity of the Sun is by monitoring the neutral density in the thermosphere. This can be calculated based on accelerometer data from spacecrafts. As we see from figure 3.1, it is directly correlated with the other two indices. When the Sun is at a peak of activity, the atmosphere expands due to the increased amount of radiation. This expansion of the lower layers of the atmosphere leads to an increase in density at higher altitudes.

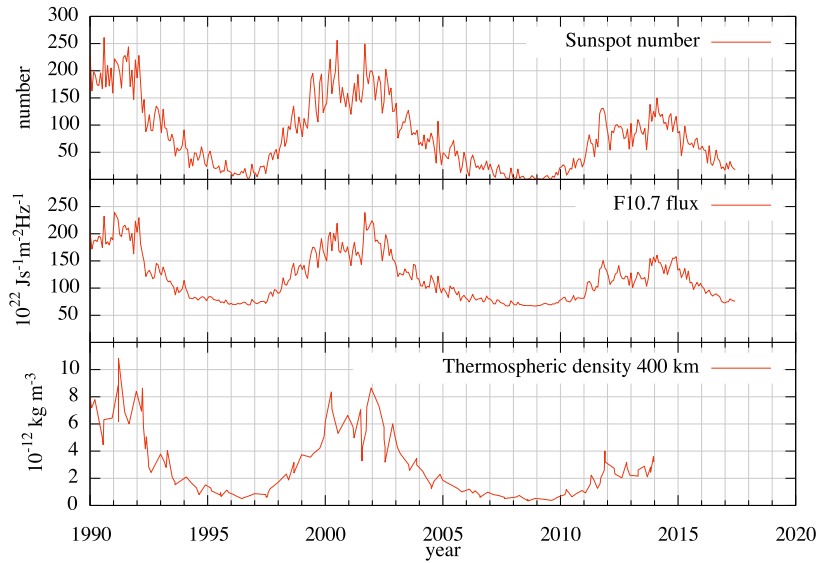


Figure 3.1 – Sunspot number over the 1990-2017 period (top), F10.7 index during the same period (middle) and thermospheric neutral density at 400 km (bottom) adapted from [Emmert, 2015]. Values shown are of monthly means.

3.3.2 Geomagnetic indices

The planetary index K_p , is an index computed every 3 hours that aims to describe the disturbances in the geomagnetic field caused by the Sun at a global scale. It is currently derived from 13 sub-auroral stations. For each station, the disturbance level is obtained by looking at the most disturbed horizontal magnetic field component and computing the logarithm of the difference between the lowest and highest value over each 3 hour interval, after removing the regular daily variation. This range is then converted to a standardised K_s value, which ranges from 0 to 9, the quietest and the most disturbed respectively. Within that range K_s is scaled in 28 values, ordered as: $0^0, 0^+, 1^-, 1^0, 1^+, \dots, 8^-, 8^0, 8^+, 9^-, 9^0$. The global K_p index is obtained from the mean of the K_s value for the 13 selected stations. Note that during a quiet year, $K_p \leq 2^0$ occurs for 70% of the time, while this is only true during 25 % of the time in a disturbed year [Kauristie et al., 2017]. In figure 3.2 we can see the K_p values for the past 27 years.

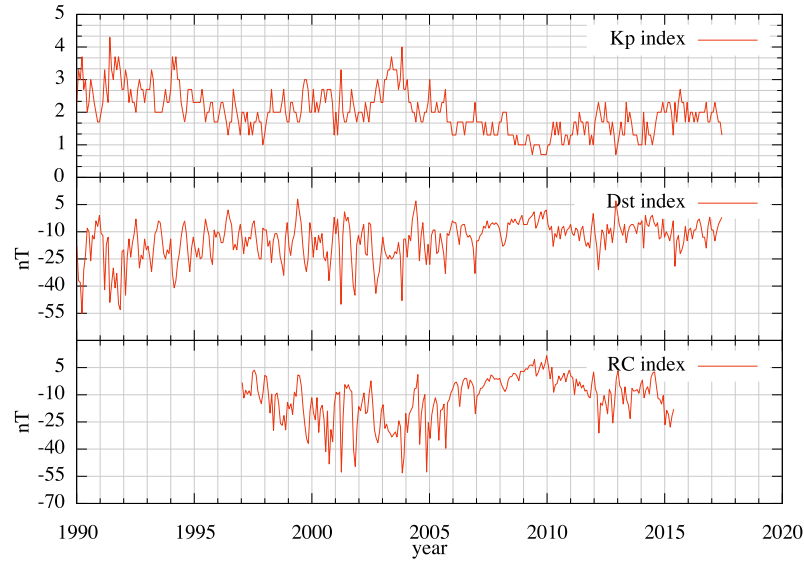


Figure 3.2 – Geomagnetic monthly means for the 1990-2017 period: Kp (top), Dst (middle) and RC (bottom).

Dst is an index derived to study disturbed magnetic field periods. It is often considered to monitor variations of the equatorial magnetospheric ring current, but other magnetospheric current systems are also known to contribute [Tsyganenko and Sitnov, 2005]. Magnetic quiet times can be associated with $|Dst| < 30$ nT, or the time derivative ($|dDst/dt|$) less than 2 to 5 nT/h [Kauristie et al., 2017]. In the world of geomagnetic field modelling, fitting both ground and satellite data accurately is important and so is data selection. Dst has been used to parameterise the time variation of the magnetosphere ring current during quiet times, but this was not its initial purpose, it was designed to study disturbed times and so the baseline was not of great importance. After Dst was introduced, other versions appeared, tailored to study more specific issues. One of this is the RC (ring current) index [Olsen et al., 2014]. The RC index was introduced specifically to address the baseline issue, and used to parameterise the time variations of the near-Earth magnetospheric field for the CHAOS series of field models. In the latest version of RC [Finlay et al., 2015], the index is obtained from 14 ground observatories at low and medium latitudes to avoid contamination by the auroral electrojets and, also, Sq currents are taken into account by

choosing only night time data.

The Auroral Electrojet (AE) indices (AE, AL and AU) were introduced in 1996 by Davis and Sugiura. They aim to describe the behaviour of the auroral electrojet currents, in the high latitude ionosphere. These currents are the reason Dst and similar indices only use observatory data from low to medium latitudes. The AE indices are constructed from the horizontal magnetic field component measured at observatories located in the northern hemisphere under the auroral oval, at latitudes between 60° and 70° . The AU index corresponds to the eastward electrojet while AL corresponds to the westward one. AE is simply the difference (AU - AL) between the two. Another index (AO) can also be obtained by averaging the two $((AU + AL) / 2)$ [Kauristie et al., 2017]. In figure 3.3 we show the AE, AL and AU indices.

AE indices provide good insight into magnetospheric and ionospheric interactions with solar wind. The reason they are not commonly used in internal field modelling to address the auroral currents is the fact that when the auroral oval is expanded or contracted (strong activity, weak activity), it is difficult to reliably determine the electrojet from their values.

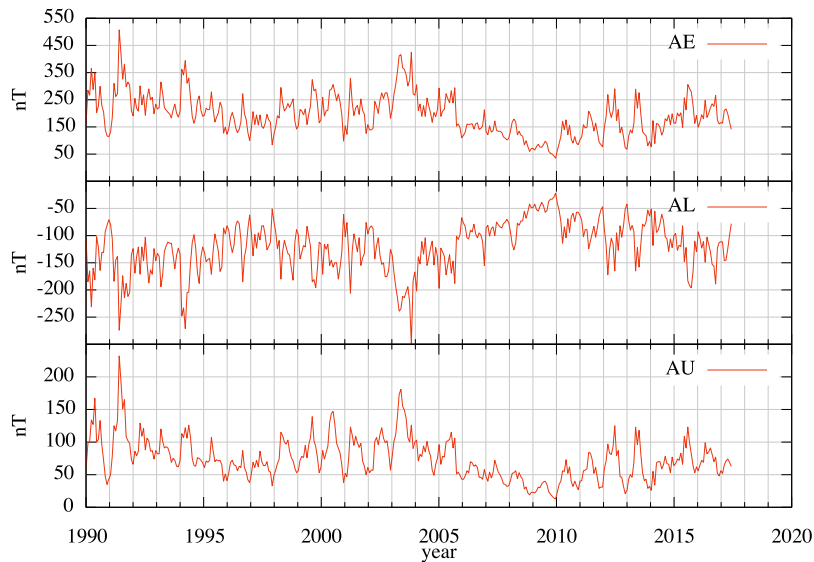


Figure 3.3 – Auroral Electrojet difference (AE) (top), westward electrojet (AL) (middle) and eastward electrojet (AU) (bottom) for the 1990-2017 period (monthly means).

Chapter 4

Principal Component Analysis (PCA)

4.1 Introduction

The method, known as Principal Component Analysis (PCA), provides a description of data by concentrating in a small number of spatial patterns (the Empirical Orthogonal Functions, EOFs) and corresponding time series (Principal Components, PCs), most of the observed variability in the data. The analysis is based on a spectral decomposition of the data correlation matrix and the individual modes (pairs of spatial structures and corresponding temporal series) are by construction decorrelated in space. The main idea behind a PCA analysis, is to reduce the dimension of the underlying problem. This is achieved while maintaining as much of the initial variation as possible. In the field of geomagnetism, we can find a recent application of PCA in [Pais et al., 2015b] where they search for decorrelated modes of the quasi-geostrophic liquid core flow.

Let \mathbf{X} be the data matrix with snapshots of gridded data values:

$$\mathbf{X} = \begin{bmatrix} X_{1,1} & X_{1,2} & \cdots & X_{1,n} \\ X_{2,1} & X_{2,2} & \cdots & X_{2,n} \\ \vdots & \vdots & \ddots & \vdots \\ X_{m,1} & X_{m,2} & \cdots & X_{m,n} \end{bmatrix} \quad (4.1)$$

where $X_{i,j}$ is the data value attributed to grid point j at epoch i . Index j takes values from 1 to the total number n of grid points, and index i takes values from 1 to the total number m of epochs considered in the analysis. The PCA identifies spatial features of a certain, measured, scalar field that evolve correlated in time. Such spatial structures (EOFs) are the eigenvectors of the covariance matrix $\mathbf{C}_X = \mathbf{X}^T \mathbf{X}$, real and symmetric. We denote \mathbf{P} the matrix that has the eigenvectors of \mathbf{C}_X as columns, ordered according to the amplitude of (real, positive) eigenvalues of \mathbf{C}_X , and \mathbf{U} the matrix with eigenvectors of $\mathbf{X}\mathbf{X}^T$ as columns. Both \mathbf{P} and \mathbf{U} are orthogonal matrices that factorize \mathbf{X} according to:

$$\mathbf{X} = \mathbf{U}\mathbf{\Lambda}\mathbf{P}^T \quad , \quad (4.2)$$

known as Singular Value Decomposition (SVD) of \mathbf{X} . Matrix $\mathbf{\Lambda}$ is a $m \times n$ rectangular diagonal matrix, with all entries $\Lambda_{i,j}$ with $i \neq j$ being zero and all entries $\Lambda_{i,i}$ equal to the square roots of the eigenvalues of \mathbf{C}_X (or singular values of \mathbf{X}), ordered from the highest to the lowest. Matrix $\mathbf{A} = \mathbf{X}\mathbf{P} = \mathbf{U}\mathbf{\Lambda}$ is the matrix of amplitudes. Denoting A^k the k th column of \mathbf{A} and P^k the k th row of \mathbf{P}^T (or transpose of k th column of \mathbf{P}), then the data matrix can be decomposed into n PCA modes according to:

$$\mathbf{X} = \sum_{k=1}^n A^k \otimes P^k \quad (4.3)$$

where the symbol ' \otimes ' denotes the dyadic product between column vector A^k and row vector P^k . A^k is the k^{th} -order PC: the vector with amplitudes of PCA mode- k for the whole time interval analysed, with high (positive or

negative) coefficient values at epochs when mode- k has a strong inprint. P^k is the k th-order EOF: the spatial pattern localising the geographic regions that take part in mode- k .

The PCA modes are also named ‘variability’ modes, because of the role of P^k eigenvectors in the spectral decomposition of the variance-covariance matrix \mathbf{C}_X . The percentage of variability (or variance) accounted for by mode- k in this decomposition is [Hannachi et al., 2007]

$$f_k = \frac{100 \Lambda_{k,k}^2}{\sum_{i=1}^n \Lambda_{i,i}^2} . \quad (4.4)$$

Note that mode- k contributes to \mathbf{C}_X spectral decomposition with weight $\Lambda_{k,k}^2$ and to the PCA decomposition of \mathbf{X} with weight $\Lambda_{k,k}$.

Lawley’s formula and the North’s rule of thumb [North et al., 1982] can be applied in order to determine the error associated with each variability mode, as a result of choosing a given sample for the analysis (a set of time epochs) instead of some other sample.

Let $\lambda_i = \Lambda_{i,i}^2$. Following [North et al., 1982], I use as the sampling error in λ_i :

$$\delta_{\lambda_i} \approx \lambda_i \sqrt{2/m}, \quad (4.5)$$

where m is the number of epochs in the analysis, and for the sampling error in P^i

$$|\delta_{P^i}| \approx \frac{\delta_{\lambda_i}}{|\Delta\lambda_i|} P^i \quad (4.6)$$

where $\Delta\lambda_i = \lambda_i - \lambda_j$ with $\lambda_j (j \neq i)$ one other eigenvalue of C_X , the one closest to λ_i . The error δ_{λ_i} was propagated to the calculation of f_i .

4.2 PCA applied on vector data

During the course of this work, PCA will be applied to data of both scalar and vectorial fields. In the first study, each individual snapshot will correspond to a single measurement grid of scalar measurements, which in this

case is the particle flux count of high energetic protons at a given epoch. I will call it scalar PCA. In this case, the application of PCA follows closely the approach as presented in section 4. In the second study, a vector quantity (the geomagnetic field) will be analysed, for which 3 scalar quantities (Earth-centered spherical components B_r , B_θ , B_ϕ) are given at a certain grid distribution, for a given epoch. This requires a slight variation of the standard PCA method in order to take into account the three variables. I will call it vectorial PCA. [Shore et al., 2016] use this approach. In case of a non-uniform distribution, the weighting scheme is very important. As our distribution is close to uniform, the weighing can be considered to be 1 as all latitude and longitudes are equally represented.

Even if a weighing factor is not required, we need to normalise the resulting PCA modes in case of vectorial PCA. Each PCA mode k assigns a certain time function A^k to spatial structure P^k , that in the case of vectorial PCA has dimension $1 \times 3n$, i.e.,

$$P^k = \begin{bmatrix} P_{B_r}^k & P_{B_\theta}^k & P_{B_\phi}^k \end{bmatrix}$$

where P_i^k ($i = B_r, B_\theta, B_\phi$) is the $1 \times n$ row vector of component- i values on the grid in mode k . Condition $P^k(P^k)^T = 1$ applies to the whole EOF and different components contribute differently. I have normalised each P_i^k separately, in order that $P_i^k(P_i^k)^T = n$. To this end,

$$A_i^k = A_i^k F_i^k \tag{4.7}$$

$$P_i^k = P_i^k \frac{1}{F_i^k} \tag{4.8}$$

where

$$F_i^k = \sqrt{P_i^k(P_i^k)^T} \frac{1}{\sqrt{n}} \tag{4.9}$$

F_i^k is the normalisation factor for mode k and n the number of grid points, as before.

The criteria used for the normalisation is that the spatial average of each component is equal to 1, for each mode. Having made this normalisation allows for the amplitude of the time series to be directly interpreted as the actual value of the field average at a certain time.

4.3 PCA modes with and without the mean

In $m \times n$ data matrix \mathbf{X} , each row may be seen as a set of n random variables for which there are m realizations. We can define n variances and $n(n-1)/2$ covariances between these variables, and arrange these values as coefficients of a covariance symmetric matrix. Strictly speaking, a covariance matrix is supposed to be built after elimination of the mean of each random variable. In section 4 and for the sake of simplicity following several authors, we called covariance matrix \mathbf{C}_X the $n \times n$ matrix $\mathbf{X}^T \mathbf{X}$ where means have been kept and looked for EOF's that are eigenvectors of this matrix. The question naturally arises as how this changes the variability modes. To clarify this point, let \mathbf{C}_X be the 'real' covariance matrix (without the mean of each random variable) and $\mathbf{S} = \mathbf{X}^T \mathbf{X}$. Using a notation closer to that in [Jolliffe, 2002], let \mathbf{x}' be the $n \times 1$ column vector of deviations of each random variable relative to corresponding means. In this work, each random variable is a geophysical field measured at a given grid point. For each epoch i there will be a different realization of the set of n variables, which is called \mathbf{x}'_i . Then, the set of all m realizations can be arranged as a data matrix that differs from \mathbf{X} only because the mean of each column has been removed:

$$\mathbf{X}' = \begin{bmatrix} - & \mathbf{x}'_1{}^T & - \\ - & \mathbf{x}'_2{}^T & - \\ & \vdots & \\ - & \mathbf{x}'_m{}^T & - \end{bmatrix} \quad (4.10)$$

Then

$$\mathbf{C}_X = \sum_{i=1}^m \mathbf{x}'_i \mathbf{x}'_i{}^T = \mathbf{X}'^T \mathbf{X}' \quad (4.11)$$

where $\mathbf{ab}^T = \mathbf{a} \otimes \mathbf{b}$ is the outer product of the two vectors \mathbf{a} and \mathbf{b} . PCA can be seen as the calculation of the orthogonal transformation \mathbf{P}' applied to \mathbf{X}' such that

$$\mathbf{Z}' = \mathbf{X}'\mathbf{P}' \quad (4.12)$$

with

$$\mathbf{Z}' = \begin{bmatrix} - & \mathbf{z}'_1{}^T & - \\ - & \mathbf{z}'_2{}^T & - \\ & \vdots & \\ - & \mathbf{z}'_m{}^T & - \end{bmatrix} \quad (4.13)$$

and $\mathbf{z}'_i{}^T = \mathbf{x}'_i{}^T\mathbf{P}'$. The conditions imposed to determine \mathbf{P}' are that (e.g. [Jolliffe, 2002]):

- i) the variance of each element of \mathbf{z}' (each transformed random variable) be maximized;
- ii) the off-diagonal coefficients of \mathbf{Z}' be zero;
- ii) the columns of \mathbf{P}' , let them be \mathbf{p}'_i ($i = 1, \dots, n$), be orthonormal.

The first condition yields, for the first element of \mathbf{z}' , that $\sum_{i=1}^m (z'_{i,1})^2$ be a maximum. This variance can be written as

$$\sum_{i=1}^m (\mathbf{x}'_i{}^T \mathbf{p}'_1)^2 = \sum_{i=1}^m \mathbf{p}'_1{}^T \mathbf{x}'_i \mathbf{x}'_i{}^T \mathbf{p}'_1 = \mathbf{p}'_1{}^T \left(\sum_{i=1}^m \mathbf{x}'_i \mathbf{x}'_i{}^T \right) \mathbf{p}'_1 = \mathbf{p}'_1{}^T \mathbf{C}_X \mathbf{p}'_1 \quad (4.14)$$

To find the maximum of $\mathbf{p}'_1{}^T \mathbf{C}_X \mathbf{p}'_1$ subject to the normalization condition $\mathbf{p}'_1{}^T \mathbf{p}'_1 = 1$, we derivate the Lagrangian function

$$\mathcal{L}' = \mathbf{p}'_1{}^T \mathbf{C}_X \mathbf{p}'_1 - \lambda'_1 (\mathbf{p}'_1{}^T \mathbf{p}'_1 - 1) \quad (4.15)$$

with respect to \mathbf{p}'_1 , where λ'_1 is a Lagrange multiplier. This leads to

$$(\mathbf{C}_X - \lambda'_1 \mathbf{I}) \mathbf{p}'_1 = 0 \quad (4.16)$$

showing that \mathbf{p}'_1 is an eigenvector of \mathbf{C}_X . Besides, as $\mathbf{C}_X \mathbf{p}'_1 = \lambda'_1 \mathbf{p}'_1$ and $\mathbf{p}'_1{}^T \mathbf{C}_X \mathbf{p}'_1 = \mathbf{p}'_1{}^T \lambda'_1 \mathbf{p}'_1 = \lambda'_1$ is maximum, λ'_1 is the largest eigenvalue of \mathbf{C}_X . The other columns of \mathbf{P}' are derived as explained in Jolliffe (2002). Let us now clarify how using \mathbf{S} instead of \mathbf{C}_X changes the eigenvectors and eigenvalues. In computing the first eigenvector, the Lagrangian function is now

$$\mathcal{L} = \mathbf{p}'_1{}^T \mathbf{S} \mathbf{p}'_1 - \lambda_1 (\mathbf{p}'_1{}^T \mathbf{p}'_1 - 1) \quad (4.17)$$

where $\mathbf{S} = \sum_{i=1}^m \mathbf{x}_i \mathbf{x}_i{}^T$ and $\mathbf{x}_i = \mathbf{x}'_i + \bar{\mathbf{x}}$. Here, $\bar{\mathbf{x}}$ is the vector of mean values of all n random variables. Taking the derivative of the Lagrangian function with respect to \mathbf{p}'_1 and equating to zero yields

$$(\mathbf{S} - \lambda_1 \mathbf{I}) \mathbf{p}'_1 = 0 \quad (4.18)$$

We can re-write

$$\begin{aligned} S &= \sum_{i=1}^m \mathbf{x}_i \mathbf{x}_i{}^T = \sum_{i=1}^m (\mathbf{x}'_i + \bar{\mathbf{x}})(\mathbf{x}'_i + \bar{\mathbf{x}})^T \\ &= \sum_{i=1}^m \mathbf{x}'_i \mathbf{x}'_i{}^T + \sum_{i=1}^m \bar{\mathbf{x}} \bar{\mathbf{x}}^T + \sum_{i=1}^m \mathbf{x}'_i \bar{\mathbf{x}}^T + \sum_{i=1}^m \bar{\mathbf{x}} \mathbf{x}'_i{}^T \\ &= \mathbf{C}_X + m \bar{\mathbf{x}} \bar{\mathbf{x}}^T \end{aligned}$$

using the definition of \mathbf{C}_X and the fact that $\sum_{i=1}^m \mathbf{x}'_i = 0$. The eigenvector-eigenvalue equation for \mathbf{S} can then be written as:

$$(\mathbf{C}_X + m \bar{\mathbf{x}} \bar{\mathbf{x}}^T - \lambda_1 \mathbf{I}) \mathbf{p}'_1 = 0 \quad (4.19)$$

The symmetric matrix of the mean, $\bar{\mathbf{x}} \bar{\mathbf{x}}^T$, has the following property:

$$(\bar{\mathbf{x}} \bar{\mathbf{x}}^T) \bar{\mathbf{x}}_{norm} = \|\bar{\mathbf{x}}\|^2 \bar{\mathbf{x}}_{norm} \quad (4.20)$$

where $\bar{\mathbf{x}}_{norm} = \frac{\bar{\mathbf{x}}}{\|\bar{\mathbf{x}}\|}$ and $\|\bar{\mathbf{x}}\| = \bar{\mathbf{x}}^T \bar{\mathbf{x}}$. That is, $\bar{\mathbf{x}}_{norm}$ is eigenvector of $\bar{\mathbf{x}} \bar{\mathbf{x}}^T$ with eigenvalue $\|\bar{\mathbf{x}}\|^2$ and norm 1. Two different cases can be considered, both relevant in the context of this study.

4.3.1 The vector of mean values is an eigenvector of \mathbf{C}_X

Let $\bar{\mathbf{x}}_{norm}$ be an eigenvector of \mathbf{C}_X , of some order k , such that $\mathbf{C}_X \bar{\mathbf{x}}_{norm} = \lambda'_k \bar{\mathbf{x}}_{norm}$. Then using S instead of \mathbf{C}_X will not change the EOFs but will change the eigenvalue associated with mode- k , from λ'_k to $\lambda'_k + m \|\bar{\mathbf{x}}\|^2$. This may be significant in terms of ordering of principal modes. If $\|\bar{\mathbf{x}}\|$ is high, the mode associated with the mean values turns into the main one. That is what happens in the proton flux case, where a spatial structure very close to the mean was already present when using \mathbf{C}_X , but was not the first mode.

4.3.2 The symmetric matrix of the mean is much larger than \mathbf{C}_X

In the case the elements of the symmetric matrix of the mean are much larger than those of \mathbf{C}_X , we may write:

$$\mathbf{C}_X + m \bar{\mathbf{x}} \bar{\mathbf{x}}^T \approx m \bar{\mathbf{x}} \bar{\mathbf{x}}^T \quad (4.21)$$

The principal PCA mode when using \mathbf{S} is then characterized by an EOF equal to \mathbf{x}_{norm} with associated eigenvalue $m \|\bar{\mathbf{x}}\|^2$ which is very high. The associated time function (PC) is obtained from the first column of \mathbf{Z} ($\mathbf{Z} = \mathbf{X}\mathbf{P}$, where the 'plicas' have been removed when using \mathbf{S} instead of \mathbf{C}_X . Note that in section 4 we use \mathbf{A} instead of \mathbf{Z}). Each element i of the first column of \mathbf{Z} is obtained from $z_{i,1} = \mathbf{x}_i^T \mathbf{p}_1$, where $\mathbf{p}_1 = \bar{\mathbf{x}}_{norm}$. By construction, $\bar{\mathbf{x}}_{norm}$ is present in the data matrix and the projection will always be non-zero. In the case of a high mean, the projection coefficients will be high. However, if the mean was not present as a mode of \mathbf{C}_X (a true 'variability mode'), we should expect a weak time variation. The following steps to compute modes of order 2 and above, work on the data matrix after the first mode (the mean) has been subtracted. We then fall into the case of PCA using \mathbf{C}_X and obtain as EOFs 2,3, ... the sequence of ordered eigenvectors 1,2, ... of \mathbf{C}_X . This case is the one we face when analysing main field data. $\bar{\mathbf{x}}_{norm}$ is the first mode because of the very high mean (main field) compared to variations (secular

variation). But it is also very nearly orthogonal to the eigenvectors of \mathbf{C}_X and does not modify significantly the following modes.

Chapter 5

Application of PCA to the SAA

This section is largely based on our article published in Earth and Planetary Science Letters with the title "The South Atlantic Anomaly throughout the solar cycle".

5.1 Reference frames

As mentioned before, one way to analyse and track the evolution of the SAA is to monitor the location and orientation of the eccentric dipole. This is done by selecting the spherical harmonics up to degree 2 of a given magnetic field model, namely CHAOS-6 in this study. Departure of the eccentric dipole from an axial dipole suffices to explain the main part of the SAA, although there are some slight differences in its shape. In fact, a westward drift of the anomaly of about $0.3^\circ/\text{yr}$ is retrieved from the movement of the eccentric dipole, which is consistent with estimates obtained directly from particle flux data [Fürst et al., 2009, Noel et al., 2014, Schaefer et al., 2016]. It is enlightening to describe the anomaly in this way, since the interaction of charged particles with the main field can then be considered in a dipole field geometry (though tilted and displaced from the Earth's center). In this study we took advantage of this feature to construct a reference frame that gets rid of effects due to changes of the tilt and/or the center of the main field dipole and concentrates on effects that can be explained using the

well-known dynamics of charged particles trapped in a dipolar magnetic field [Vernov et al., 1967, Gledhill, 1976].

5.1.1 Eccentric dipole reference frame

Some tests have been carried out in the search for an adequate reference frame, one that on the one hand can minimise the complexity of our solutions, and on the other hand can properly characterize the main spatial and temporal features of the SAA using the PCA method. Using a regular geographic latitude-longitude grid we found that a patch of particle flux can be detected at times of high solar activity in a region south of the anomaly (see Figure 5.1).

To remove this patch of the particle flux, not relevant for this study, and not crop any portion of the SAA patch, a new latitude-longitude grid with the orientation based on the inclination and displacement of the eccentric dipole was used, the 'dipole reference frame'. Contours of this grid can be seen in figure 5.1, overlaid on top of a snapshot of the POES particle flux data, to compare with the regular geographic latitude-longitude grid (vertical and horizontal lines). In this particular snapshot of POES particle flux for December 2014, we can see the undesirable particle flux region south of the anomaly, and the way the dipole reference frame allows to crop around it. To account for the displacement of the eccentric dipole, this reference frame was recalculated for each instance of the particle flux data, using the CHAOS-6 model. In this way, the frame follows the movement of the anomaly, at least that component due to the secular change of the main field.

5.1.2 L-shell reference frame

Here we use the *a priori* knowledge that trapped particles drifting in a certain L-shell have their lowest altitude mirror points where the magnetic field intensity is also minimum [Gledhill, 1976]. This suggests that the most physically meaningful coordinates to map the particle flux data are L and the field

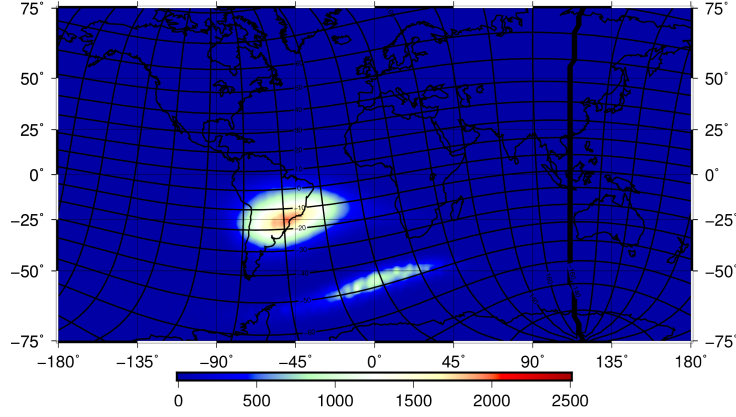


Figure 5.1 – POES particle flux data for December 2014 with eccentric dipole grid representation overlaid.

intensity $|\mathbf{B}|$. In a dipole field, L values can be calculated as,

$$L = \frac{r}{\cos^2 \lambda}, \quad (5.1)$$

where r is the distance in Earth radii to each point in the field line, from the Earth's center, and λ is the geomagnetic latitude, computed based on the eccentric dipole approximation (dipole and quadrupole spherical harmonic coefficients). As in section 5.1.1, the grid values (in this case L and $|\mathbf{B}|$) were recalculated for each instance of the particle flux data. This representation identifies each particular magnetic field line by the distance in Earth radii when it crosses the magnetic equator. When considering all field lines with the same L value, we construct L-shells. These shells of toroidal shape circle the Earth and are organized about the axis of the eccentric dipole. Due to the dipole displacement with respect to the Earth's center, there are L-shells that intersect constant altitude surfaces in some angles of longitude only, representing an area where the L-shell is located beneath the considered altitude.

The L-shells description is appropriate to discuss the particle flux in the upper atmosphere. Trapped charged particles, such as protons and electrons move along L-shells, bouncing between mirror points north and south of the magnetic equator, and drifting around the Earth. It is a useful simplification to consider separately the particle flux in different L-shells. The particle flux

distribution is related to the Sun's activity, and varies according to the solar cycle [Vacaresse et al., 1999]. Because the trapped particle motions are well described in terms of L-shells, it seems logical to study the evolution of the particle flux using the L-shell representation.

In order to properly describe the particle flux, we need another parameter besides the L value. Although a charged particle population can be associated with each L-shell, the mirror points for the particles motion depend on longitude. As we discussed before, the magnetic field intensity affects the penetration of energetic particles, and so, for each L line at a certain altitude, a higher particle flux is expected where the magnetic field has its minimum. With this in mind, we have drawn the location of the minimum magnetic field intensity as a function of L and from this contour we have been able to define a new coordinate.

In figure 5.2 we can see a step by step representation of the reference frame construction. In order to properly map the region of interest, certain L-shells had to be removed, namely the ones that did not properly cover the entire longitudinal range. At the altitudes concerned by our data we removed all lines with $L < 1.22$ (figure 5.2, b). A set of 12 lines were drawn to fill the void left by the removed L contours (figure 5.2, c). This was done by interpolating linearly the difference between the two innermost L-shells for each fixed longitude value. For each one of L contours and interpolating lines, which globally define the L coordinate, we located the point of minimum field intensity, as calculated using the CHAOS-6 model up to degree 13. The set of all these points gives the thick red line on figure 5.2, d. Finally, a set of lines were drawn, shifted from the minimum $|B|$ contour by a multiple of $B_{step} = \Delta|B|$, in both East and West directions. They define the B coordinate according to:

$$B_i^j = B_{min}^j \pm B_{step} i^2 \quad (5.2)$$

where B_i^j is the value of $|B|$ in L shell j (L_j) in position i away from the centre line. B_{min}^j is the minimum $|B|$ value for line L_j and B_{step} is a constant to set the spacing of the B grid coordinate. The increments of B defining the

5.2. SOUTH ATLANTIC ANOMALY THROUGHOUT THE SOLAR CYCLE67

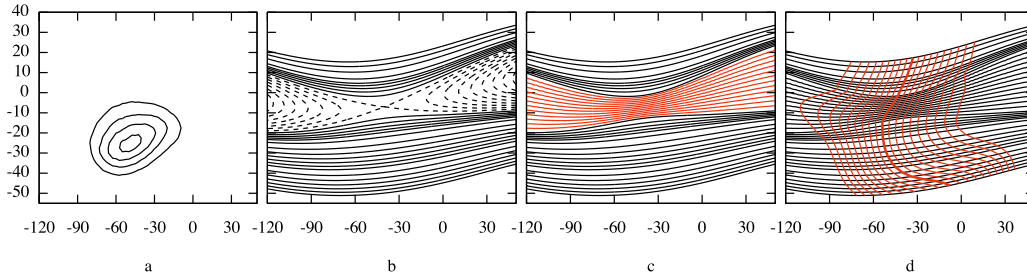


Figure 5.2 – Contours of the particle flux anomaly (a). Representation of the L-shell reference frame construction process: removal of $L < 1.22$ contours as shown by dashed lines (b); new lines defined by interpolating lines in red (c); vertical axis created from thick red line of $|B|_{min}$ together with other $|B|$ contour lines (d).

grid have been customised to the variation of B near its minimum (where $\partial B/\partial i = 0$) on each L line.

Both grids define a new coordinate system (the 'L-shell reference frame') for the region where the SAA is located, covering $[-135^\circ:45^\circ]$ in longitude and $[-50^\circ:25^\circ]$ in latitude. The approximate average grid spacing is 2.5° . Note that this domain of coordinates is not that represented in figure 5.2.

5.2 South Atlantic Anomaly throughout the solar cycle

When applying the PCA method, we can choose to either keep or remove the mean particle flux at each grid point, averaged over the whole time interval. In this study we have chosen to represent and discuss the results with the mean flux distribution retained in the calculation, since this leads to a clearer interpretation of results, enabling a better description of the physical source for each mode (see section 4).

The particle flux data from the POES satellite, for the period between 1998 and 2014, have been analysed. Figure 5.3 shows the spatial structures (or EOFs) of the first three modes obtained through the PCA decomposition of the data using the dipole grid described in section 5.1. Each of the three modes shows interesting spatial and temporal structures, which can be understood in the light of physical mechanisms involving trapped radiation. All

together, they explain more than 99.9% of the total data variability (see eq. 4.4). The first mode shows a (monopolar) structure of particle flux intensity (figure 5.3(a)) with the same shape as the mean SAA and an associated time oscillation between a maximum and a minimum of intensity (figure 5.5(a)).

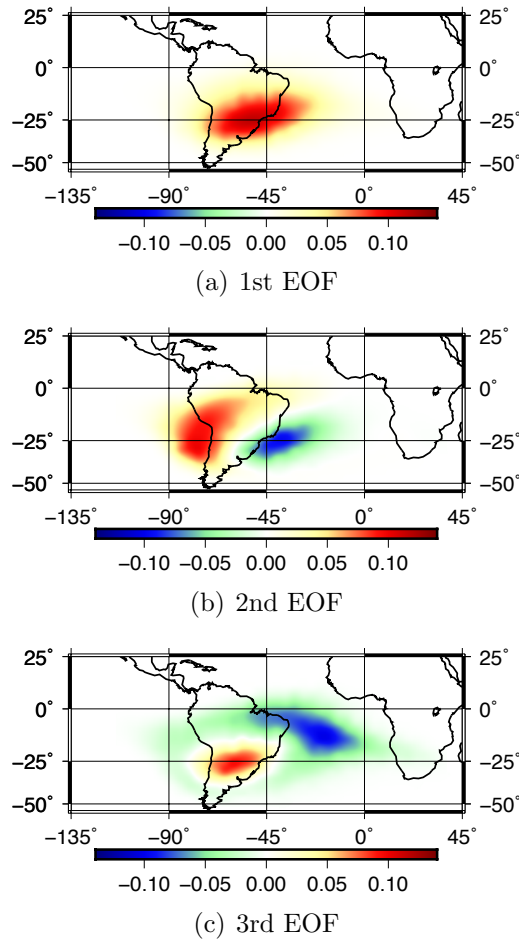


Figure 5.3 – The first three spatial patterns from the PCA analysis of POES data between 1998 and 2014, using the dipole reference frame and represented in the regular geographic grid. The x-axis is longitude and y-axis latitude. Percentage of variability, f_i , from the first to the last: 99.46, 0.38 and 0.11.

The second mode, showing a bipolar spatial structure (figure 5.3(b)), represents a superposition of a steady westward drift and an oscillation of about 11yr period (figure 5.5(a)). The amplitude of variation of mode 1 is just about a factor 2 larger than that of mode 2, both modes showing a time oscillation with approximately an 11-year period. Keeping the time average

helps to define the spatial structure of mode 1 (which is also present in the mean) thus allowing for a better separation of modes 1 and 2. Finally, a change in the geometry of the anomaly can be represented by the third mode (figure 5.3(c)). As we show below, this mode can be significantly reduced in terms of its fraction of variability, if the more adequate L-shell reference frame is used.

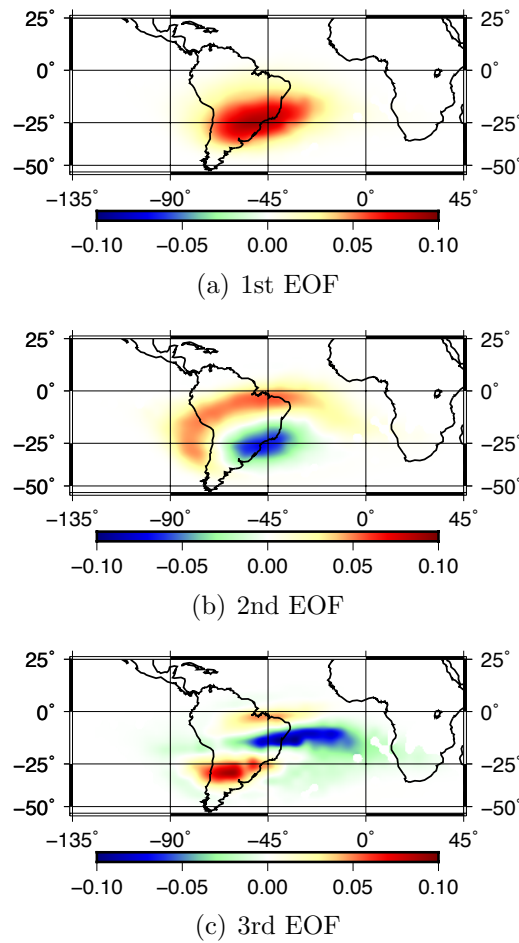
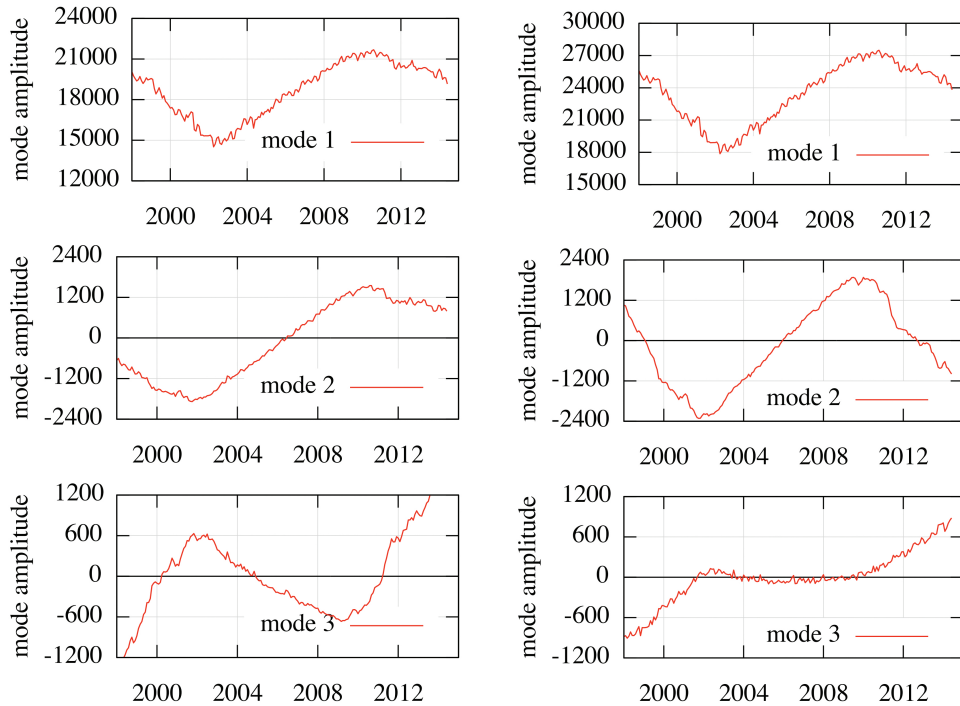


Figure 5.4 – The first three spatial patterns from the PCA analysis of POES data between 1998 and 2014, using the L-shell reference frame and represented in the regular geographic grid. The x-axis is longitude and y-axis latitude. Percentage of variability, f_i , from the first to the last: 99.64, 0.28 and 0.02.

When analysing the decomposition of the same data, but using the L-shell reference frame (figure 5.4), the first mode (figure 5.4(a)) is much the same, with an identical time series (figure 5.5(b)). This has been expected as

the change of reference frame does not affect the calculation of the total flux. The second mode, which reflects motions of the anomaly, strongly depends on the reference frame and the grid choice. Both its spatial structure (figure 5.4(b)) and its evolution are affected. We note in section 5.2.2 below that calculating this mode on the L-shell reference frame is the appropriate way to understand its origin. The third mode is also very different in the two reference frames. This might have been expected because it accounts for geometrical variations of the anomaly and the transformation between the dipole and the L-shell reference frames introduces distortions. The third mode in the L-shell reference frame has a clear tripolar structure. Most of the variability of the anomaly is represented by the first two modes and the third mode is significantly less energetic when calculated on the L-shell reference frame (0.02% of the variability) than when calculated on the dipole reference frame (0.11% of the variability).



(a) PCs using the dipole reference frame. (b) PCs using the L-shell reference frame.

Figure 5.5 – Time series corresponding to modes in figures 5.3 and 5.4 for the POES particle flux data. The x-axis is in years.

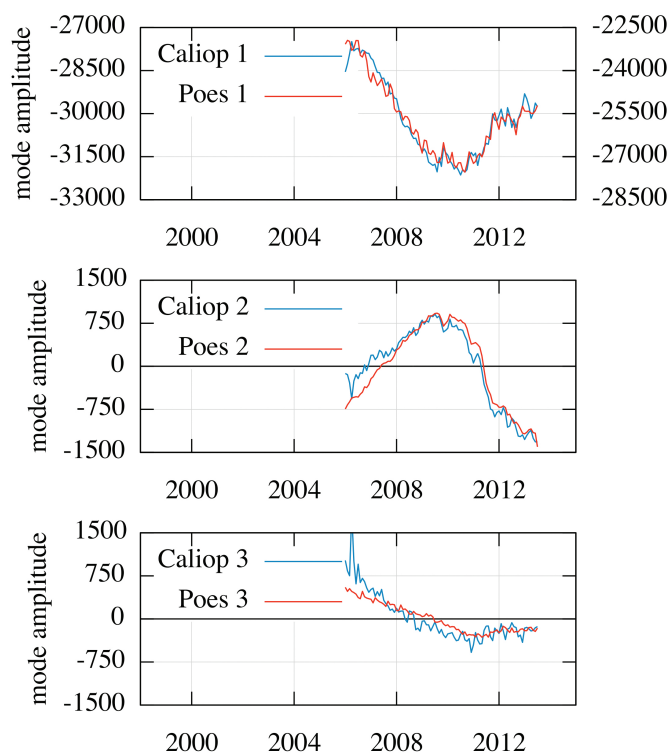


Figure 5.6 – Modes amplitude for CALIOP dark noise data and POES particle flux data for the same time interval. The x-axis is in years.

Applying PCA to only that data from POES that is concurrent with the CALIOP data, the modes and time series (see figure 5.6) closely match. This leads us to believe that with a long enough time series, the dark noise data could be interpreted in the same way as particle flux data.

5.2.1 The first mode: modulation of the global flux of trapped protons by the solar cycle

The first mode of either one of PCA decompositions is related to the global increase and decrease of particle flux in the inner Van Allen belt. On the top of figure 5.5(b) we can see the time series of the first mode from the PCA decomposition of the POES data. Comparing the time variation of this mode with the thermospheric density evolution (figure 5.7), we can clearly see the response of the flux of particles to the evolution of the thermospheric density.

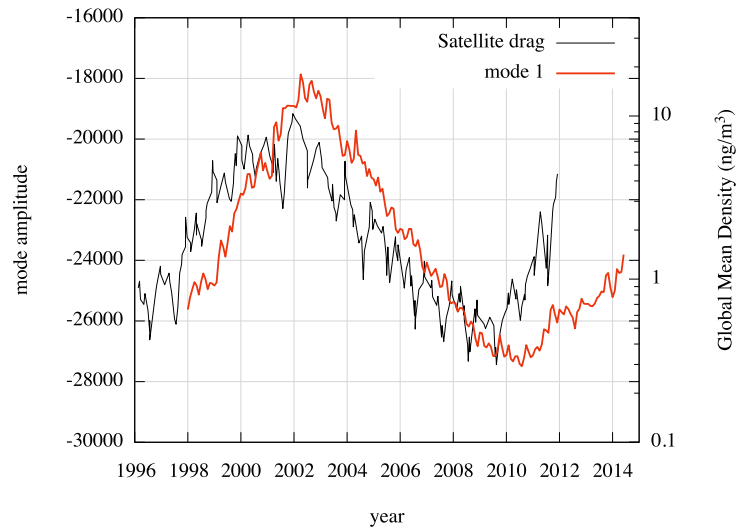


Figure 5.7 – Time series of the first PCA mode of POES L-shell reference frame and the thermospheric density. Atmospheric data retrieved from [Solomon et al., 2013].

Thermospheric density is directly correlated with the Sun’s activity, as a result of heating driven by solar radiation, showing the same time evolution as the solar cycle [Solomon et al., 2013]. Density increase at high altitude, as the atmosphere expands during solar maxima, leads to more frequent collisions between the trapped energetic protons and atmospheric atoms. As a result, the trapped proton stocks are depleted during maxima of the solar cycle. We identified a 17 month lag between the time series of the first mode and the thermospheric density variation (see figure 5.7).

5.2.2 The second mode: bipolar oscillation in the location of the maximum of proton flux

As seen in the two PCA decompositions from POES particle flux data with the different grid choices, the second mode is also enslaved to the solar cycle. There is a clear oscillation in the time series (figures 5.5(a) and 5.5(b)), following the solar cycle. The internal field is responsible for a westward drift of the anomaly, which can be seen in the time series in figure 5.5(a), superimposed with an oscillation. This trend is already slightly removed by using a reference frame that follows the evolution of the eccentric dipole

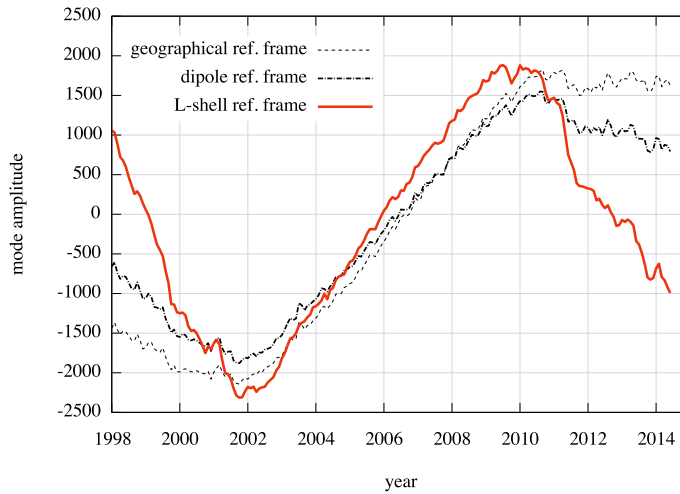


Figure 5.8 – Time series of the second mode for POES: comparison between a regular geographical grid (thinner dashed line), the dipole reference frame (thicker dashed line) and the L-shell reference frame (bold red line).

instead of the geographic frame. In the L-shell reference frame, this trend is almost completely removed (figure 5.5(b)). In figure 5.8 we can clearly see the gradual removal of the drift component with the choice of reference frame.

The dipole grid takes into account the westward movement of the eccentric dipole, but it is not able to properly account for the direction in which the particle flux moves. This movement is dictated by the location of the minimum intensity of the magnetic field in each L-shell. The L-shell reference frame takes into account exactly this, and we are able to almost completely separate the westward drift from the North-South oscillation driven by the Sun’s activity.

With the internal field westward motion almost entirely removed, the L-shell mode 2 shows a clear North-South behaviour. Over the solar cycle, different L-shells are differently populated by energetic particles. The shells with low L values are the most affected by depletion mechanisms during the solar maximum [Miyoshi et al., 2000]. As a result the maximum of the anomaly is then displaced towards a higher L value. This variation of L-shell population, together with the variation of the position of the minimum of the

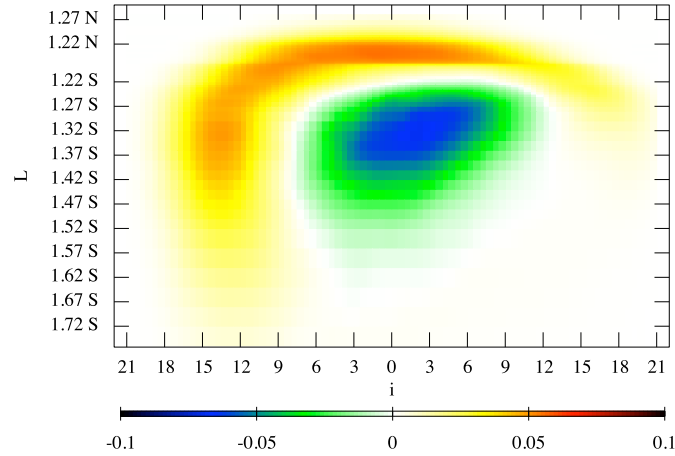


Figure 5.9 – The spatial patterns from the second mode of the PCA analysis of POES data between 1998 and 2014, using the L-shell reference frame and represented in the L - B_{min} grid. In this representation equation 5.2 is used, with i values ranging between 0-21 and the B_{step} equals 10.

magnetic field intensity in these L-shells [Vernov et al., 1967, Gledhill, 1976], leads to the oscillation represented by the second mode. A 10 month phase lag was obtained when the time series was compared with the thermospheric density variation.

In figure 5.9 the spatial pattern of the second mode is represented in the L - B_{min} space. Let us note that an abrupt change seems to separate the L-shells 1.22 N and 1.22 S. However, this is not a real feature, as in this region the interpolated L-shells have very close values of L whereas in the regular geographical space they have larger spacing. The break in the spatial pattern is the result of squeezing the smooth pattern in that region.

5.3 Discussion

Evolution of the SAA particle flux can be seen as the result of two main effects, the secular variation of the Earth’s magnetic field and the modulation of the protons density of the inner Van Allen radiation belt during the solar cycle. The internal geomagnetic field, due to a dynamo inside the

Earth's liquid core, is responsible for the observed westward drift. A main point coming out from this study is the identification of a reference frame, which we call L-shell reference frame, depending only on the main field. In this frame, the particle flux data can be decomposed into stationary modes with a physical interpretation in terms of mechanisms of feeding (CRAND, trapping/diffusion of solar protons) and depletion (nuclear collisions with atoms of the neutral atmosphere) of energetic protons inside the inner radiation belt. This provides for the separation of Earth's internal and external effects. We have identified the modes that represent changes in the SAA related to solar effects. Both the first and second modes have a good correlation with the thermospheric density, which varies with the solar cycle. The first mode represents the intensity variation of the global particle flux in the inner Van Allen belt. The second mode represents the movement of the peak of the proton flux between different L-shells. A different phase lag was identified when comparing both time series with thermospheric density evolution. A 17-month delay for the first mode and 10 months for the second. This difference is not necessarily a product of a small time resolution or the method itself. In fact, the particle flux in different L-shells responds to the solar cycle with different time lags [Miyoshi et al., 2000]. We have found that the position of the anomaly at solar maximum is 2.6° South and 0.9° East from its position at solar minimum. It corresponds to a change from $L = 1.32$ at solar minimum to $L = 1.35$ at solar maximum.

Once these modes are transformed back into the geographic frame, secular change of the main field combine with variations in the L-shells proton population. The westward drift rate as well as latitudinal and longitudinal solar cycle oscillations are well recovered in agreement with results from other recent studies [Qin et al., 2014]. In [Qin et al., 2014], they identify a 685 days time delay between the F10.7 solar index and the proton flux longitudinal evolution. They obtain these results studying protons with energies > 70 MeV, so no direct comparisons can be made with our results which focus on protons with energy > 16 MeV. By moving the reference frame together with the eccentric dipole, which represents the main part of the geomagnetic field, we account well for the westward motion of the anomaly. Conversely, on a

20 year time scale, the North-South movement is dominated by solar cycle effects. Investigating the location of the eccentric dipole in spherical coordinates, we note that its northward displacement in latitude has suddenly decreased from $0.069^\circ/\text{yr}$ to $0.014^\circ/\text{yr}$ in 2011, *i.e.* during the time interval investigated here. The associated particle flux change however remains small when compared to the oscillations of the anomaly during the solar cycle and cannot be detected. In contradiction with [Fürst et al., 2009] we conclude that rapid changes of the main field cannot be detected in particle flux measurements.

Our results hold for the 16.5 yr time interval of the analysis. In Chapter 6 we consider the effect of using a somewhat longer dataset. On secular and millennial time-scales, a prediction of the SAA evolution requires forecasts of the geometry and intensity of the geomagnetic main field and of the L-shell distribution of charged particles. [Aubert, 2015] has investigated the axial dipole decay and the place where the field is minimum at the Earth's surface for the next 100 years. In this study the spherical harmonic coefficients that most contribute to the cost function are the low order degree terms, precisely those that model the eccentric dipole. The question now is to infer how the flux of particles above the South Atlantic and South America will change in response to the evolution of the magnetic field. [Glassmeier et al., 2004] have shown that less particles can be trapped in a weaker magnetic field. We can also anticipate that interactions between protons trapped in the inner radiation belt and the thermosphere will increase as the SAA grows ([Roederer and Zhang, 2014]). Our time series are too short to detect a trend in the proton flux. We nonetheless think that the methods used in this work are appropriate to identify such a trend if applied to longer series. It would enable us to forecast the impact of the South Atlantic Anomaly on space weather.

Chapter 6

The evolution of the SAA over the last 30 years

6.1 POES extended time series

To allow for a better assessment of the impact of solar activity on the evolution of particle flux in the thermosphere, long time series are needed that cover several solar cycles. To comply with this requirement we joined 3 different datasets of particle flux data from different satellites. The satellites are all from the same series (POES NOAA) but they use different instruments for proton detection, SEM (for POES NOAA 10 and 12) and SEM-2 (for POES NOAA 15). Despite this difference, we consider it is possible to build a continuous series, as both detectors have a common energy range of >32 MeV, and all satellites orbit at similar altitudes, around 800 km.

Any two consecutive satellites were in operation at the same time over a given period, and this allowed us to adjust each series in order to get a continuous dataset. POES NOAA 10 and 12 have 3 months in common between June and August of 1991 and POES NOAA 12 and 15 have 15 months in common between July of 1998 and September of 1999. The three series showed different baselines. To join them, we considered the most recent one (POES NOAA 15) as the most reliable and multiplied each of the other two series by a factor to adjust them to follow the baseline of POES 15. For

this purpose, the total flux at each epoch belonging to both consecutive series was calculated. A factor was then computed that minimises the difference between the total flux values of the two series. This criterion guarantees the continuity of the total flux in the concatenated series. The following equation denotes this calculation.

$$Q_{min} = \sum_i^N (P_j^i - f_{j,k}P_k^i)^2 \quad , \quad j, k = 15, 12 \text{ or } 12, 10 \quad (6.1)$$

where, Q_{min} is the function to be minimized, N is the number of epochs present in both consecutive series, P_j^i is the total flux for epoch i from satellite j , and $f_{j,k}$ is the factor applied to the series P_k to bring it closer to P_j .

A shift of each series was not envisaged, besides the scaling, because certain values of the particle flux would become less than zero, which has no physical meaning. For this reason, only a multiplying factor could be used to join the series, instead of both an additive and multiplying factor as would be ideal in order to reduce the differences. Under these constraints, a factor $f_{12,10} = 1.0587$ was calculated to be applied to all the charts in POES NOAA 10 and a factor $f_{15,12} = 0.8263$ for POES NOAA 12. This produced a continuous series, as can be seen in figure 6.1 with 5-day average charts covering a period of 26 years.

Once a continuous series was available, spanning the 1986 to 2015 time interval, we computed 5-day average grids of the SAA in the L-shells reference frame (see section 5). The calculation in the L-shells grid removed many outliers by cropping the polar regions which have a sporadic activity and are not of interest in the study of the SAA. Despite this, some clear faulty results remained in the series, which could be addressed in a case by case correction, by removing the outliers and interpolating linearly. One further problem we faced was the absence of data for large periods of time. The largest gap was a period of 7 months in 1988, which was addressed by cropping the first 2.5 years of the series and considering the starting time in 1989 (1989-2015). The resulting normalised particle flux series can be seen in figure 6.1. After these corrections, the PCA method was applied to the concatenated series,

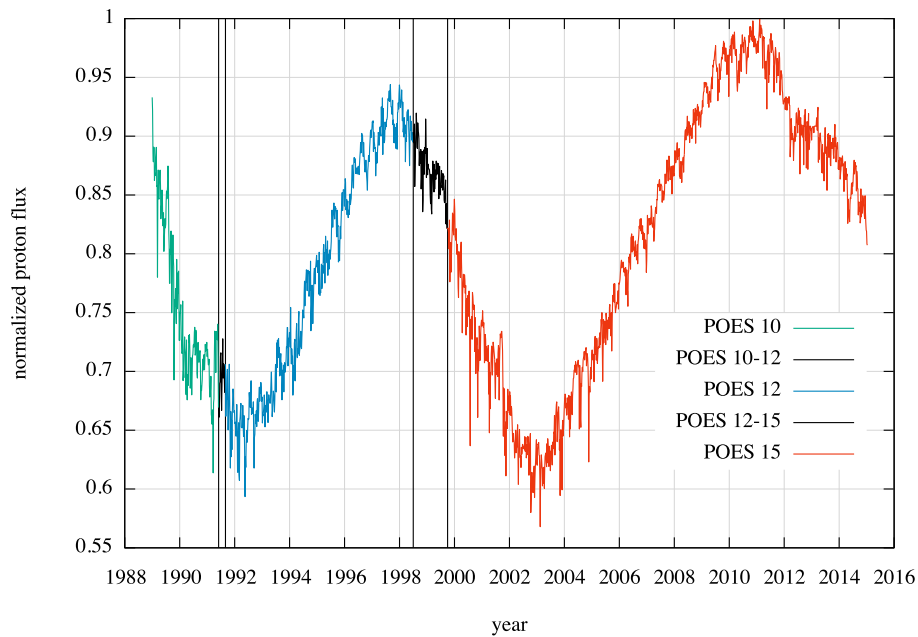


Figure 6.1 – POES 10,12,15 concatenated series with proton flux values normalized to 1. The vertical black lines represent the beginning and end of the time intervals of superimposed datasets.

with the results of the spatial modes shown in figures 6.2 and 6.3.

When looking at the PCA time functions from this extended series (figure 6.3), the apparent upward trend observed in the first mode and downward trend in the second mode are the most striking new results comparing with results obtained with a shorter dataset (chapter 5). Mode 3 seems to show the same behaviour as in the previous shorter time series. The spatial mode is very similar and the simple trend is the same. This mode corresponds to a gradual increase in the area of the anomaly, favouring a spread in the West direction. Several spikes are observed in the time intervals where the series are joined. For the first and second mode, previous time functions from a shorter dataset showed only an oscillation related with the solar cycle variation. This extended series provides evidence for the suspected trend debated in the previous chapter.

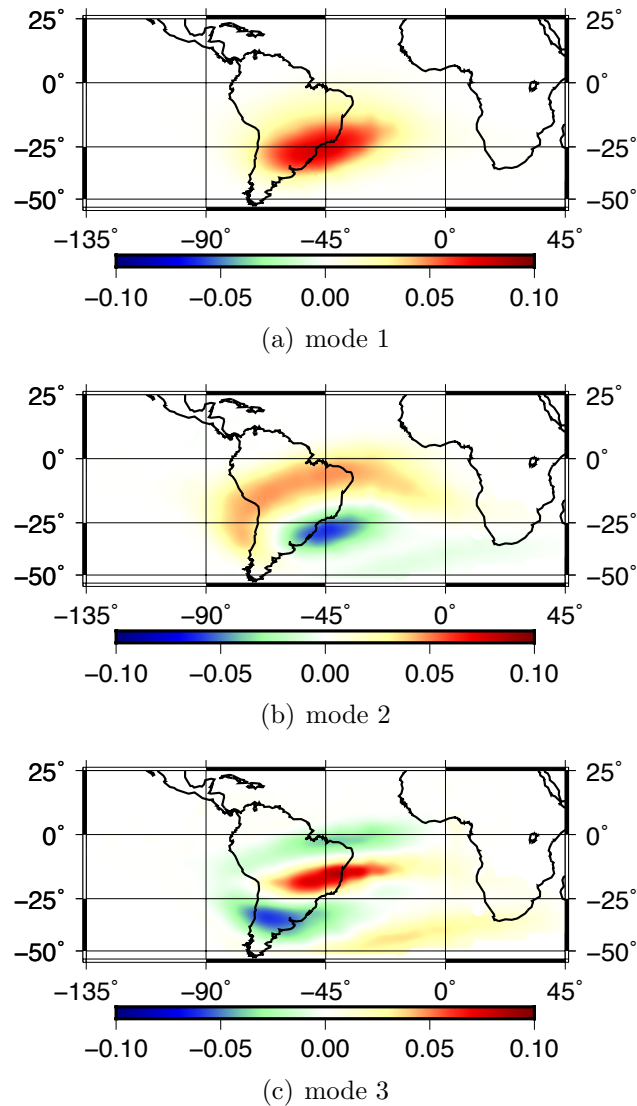
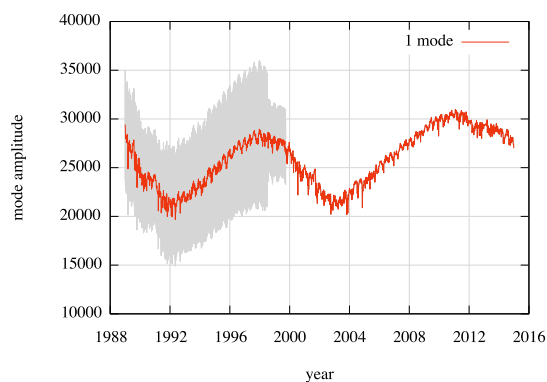
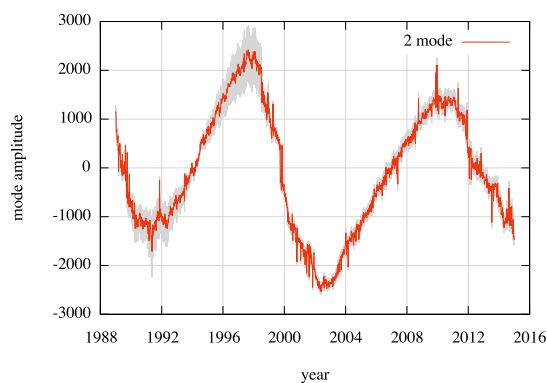


Figure 6.2 – First three PCA spatial modes for the POES 10,12,15 extended series. The x-axis is longitude and y-axis latitude. The fractions of variability of the three modes are 99.42%, 0.23% and 0.10% in order of importance.

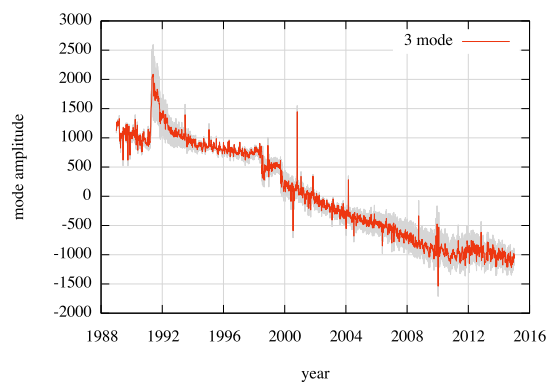
The trend in mode 1, shows up from imposing the continuity of the total flux series. As to the trend in mode 2, we must consider its robustness. Due to the construction process of the continuous series, the trend might appear only as an artifact due to a particular choice of multiplying factors. To test this possibility, a range of factors around the calculated best values was probed, in a total amount of 121 different combinations. 11 factors for each



(a) mode 1



(b) mode 2



(c) mode 3

Figure 6.3 – First three PCA time series for the POES 10,12,15 extended series. The grey region is the envelope from scanning the factors $f_{15,12}$ and $f_{12,10}$.

section were chosen between 0.8587 and 1.2587 for factor $f_{12,10}$ and between 0.6263 and 1.0263 for factor $f_{15,12}$, with a step of 0.04 between each one. To

investigate if this had any effect in the occurrence of the trend in mode 2, the PCA method was applied to all 121 resulting datasets. We then looked at the time series of all the second modes, which can be seen in figure 6.3(b). The envelope of results shows a clear trend regardless of the factors used to construct the initial series. This validates the presence of the trend in mode 2. Even in the region of the parameter space where the trend in mode 1 no longer exists, we still observe it in mode 2. The presence of such a trend in mode 2 even when sharp changes in total flux intensity are considered is not a surprise. This mode represents the displacement of the anomaly, and this does not change with the baseline of flux intensity. The only mode affected by these sharp changes in the total flux intensity during the test is mode 1, as it is the only mode that represents the variation of intensity.

In [Emmert, 2015], a linear trend in thermospheric density is observed, as we can see in figure 6.4. As we have already underlined in chapter 5, the variation of the thermospheric density is anticorrelated with the particle flux content and distribution in the same region. [Emmert, 2015] relates the contraction of the thermosphere with the increase in CO₂ in the atmosphere. CO₂ build up in the stratosphere and above, where absorption of infrared radiation is not saturated, causes a cooling effect due to infrared re-emission of energy received from the Sun. It leads to an effect similar to a decrease in solar activity, as during the minima of solar cycles. Note that the presence of CO₂ in the lower and denser troposphere has the opposite effect of warming it up, as predicted from radiative equilibrium, due to the transfer of the absorbed energy by collisions, instead of radiation to the outer space [Emmert et al., 2012, Andrews et al., 1987]. The trend in the particle flux detected over the SAA, clearly identified using the PCA method, may be related with the known trend in thermospheric density.

In mode 1, the trend corresponds to an increase in the intensity of the SAA particle flux, as would be expected from a contraction of the thermosphere. The sign of the trend in mode 2, seems to be contradictory with the explanation given in chapter 5 for this mode. A decrease in thermospheric density should be followed by a population increase in the lower L shells, as observed during minima of solar activity, but this is not what is observed.

Here, the trend is apparently associated with a displacement towards higher L shells. In order to identify the exact origin of this trend, a test was applied to find out if this trend could be identified with a movement in the L shells on the top of the intensity variation already established.

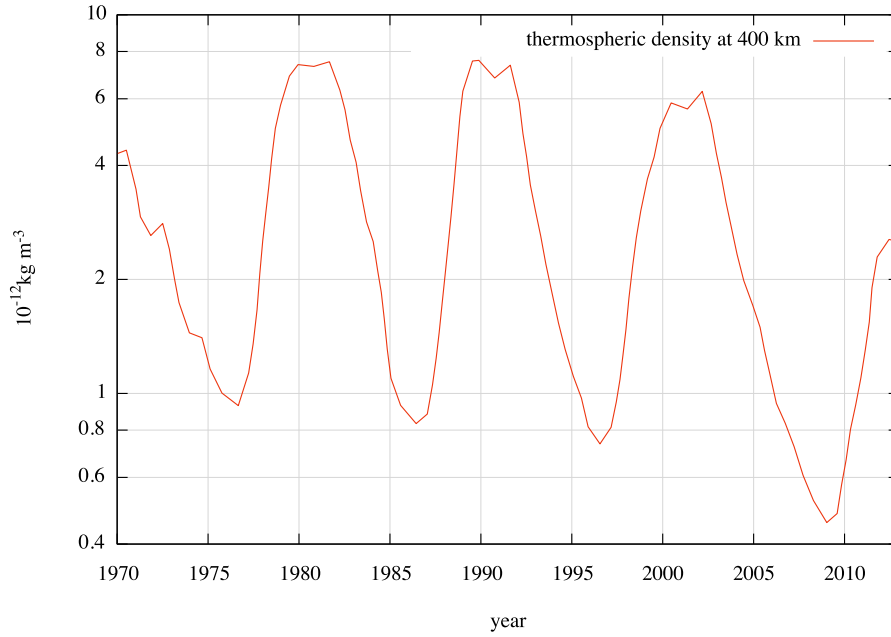


Figure 6.4 – Thermospheric density at 400 km altitude in logarithmic scale, obtained from orbit data for yearly running averages. Adapted from [Emmert, 2015].

The two modes, are written as \mathbf{X}^1 and \mathbf{X}^2 ,

$$\begin{aligned}\mathbf{X}^1 &= A^1 \otimes P^1 \\ \mathbf{X}^2 &= A^2 \otimes P^2\end{aligned}\tag{6.2}$$

where A^i and P^i are the vectors of the time series and spatial modes respectively, as in chapter 4. If we consider both time series to be constructed as an oscillation and a trend, we can separate each vector A^i as,

$$\begin{aligned}A^1 &= A_O^1 + A_T^1 \\ A^2 &= A_O^2 + A_T^2\end{aligned}\tag{6.3}$$

with A_O^i the oscillation part and A_T^i the corresponding trend. With this we can sum the two modes and re-arrange the different components.

$$\begin{aligned}
 \mathbf{X}^1 + \mathbf{X}^2 &= (A_O^1 + A_T^1) \otimes P^1 + (A_O^2 + A_T^2) \otimes P^2 \\
 &= A_O^1 \otimes P^1 + A_T^1 \otimes P^1 + A_O^2 \otimes P^2 + A_T^2 \otimes P^2 \\
 &= (A_O^1 \otimes P^1 + A_O^2 \otimes P^2) + (A_T^1 \otimes P^1 + A_T^2 \otimes P^2) \quad (6.4)
 \end{aligned}$$

With these equations, comprising the oscillation part of both mode 1 and mode 2 and the trend of the same modes we can analyse separately the two behaviours. Computing the two terms in brackets from equation 6.4, we get a series of snapshots for each of them during 1990-1998, corresponding to the descent of solar cycle 22 and beginning of cycle 23 (see figure 6.5). In the oscillation term during the entire time series we observe a change in the flux intensity distribution, with higher values moving from higher to lower L shells. The trend section on the other hand, shows only a peak of intensity, much like the one observed in 6.2(a). This peak does not show any movement towards higher or lower L shells over the duration of the investigated period. The only effect is the steady increase of the total intensity, not discernible in figure 6.5. These results seem to show that mode 1 and mode 2 are both contributing to the oscillation behaviour of the particle flux at a discernible level, while the trend in mode 1 is stronger and dominates its evolution.

The trend in mode 1 is a clear result from the decrease in thermospheric density reported in [Emmert, 2015]. The particle flux intensity increases as the density decreases. The trend in mode 2 is opposite, and even if not as strong as the trend in mode 1, it is a very important result, as we explain in the following. This trend is associated with a displacement in maximum flux intensity values between different L shells, as is evident by the associated spatial mode. As such, the trend is most likely due to a difference in the population depletion and or feeding, between the lower and higher L shells. On a decade time scale, due to the variation of the solar cycle, the thermospheric density changes have a clear effect in the population of the L shells. During solar maximum, the thermospheric density increases and the particle population goes toward higher L shells, corresponding to

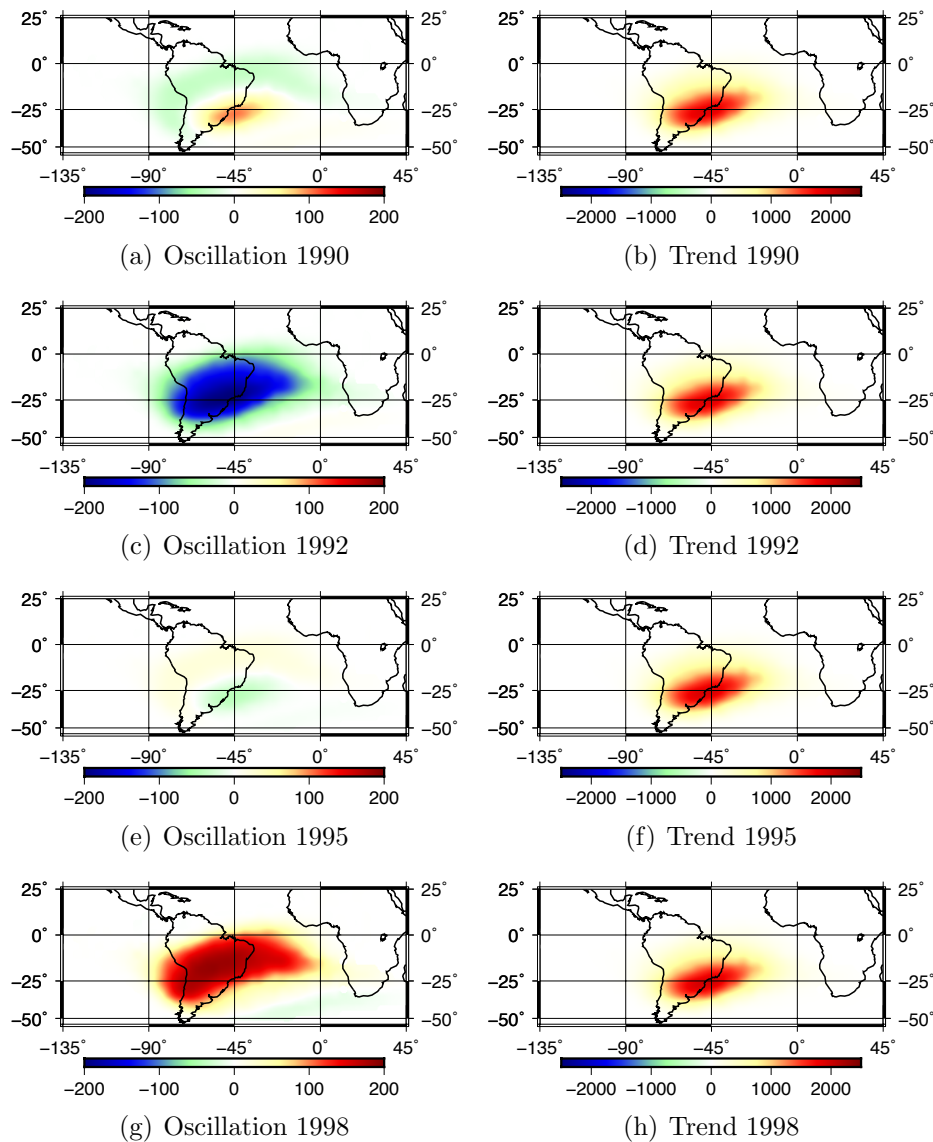


Figure 6.5 – Results of the calculations detailed in equation 6.4. Oscillation results presented on the left and trend results on the right. Four different instants are presented, beginning of 1990, 1992, 1995 and 1998, in order. This corresponds to solar maxima, transition to solar minima, solar minima and transition to solar maxima, respectively. The cycle between high and low values repeats until the end of the available interval. The x-axis is longitude and y-axis latitude.

a Southeast displacement. On the contrary, on larger time scales, the observed trend corresponds to a displacement in the same Southeast direction, but while the thermospheric density is decreasing. To produce the observed

effect, there must exist either a feeding mechanism that produces a larger increase in population in higher than in lower L shells or a depletion mechanism that produces a larger decrease in population in lower than in higher L-shells. We first have to consider the lifetime of protons in these regions. In [Jentsch and Wibberenz, 1980], it is clear that the particles trapped in lower L shells, even if they have high energy, have short lifetimes compared to the solar cycle 'quasi-period'. As explained there, although these particles respond to rapid density variations, they contribute less to long time scale effects and as such, the overall displacement related with the trend would shift towards the higher L shells. Also to note is the fact that due to the lower altitude of the low L shells, they are subject much more intensely to the effects of the increased thermospheric density (see [Jentsch and Wibberenz, 1980]). As such, during a large part of the solar cycle, when activity is strongest, the depletion process happens very efficiently, and the population at lower L shells drops and remains low. The population at these shells only increases at the solar minima, and as such, it reinforces the effect of the low L shell particles not participating in the long scale evolution of the anomaly.

6.2 Higher altitude data from Jason-2

In this section, I analyse in flight measurements of radiation on board the satellite Jason-2. [Boscher et al., 2011] indicate that the output of the ICARE NG detector of ONERA can be organised in 42 channels for protons covering the range 27.5 - 292 MeV. These authors have also shown that the measurements compare well, at solar minimum, with the model AP8 min for the distribution of protons as a function of the parameter L and of energy. Specifically, I discuss here two integral proton channels for energy levels 63 and 292 MeV, from June 2008 (launch of Jason-2) to January 2016. Jason-2 data over the period June 2008 to January 2016 have been considered and individual bins of 5 days calculated (superimposing the periods with the POES calculations), and then a regular grid obtained with a spacing of $2.5^\circ \times 2.5^\circ$. A grid between latitudes of -70° and 70° was created, as it was roughly the range of the satellite in the poles. Thereafter the particle flux was calcu-

lated in the L-shell reference frame much like in the POES data case (see chapter 5). With these grids, an indicator of the total flux was calculated by summing over all the grid points.

We don't expect the study of Jason-2 data to mimic the findings of POES. Observations retrieved from Jason-2 present two very significant differences that provide extra information regarding the particle flux evolution. First of all the orbit of the satellite is higher. It is 1300 km above the Earth's surface in comparison to the 800 km of the POES series. This gives us information on higher L shell populations. The other major difference is the energy distribution of data. In Jason-2 the instrument provides protons flux for well resolved energy ranges. Among the available integral channels two were selected to be analysed in this work, namely 63 and 292 MeV, the lowest and highest thresholds available from the detector. These values are both much higher than the lowest threshold for POES. Even though POES data also cover these energies, the results are dominated by the lower energy particles which are much more abundant and overshadow the higher energy particles signal. Another difference, this time limiting the utility of this dataset in the framework of this thesis, is that the time series available are shorter than a solar cycle, only 8 years. In figure 6.6 we can see the spatial modes from the PCA decomposition. On the left, the first and second mode for the lower energy of 63 MeV and on the right the corresponding modes for the higher energy of 292 MeV.

Looking first at mode 1 for both energies (figures 6.6(a) and 6.6(b)), which is the mode that represents the variation of intensity of the anomaly, we see the same structure with a shift in position. The center of intensity of the anomaly is located further south for the low than for the high energies as expected (see figure 14 of [Boscher et al., 2011] and figure 3 of [Boscher et al., 2014]). Comparing to the results from POES, we can see that the low energy result is located closer to the results from POES, which agrees with the fact that the POES results are dominated by lower energy counts. From this we can confirm that the particles are arranged in the L-shells by energy. High energy particles are trapped at lower L values, and low energy particles at higher L values, as we can see in the spatial modes.

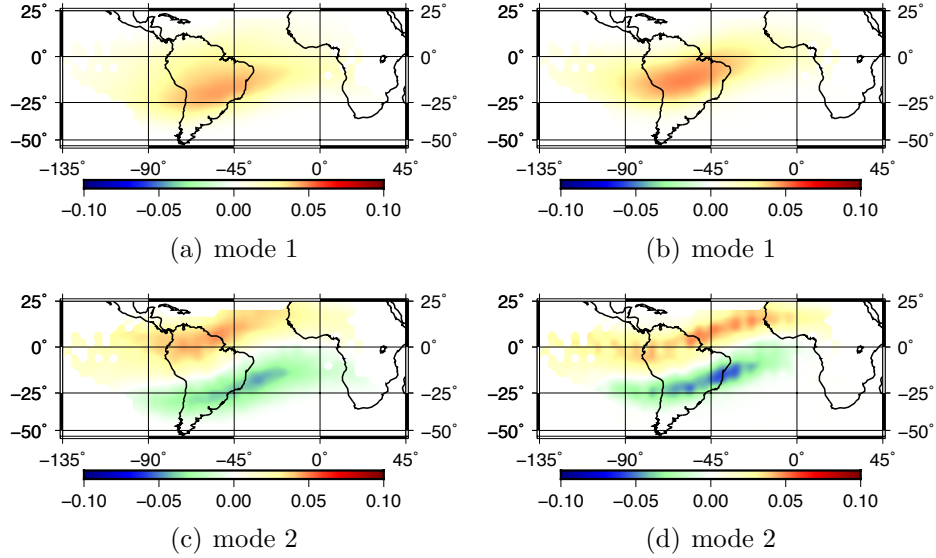


Figure 6.6 – Jason-2 63 MeV spatial mode (left), Jason-2 292 MeV spatial mode (right). The x-axis is longitude and y-axis latitude.

This behaviour was already known [Selesnick et al., 2014], but the analysis based on PCA spatial modes provides extra information [Jones et al., 2017]. The spatial structures, from Jason-2, are broader than the ones observed in POES. This is likely to be both due to the reduced particle counts, as these are higher energies, and also the higher altitude of the satellite. At higher altitudes, the L shells are more spread out, covering a larger area than at lower altitudes.

The second spatial modes (figures 6.6(c) and 6.6(d)) are again very similar, this time showing a very clear dipolar behaviour. The shift in the position is again present as would be expected. The striking fact is the clear separation between the two regions of different sign. In POES data, we observed that the second mode was also of a dipolar nature but lacked the mirrored aspect we can see here. This effect is due to the different energy ranges from the different satellites. Here we have much higher energy ranges than POES, and consequently, less total flux. The majority of particles are removed from these detections, this means that we will see close to the same behaviour from all the particle population, moving from higher to lower L shells (and vice-versa). Previously, we had a larger population of particles and of many different ener-

gies, so what we saw was the added effect of this displacement. Each particle with a different energy value was affected differently by the same conditions, so the movement from higher to lower L shells (and vice-versa) showed a large spread. Differences seen in mode 2 for lower and higher energy particles are consistent with the strongly decaying energy spectrum as observed for higher L shells (e.g. [Selesnick et al., 2014, Jentsch and Wibberenz, 1980]). We see how these shells tend to become depleted of high energy particles in figure 6.6(c) and 6.6(d). Focusing our attention on the time series associated with each spatial mode, some interesting conclusions can also be drawn. In figure 6.7 we can see the time series associated with the modes in figure 6.6 and the POES results for comparison. Looking to the different modes of the 63 MeV results, namely the first mode time series (figure 6.7(a)), we see that they somewhat agree, having the same general evolution.

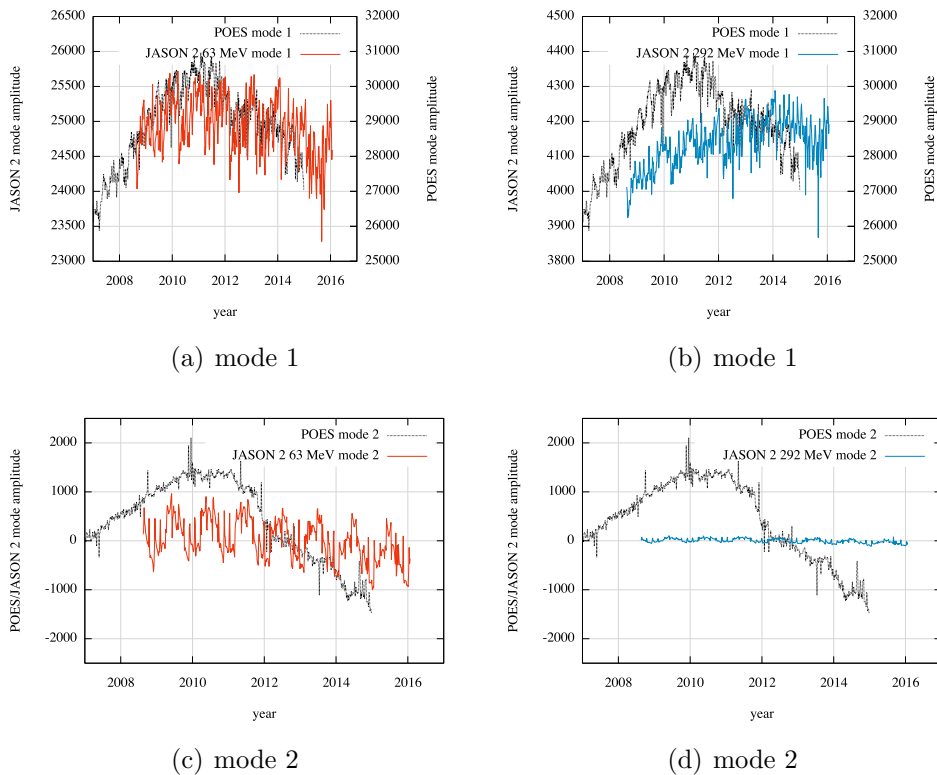


Figure 6.7 – Time series of the associated spatial modes in figure 6.6. Jason-2 63 MeV time series (left), Jason-2 292 MeV time series (right). Note that for both the first modes, the amplitude scale is smaller than POES (black), 50 % and 10% for mode 1 and 2 respectively.

When looking at the 292 MeV results (figure 6.7(b)) we can no longer make this statement. One possibility is that the response we see at higher energies has a phase lag associated with it (see [Jentsch and Wibberenz, 1980]). In this case, if we consider a lag of 3 years for the higher energy, the series have a similar behaviour. Due to the high energy and altitude of the protons in this case, it can also be that the particles are not so much influenced by the solar cycle as lower energy ones. If we now look at the second mode time series (figures 6.7(c) and 6.7(d)), the solar cycle effect does not seem to be present. A trend seems to be present, and it coincides with the trend observed at all the POES results, but the time series is not long enough to make that assessment. This is exactly the information the extended series from POES provided and made clear from the initial dataset. To determine this effect a longer dataset from Jason would also be needed.

The signals in figure 6.7 appear to have three distinct periods. An annual period, stronger on mode 2, a 4-month period also stronger on mode 2, and a shorter period, stronger on mode 1, of 59.1-days, as can be seen in figure 6.8. The shortest period results from the characteristics of the orbit of Jason-2. The time the satellite requires to cover all local times as it orbits is 58.7 days [Zawadzki et al., 2016]. We observe the atmospheric heating and consequent variation in particle flux density associated with the local day-night cycle.

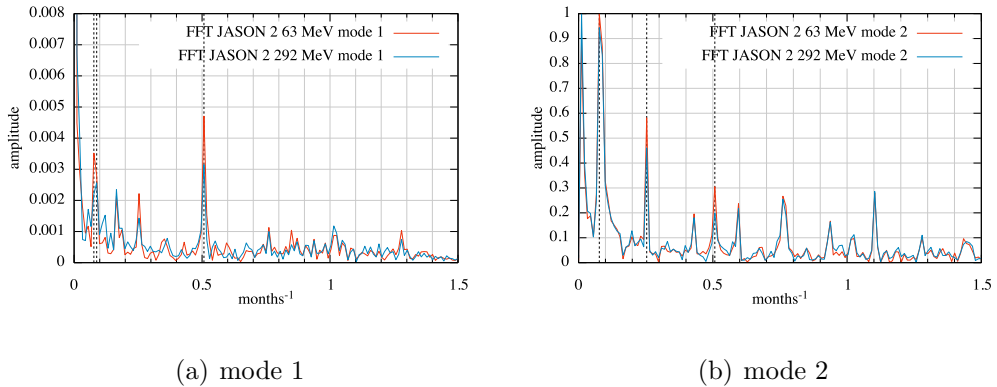


Figure 6.8 – Periods of the signals in figures 6.7. A period of 59.1 days is observed at both modes. For mode 1, a period of 11.33 to 12.95 months is observed, while for mode 2 the period is centered at 12.95 months. A period at 3.94 months for mode 2. All periods are marked with a black vertical line.

The annual signal, present in both modes from Jason-2, although more clearly in the second mode, is a known effect. This is a signal we do not see in the POES data which are sensitive to protons with lower energy, but is very distinct here. The population of particles and their movement is affected by the Sun as is the atmosphere density, and as such, the annual signal is expected [Emmert, 2015, Casadio and Arino, 2011]. In [Schaefer et al., 2016] the variation of intensity of the flux of protons with energy > 45 MeV in the SAA is shown, with a minimum in July. This would agree with our results for mode 1, shown in figure 6.9. There is also an annual signal in mode 2, corresponding in this case, when looking at the associated spatial modes (figures 6.6(c) and 6.6(d)), to a displacement North in the middle of the year. This corresponds to a movement towards lower L shells, when the total intensity is decreasing. This is the same mechanism responsible for the 11-year oscillation, as the thermospheric density decreases in June-July.

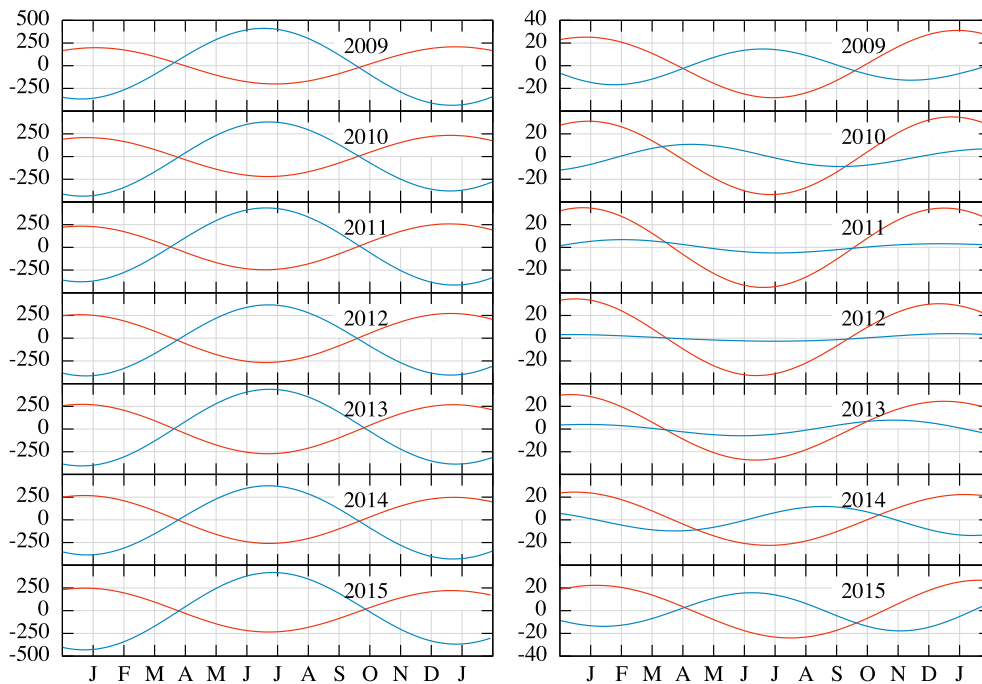


Figure 6.9 – Annual signal from figures 6.7 shown for each year of the series. 63 MeV results shown on the left for mode 1 (red) and mode 2 (blue). 292 MeV results shown on the right for mode 1 (red) and mode 2 (blue).

Comparing with the annual variations in density (see eg.: [Guo et al., 2008] for the density at 400 km altitude) we remark that the annual variation in the flux of high energy protons cannot be directly attributed to increased capture of protons when the thermosphere is denser. This remark agrees with the

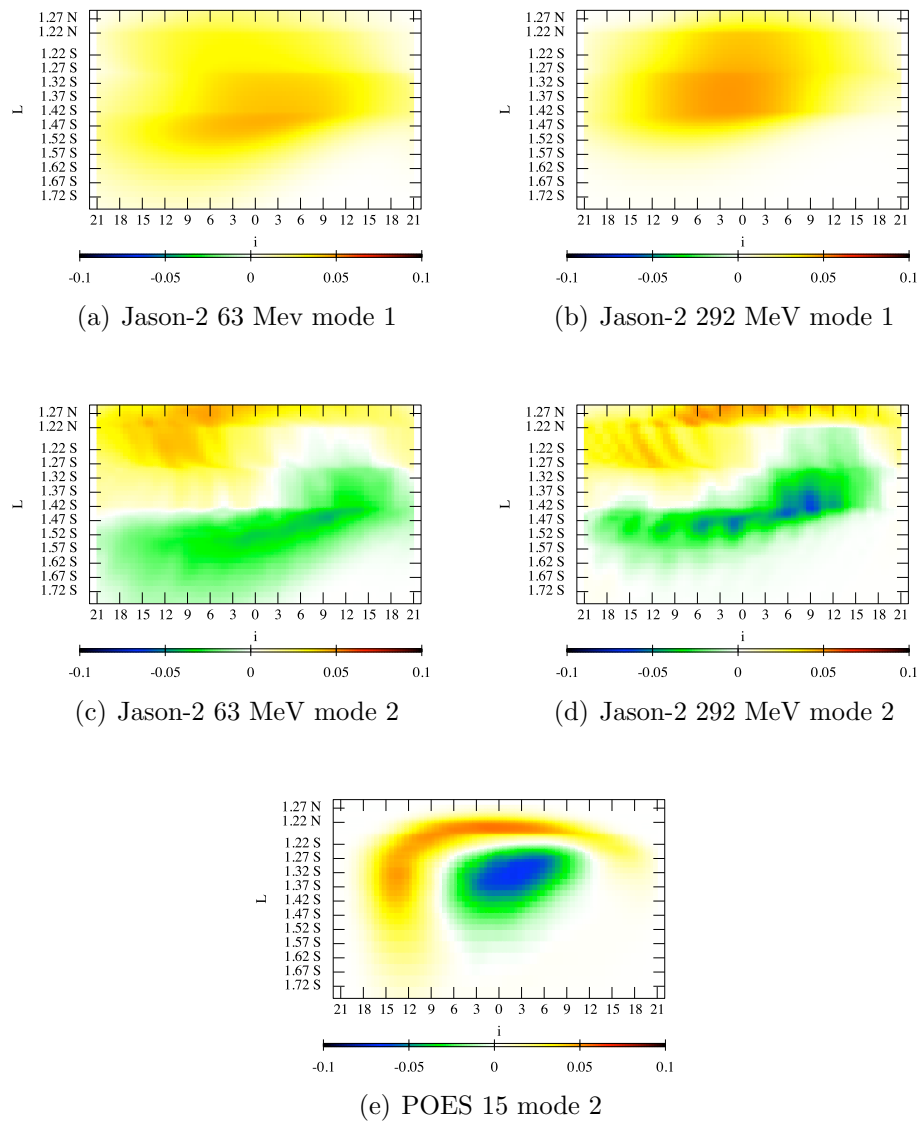


Figure 6.10 – Jason-2 63 MeV spatial mode (left), Jason-2 292 MeV spatial mode (right), represented in the L - B_{min} grid. In this representation equation 5.2 is used, with i values ranging between 0-21 and the B_{step} equals to 10. In the bottom, POES 15 mode 2 is plotted in the same grid (see figure 5.9)

observation that the annual cycle is not detectable in lower energy protons series (POES). [Schaefer et al., 2016] tentatively attribute the annual signal to an annual variation in cosmic ray radiation. [Antonucci and Marocchi, 1978] have found indeed that there is an annual component in the cosmic ray intensity. Its phase depends on the 22-year cycle.

Instead of plotting the spatial modes in the geographical space, we can plot the modes in the L - B_{min} space, as was done in chapter 5. In figure 6.10 we can see the clear separation between L shells, and how the distribution of particles in the different L shells evolves.

6.3 Discussion

The concatenation of the series from 3 successive satellite missions clearly has advantages in identifying long scale behaviours. A trend that in chapter 5 was speculated upon, now becomes clear. Of course this procedure has drawbacks, as the joining of the series may introduce some errors. Nonetheless, as the possible problems were identified and directly addressed through a robustness test, we believe we can trust our results. Here, the long series allowed us to observe a trend associated with a gradual increase in particle flux, and a different trend associated with the particle population on the different L shells. The first trend can be associated with that observed in the thermospheric density over the same period. The source for this trend in density seems to be the build up of CO_2 in the atmosphere [Emmert, 2015], which leads to a cooling of the high altitude atmosphere. The second trend is more interesting, as it goes against the previous considerations made about the displacement in the L shells during thermospheric density variations and has not been reported before. To explain it, the mechanisms proposed to explain the behaviour on decade and shorter time scales cannot be used for the long scale trend. The short lifetime of the particles in the lower L shells [Jentsch and Wibberenz, 1980], and the high levels of depletion in this region during high solar activity [Jentsch and Wibberenz, 1980] imply that this region is less responsive than high L shells to the trend in the thermosphere density. The higher L shells are less affected by these effects and so the dis-

placement on the long term is towards these shells.

Another addition to the findings in chapter 5 is provided by Jason-2 data. Although the data span a few years (shorter period), it is the separation between energy range detections and the increased altitude that provide new results. The observed spatial structures are consistent with the results obtained from POES. Furthermore, we get the chance to observe the effects of varying altitude and energy on the particle flux anomaly, seen as a diffuse and less intense anomaly for the altitude increase and a change in L shell population associated with the different energies. The shifting of populated L shells along time, due to various effects becomes very clear when we look at a tighter energy range. This shifting is visible for low and high energy particles as evident by figures 6.6(a) and 6.6(b). In Jason-2, the strongest observed signal in the first mode, which governs intensity, is an annual signal. This cannot be directly interpreted as the result of density variations. The time series of second modes for both energies, 63 MeV and 292 MeV, do not show a significant trend and at this short time period we can only discern the short 59.1-day period [Zawadzki et al., 2016], the annual signal [Emmert, 2015, Casadio and Arino, 2011] and a 4-month period. Due to the fact that the altitude of Jason-2 is higher, namely 1300 km, the effects of the thermospheric density variation are lessened. The particles have less a chance to interact with the neutral atmosphere in these shells than L shells that are completely in the thermosphere.

Chapter 7

Application of PCA to the recent geomagnetic field

A large part of the evolution of the SAA is due to the geomagnetic field. Here we will apply the PCA method to the geomagnetic field itself, but this time taking full advantage of the vectorial capabilities of the method. This means we will analyse the three components of the field simultaneously resulting in a better description of the field in terms of PCA modes. A localised grid as that used with particle flux data is not ideal for this situation. A global grid that allows to retrieve all the aspects of the geomagnetic field is the best approach instead. With a global coverage, the PCA method provides the possibility to identify modes most possibly due to either internal sources to the Earth or external sources.

7.1 Virtual observatories (VO)

The Virtual Observatory approach [Mandea and Olsen, 2006], consists in using measurements from satellite instruments over a certain period of time which are interpolated to simulate fixed observatory measurements at the satellite's altitude. It provides us with the ability to have continuous magnetic field series, which allows to separate time and space variations, while overcoming a big weakness of observatory data, which is the uneven distri-

bution of the observatories.

The Virtual Observatory grid distribution used in this work was provided by Chris Finlay and Magnus Hammer. It consists of 500 grid points ('observatories') at 500 km altitude. The Recursive Zonal Equal Area Sphere Partitioning Toolbox [Leopardi, 2006] was used to create this distribution in order to partition the surface of a sphere into nearly equal area regions. This equal distribution of grid points lets us consider the entire region without having to add any weighting factors to different latitude regions, as is customary in a geographic grid spacing approach. To calculate the values of the field at the VOs location, all data in a cylinder of a certain radius around each point were collected. After properly selecting the data, a cubic potential was fitted to the data in each of these cylinders and a prediction was calculated for the chosen point by fitting the data to $\mathbf{B} = -\nabla V$.

The data were selected in order to reduce noise and aliasing from high frequency currents in the magnetosphere and the ionosphere and charges circulating near and across the satellites orbit. A 15 second data sampling rate was used as the base set. Gross outliers deviating more than 500 nT from the CHAOS-6 model were removed and only dark time (10 degrees below horizon) and geomagnetically quiet conditions ($Kp < 3^0$, $dRC/dt < 3$ nT/h, $E_m < 0.8$ mV/m, $B_z > 0$ nT and $abs(B_y) < 10$ nT) were taken into account [Finlay et al., 2016]. The Kp index [Richmond, 1995] is a measure of the disturbances in Earth's magnetic field, namely the horizontal component (see chapter 1). The RC index [Olsen et al., 2014] is defined by an hour-by-hour spherical harmonic analysis of hourly means from 21 worldwide distributed observatories. It describes the magnetospheric ring current strength even during geomagnetic quiet conditions. This improves on the more widely used Dst index [Sugiura, 1964] which has baseline instabilities that affect geomagnetic field modelling. E_m is the merging electric field at the magnetopause, described initially by [Kan and Lee, 1979]. The revised version of this index is used here [Newell et al., 2007]. B_z and B_y are components of the IMF described in chapter 1.

The solar quiet (Sq) ionospheric field in quasi-dipole coordinates is subtracted from the data. Magnetic fields from the magnetosphere as modelled

in CHAOS-6, the ionosphere as modelled in CM4 [Sabaka et al., 2004], and the crust (CHAOS-6) are also subtracted from the time series. Making use of the Swarm constellation, along-track and cross-track differences and sums are used.

7.2 Data selection for PCA

Virtual Observatories based on data from CHAMP satellite and Swarm's constellation of three satellites were used to perform a PCA analysis of the magnetic field. The period under study goes from February 2004 to January 2010 for CHAMP and from April 2014 to April 2017 for Swarm. For both datasets, vector magnetic field values with monthly resolution were used. Virtual Observatories are appropriate for PCA as they provide data for a fixed set of spatial coordinates, which is a requirement of PCA decomposition. The distribution of the grid points can be seen in figure 7.1. In 3D, this representation covers the globe uniformly, as previously mentioned, so not to overweight any given region and as such, no weighting factor is needed. Grid points at latitudes 90° and -90° , were removed and the maximum count of the grid points is: $N_P = 498$.

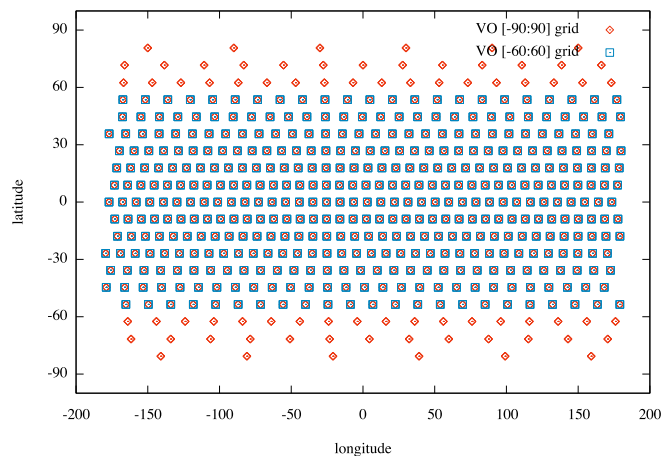


Figure 7.1 – a) Distribution of the virtual observatories over the globe. The altitude of the VOs is 300km for CHAMP and 500 km for Swarm. Red dots represent the global coverage (total of 498), while blue squares represent the VOs in the sub-auroral region (total of 424).

For both CHAMP and Swarm, two different sets were constructed, one using all the 498 VOs (global grid), and another only 424 VOs between -60° and 60° latitude (sub-auroral grid). Only the spatial functions for the global grid are shown for most modes, as the sub-auroral PCA spatial modes were frequently similar in the selected region. The spatial modes are shown in a Hammer projection, centered on the equator (for more detail see appendix B). More important were the differences between global and sub-auroral time series of each mode and, as a result, the two obtained time series are shown for every mode. Plots of the time series must be complemented with information on the multiplying values that introduce different scalings for the three vector components of the same mode. These factors, introduced in Chapter 5, are essential to completely define the spatial geometry of the field modes, a feature which is specific of PCA applied on vector data. They are given in tables 7.1 and 7.2, to be used as shown in eq. 7.1 in order to retrieve the real amplitude series, A_i^{lk} , for each of the three separate components (B_r , B_θ and B_ϕ):

$$A_i^{lk} = A_i^k \times N_{F_i}^k \quad (7.1)$$

where A_i^{lk} is the unnormalised time series, A_i^k is the normalised series and $N_{F_i}^k$ is the normalising factor, different for each component, and shown in tables 7.1 and 7.2 for the CHAMP and Swarm results respectively. This step in the calculation of PCA modes is most important to assign meaningful quantitative values to our estimates.

7.3 Results

7.3.1 CHAMP

The CHAMP dataset consists of roughly 6 years of monthly values at each VO, close to twice as much as Swarm. Although Swarm data is more precise, the longer time series from CHAMP allows to expect a better resolution of modes that have annual to decadal characteristic times. Figure 7.2 shows the fraction of variability for each mode from the PCA decomposition of

CHAMP data. Using Lawley’s formula for the typical error in eigenvalues (e.g. [Storch and Zwiers, 2003]), we can see that the first three modes are well separated, though higher modes are still somewhat inter-related. There is no clear improvement for high-order mode separation when using the global or sub-auroral dataset.

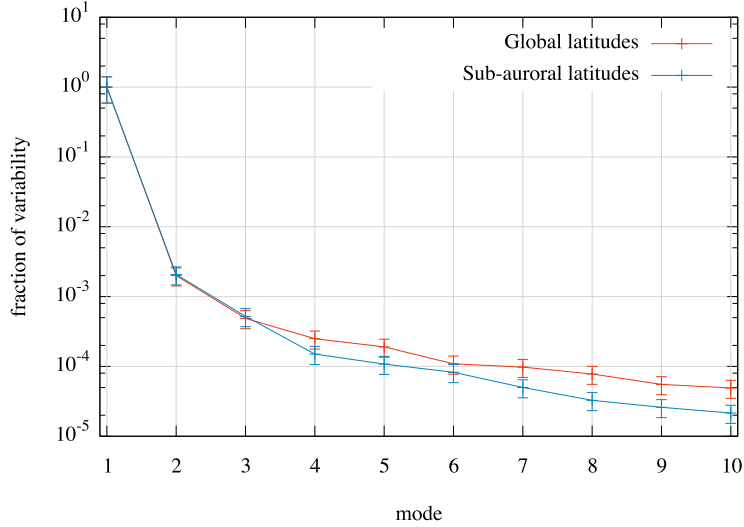


Figure 7.2 – Fraction of variability of standard PCA modes from CHAMP and associated standard deviation. The two plots are for PCA applied to the global spherical grid (red) or eliminating points at super-auroral latitudes (blue).

The PCA is applied on the 6 years of data. There are two options when applying PCA, we can either keep or remove the average of each monthly grid before calculating the SVD decomposition. In this case the average was removed because it introduced a completely different spatial mode, i.e., the vector of the average field is not an eigenvector of the covariance matrix. For more information on this choice I refer to chapter 4.

In figure 7.3, the spatial features of the first five modes of the PCA decomposition are shown. The vector PCA decomposition implies that each mode is characterised by three different plots, one for each B_r , B_θ and B_ϕ components. Note that all charts in figure 7.3 are normalised to 1 (see Chapter 4), so that we can not directly infer the relative importance of any given component. The multiplying factors in table 7.1 must be treated as an independent output of the vector PCA method, crucial to fully characterise

each mode.

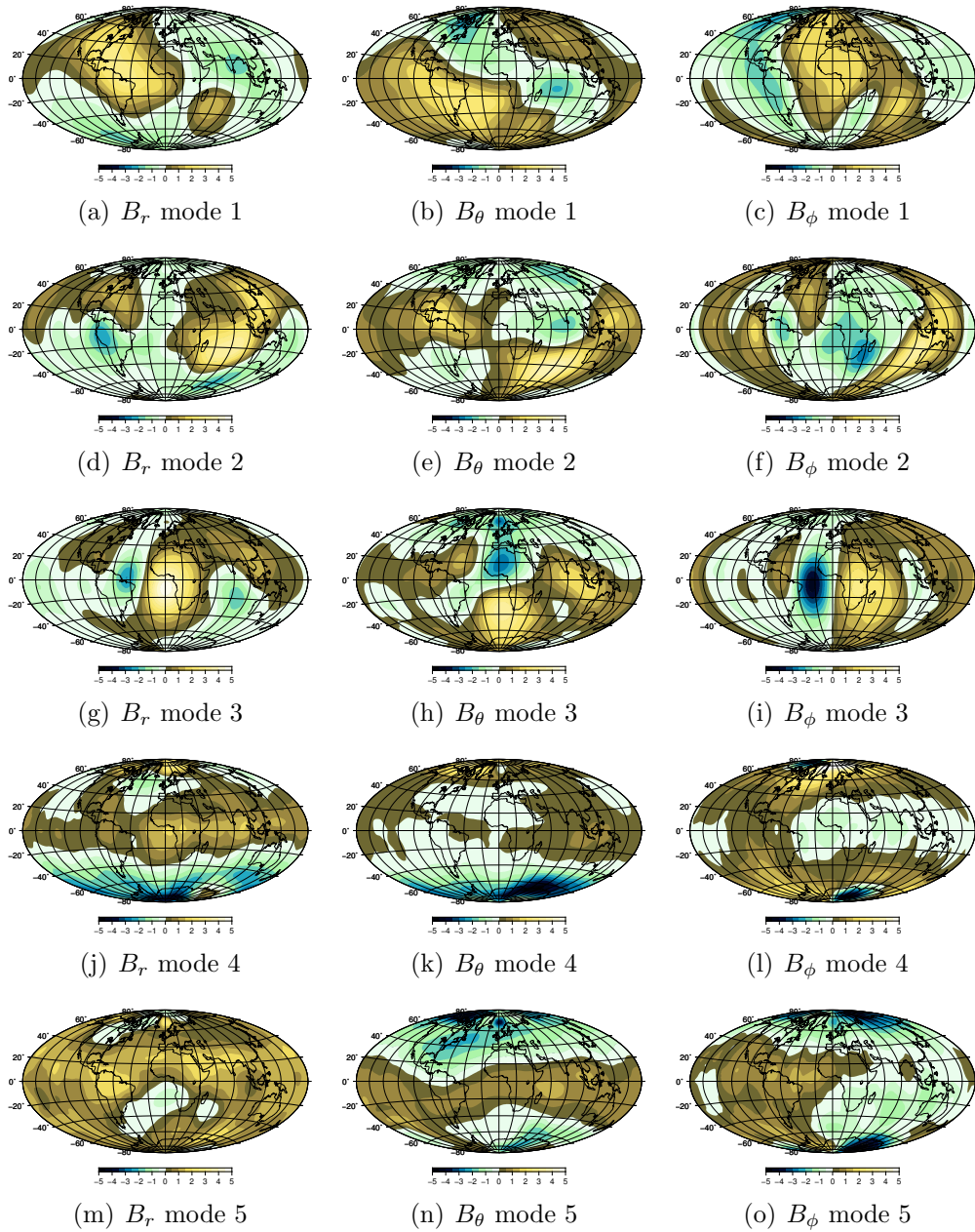


Figure 7.3 – Representation of the spatial charts (B_r , B_θ and B_ϕ) of the first five modes of the PCA decomposition, for the global grid, using data from CHAMP. The color scale ranges from -5 to 5 (normalised values).

The time series corresponding to the first five modes from CHAMP are represented in figure 7.4, with zoom in of the last two plots. This was done as these modes show a more complex time variation, and can be harder to read. The first three modes seem to represent the first order terms of a Taylor-like expansion in time of the whole dataset, i.e., a linear term, a quadratic, and a cubic terms. As will be discussed later, there seems to be some relevant geophysical information in at least some of those modes, showing that this decomposition is not merely a mathematical representation.

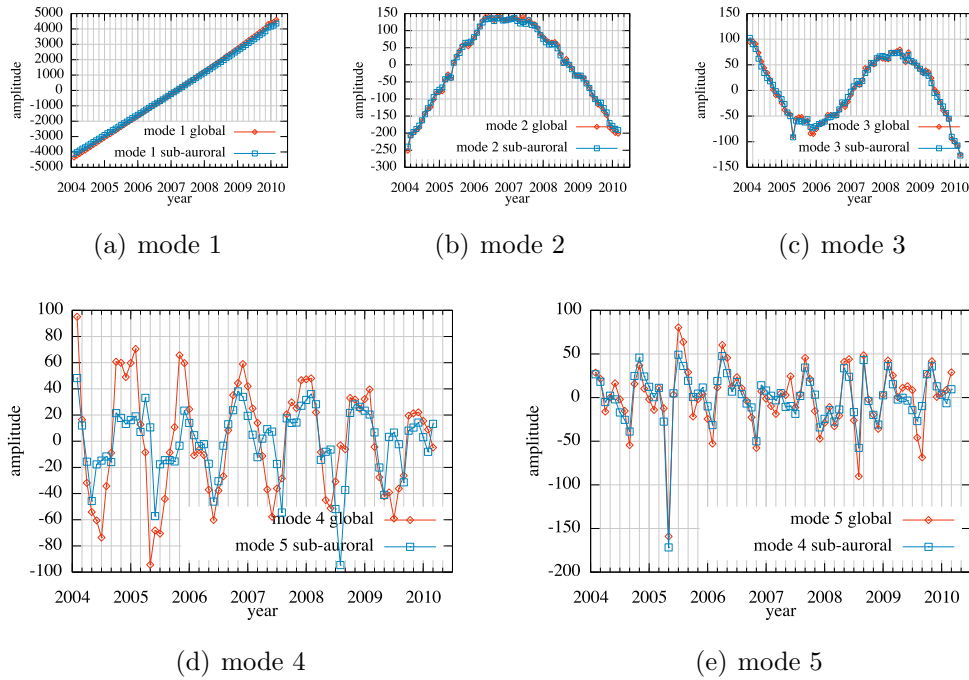


Figure 7.4 – A_i^k time series corresponding to the spatial modes in figure 7.3, for the global grid (red) and sub-auroral grid (blue).

Different plots in Figure 7.4 use different scales. To obtain the unnormalised amplitude of each time series, the normalising factors from table 7.1 have to be used.

Mode, k	Component, i	Norm factor, N_F	
		global	sub-auroral
1	B_r	0.0351718	0.0383478
	B_θ	0.0201432	0.0216600
	B_ϕ	0.0191110	0.0204642
2	B_r	0.0338641	0.0369254
	B_θ	0.0228691	0.0241553
	B_ϕ	0.0183917	0.0202861
3	B_r	0.0328372	0.0365102
	B_θ	0.0183839	0.0185014
	B_ϕ	0.0243265	0.0261379
4	B_r	0.0201739	0.0304864
	B_θ	0.0333930	0.0349949
	B_ϕ	0.0220443	0.0142978
5	B_r	0.0222413	0.0220578
	B_θ	0.0345780	0.0317929
	B_ϕ	0.0178245	0.0293454

Table 7.1 – Normalising factors of PC time series for all five modes of CHAMP PCA decomposition (See equation 7.1).

7.3.2 Swarm

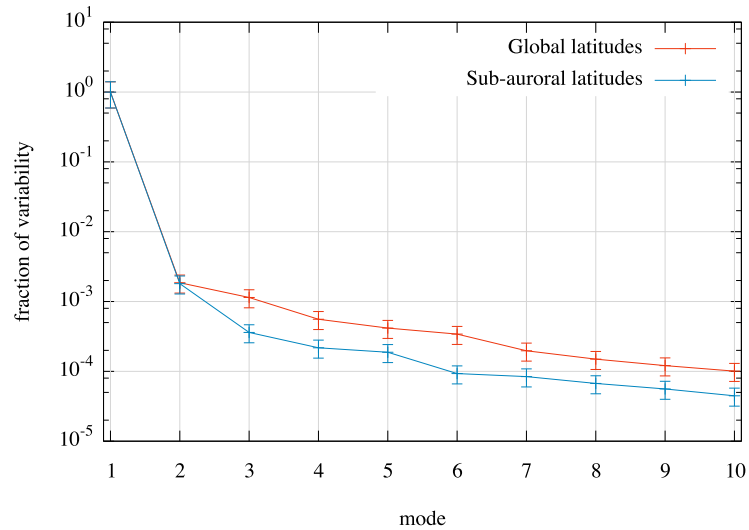


Figure 7.5 – Fraction of variability of standard PCA modes from Swarm and associated standard deviation. The two plots are for PCA applied to the global spherical grid (red) or eliminating points at super-auroral latitudes (blue).

Figure 7.5 represents the fraction of variability from Swarm modes. Comparing with Figure 7.2 for CHAMP, a clear difference appears. We no longer have three main modes, well separated and with identical fraction of variability considering both global and sub-auroral regions. We now have only two modes that are identical using the two grids. Higher order modes differ significantly, depending on the used grid.

Much like the results from CHAMP, to obtain the unnormalised amplitude of each time series from Swarm, the normalising factors can be found in table 7.2.

Mode, k	Component, i	Norm factor, N_F	
		global	sub-auroral
1	B_r	0.0351381	0.0384481
	B_θ	0.0193757	0.0207645
	B_ϕ	0.0198470	0.0211913
2	B_r	0.0364613	0.0323227
	B_θ	0.0169137	0.0284618
	B_ϕ	0.0197106	0.0224424
3	B_r	0.0217346	0.0310579
	B_θ	0.0348364	0.0192739
	B_ϕ	0.0178337	0.0319752
4	B_r	0.0230277	0.0284364
	B_θ	0.0296580	0.0266224
	B_ϕ	0.0243749	0.0290019

Table 7.2 – Normalising factors of PC time series for all four modes of Swarm PCA decomposition.

Figure 7.6 shows the spatial structure of the first four modes of the PCA decomposition from Swarm. The layout is identical to figure 7.3. As explained above, the Swarm dataset produces one fewer main mode. When we compare Swarm and CHAMP modes, both spatially (figures 7.3 and 7.6) and temporally (figures 7.4 and 7.7), we realize that the missing mode is mode 3 from CHAMP, the one with an associated cubic temporal variation.

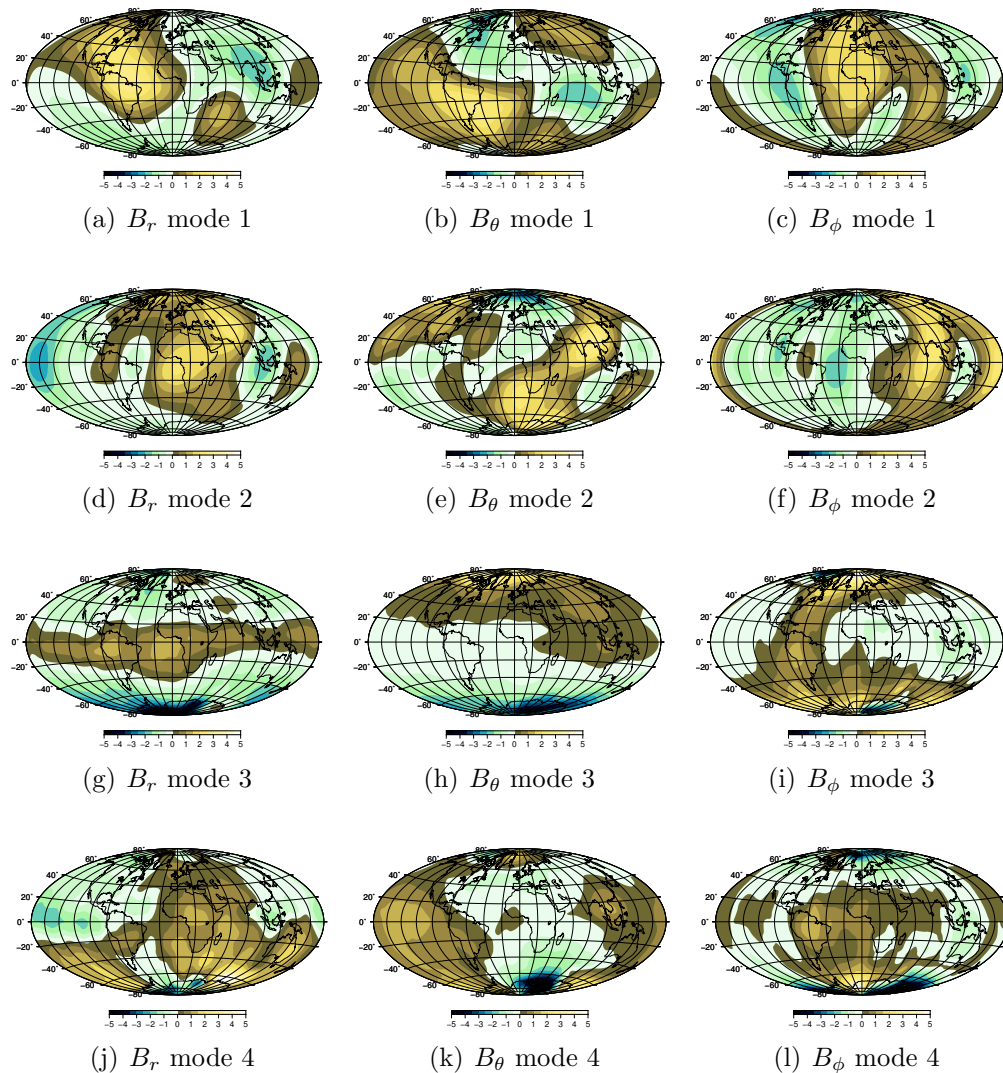


Figure 7.6 – Representation of the spatial charts (B_r , B_θ and B_ϕ) of the first four modes of the PCA decomposition, for the global grid, using data from Swarm. The color scale ranges from -5 to 5 (normalised values).

Figure 7.7 shows the time series corresponding to the first four modes from Swarm. The first two modes have again a linear and a parabolic time evolution as seen in Figure 7.4 for CHAMP. They represent the two lower order terms in a Taylor-like expansion in time. We no longer see the cubic polynomial represented, but the higher frequency modes still occur.

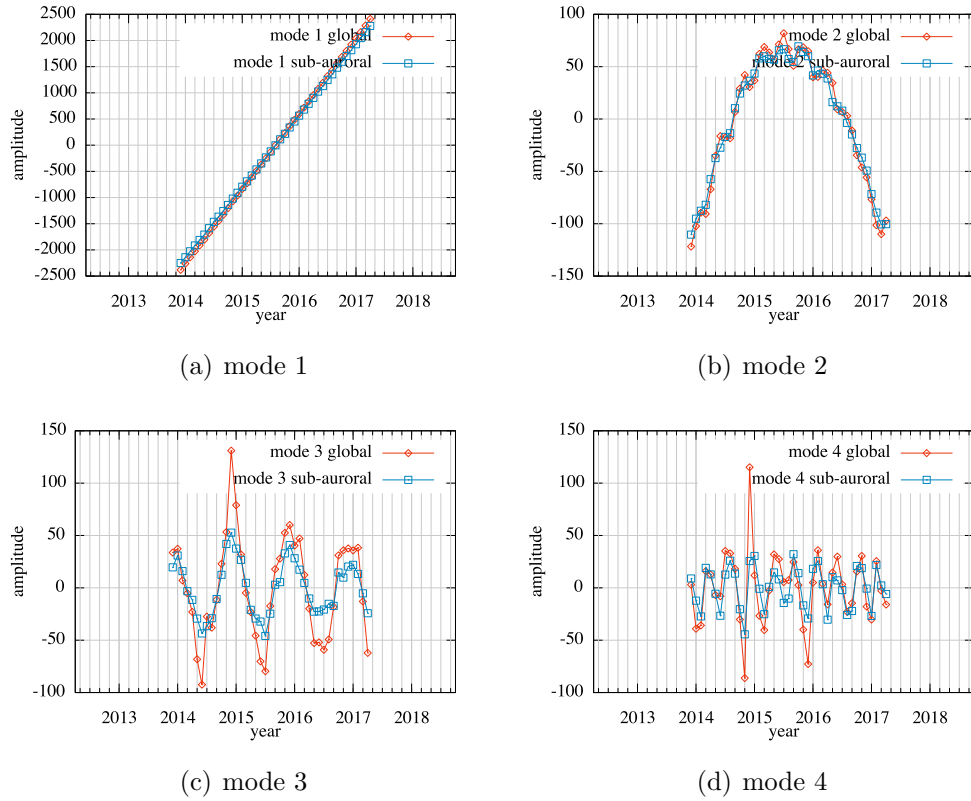


Figure 7.7 – Time series corresponding to the spatial modes in figure 7.6, for global grid (red) and sub-auroral grid (blue).

7.3.3 Internal and External modes

The standard decomposition of the Earth’s irrotational field into spherical harmonic functions, allows to parameterise differently the internal and external contributions (see Chapter 2). Note that with respect to VOs, internal components have a source below the satellite orbit, and external components will cover the remaining outer sources. The PCA method is non-parametric and decomposes the entire magnetic field into separate modes only on the basis of existing correlations in the data. In order to separate sources into internal and external, standard spherical harmonic analysis, was applied to the individual modes produced by the PCA method. We started by considering an internal field model. If such a model fits closely a given mode, this mode

will be identified as internal. On the contrary, high misfits are interpreted as meaning that the mode is due, at least partly, to external sources. The misfit is obtained from the residuals of the model compared to the mode as in equation 7.2.

$$Misfit = \sqrt{\frac{(P^M - P^k)^T \cdot (P^M - P^k)}{N}} \quad (7.2)$$

where P^M is the fitted model, P^k is the vector of spatial mode k and N is the number of grid points.

In table 7.3, we can see the results of this calculation. The first three modes from CHAMP have normalised misfits from this calculation below 0.006, while the following two have misfits close to 0.02. For the case of Swarm, we only get the first two modes with misfit at most 0.005, and the following two are above 0.02. A similar test can be done, this time considering a harmonic field with sources external to the surface described by the VOs. These results are also shown in table 7.3. From these results we see that, with respect to an external harmonic field model, the best fitting mode is mode 4 from CHAMP and mode 3 from Swarm. Modes that had low misfits with respect to an internal harmonic model, now show high misfits, as expected.

Satellite		Misfit ($\times 10^{-2}$)				
		mode 1	mode 2	mode 3	mode 4	mode 5
CHAMP	internal	0.01404	0.27137	0.53992	2.07323	1.96048
	external	2.58671	2.57949	2.55958	1.88835	2.22695
Swarm	internal	0.01790	0.47828	2.21487	2.38930	—
	external	2.58411	2.55442	1.57966	1.97018	—

Table 7.3 – Misfit values from internal and external SH fit of the PCA modes, for both CHAMP and Swarm.

Modes 4 and 5 from CHAMP and 3 and 4 from Swarm have annual and semi-annual signals respectively. The known periods associated with internal field sources have longer periods, as so, it follows that these modes most likely have origin above the surface of the Earth. There are several currents

in the ionosphere and magnetosphere, which generate induced fields strong enough to be detectable by satellites. Taking into account the altitude of the satellites, these currents could be below, above or intercepting the trajectory of the satellites.

The results from these tests, together with a close look at the spatial features and time series of the modes, allow us to separate the first three modes from CHAMP and the first two from Swarm into modes with internal sources, and the remaining ones as having at least some external part. Mode 4 from CHAMP and mode 3 from Swarm still show a high misfit when considering an external harmonic field, even though it is lower. This can be due to the fact that the field represented by this mode is not a harmonic field, at least not entirely. An electric current system at the altitude of the VOs would not be represented by a harmonic field. Figure 7.8 shows the graphical representation of the values in table 7.3. The separation between internal and external modes is clearly seen on the left, with a clear jump in the misfit values from internal to external modes. As to the plot on the right, it shows an apparent 'anomaly' in mode 3/4 from CHAMP/Swarm, indicative of a possible contribution of an external harmonic field.

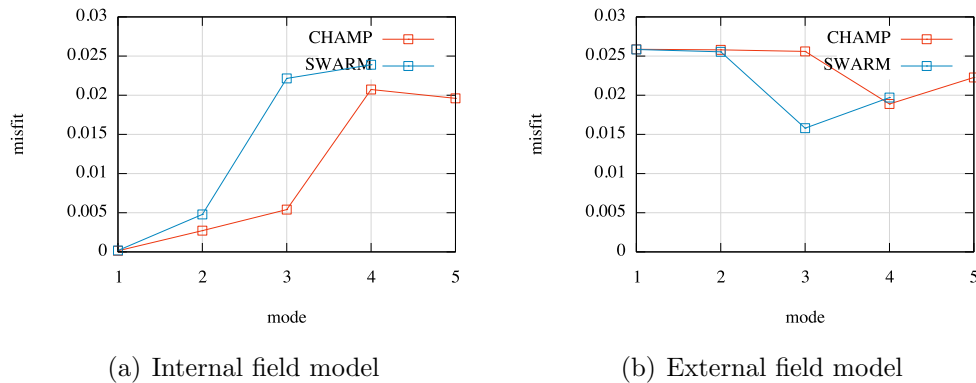


Figure 7.8 – Misfit values to a harmonic field fit, both internal (left) and external (right)

Having fitted the modes to two different models, one internal and one external, we can calculate the spectra (see equation 2.10 in chapter 2) of the harmonic degrees, in order to see the dependance of each mode on the SH degree. Figure 7.9 shows both the spectra for the internal modes (figure

7.11(a)) and the mixed modes (figure 7.11(b)).

The ability of the PCA method to separate internal modes is an important result. In PCA, no a-priori conditions or restrictions are imposed, no parameterization is being used and the method is only based on correlations between data values. Nonetheless it may be able to separate the dataset into modes according to their sources.

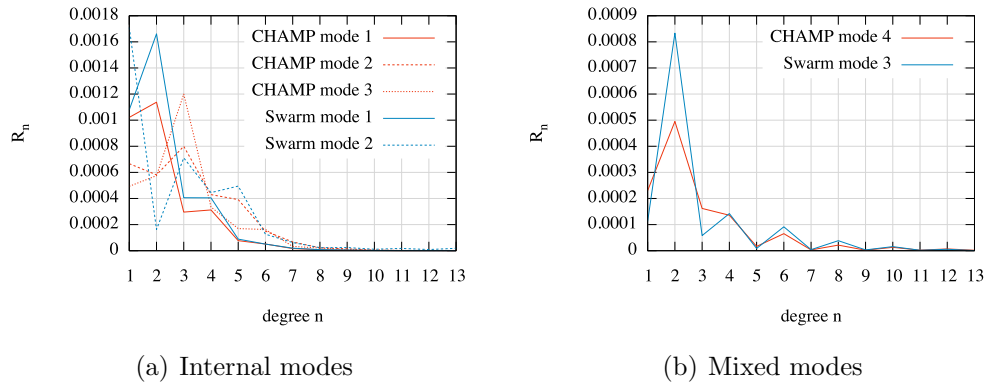


Figure 7.9 – Spectra of the harmonic field models, internal (left) and external (right), fitted to different PCA modes.

7.4 Discussion

The PCA decomposition of the dataset matrix is always possible, in general, as a mathematical operation. This decomposition is particularly useful in cases where it allows to distinguish different physical source contributions. The fit of internal and external harmonic models to PCA modes guided us in a plausible separation between internal and mixed modes.

From each satellite dataset, we identified two to three modes of internal origin. The time series of these modes represent increasing degrees of a Taylor expansion in time. The first mode corresponds to a linear term, the second mode to a quadratic and the third mode to a cubic term. We can expect that if we had access to longer series, we would retrieve from the PCA decomposition extra terms for this series. In fact, the CHAMP data series produces an extra internal mode as can be seen in figure 7.3. Swarm data

do not produce the cubic term in the internal decomposition of the field, as the time series are too short to properly represent it. Tests were done by reducing the period of CHAMP data that was analysed by PCA and the third mode no longer appeared. Removing one year of data was enough to only obtain the linear and quadratic terms.

Comparing figures 7.3 and 7.6, we see that the second mode is quite different between the two series. There are similarities in some regions, but the geography of the spatial mode is obviously different. The two time series have a similar quadratic shape, but the period of the signal is also clearly different, as CHAMP covers almost twice as much time. We can argue that this mode 2 from Swarm includes the behaviour that we observe in both modes 2 and 3 from CHAMP. The PCA method does not allow to properly separate them in the Swarm dataset due to the short length of the series and as such they appear as a combined mode. Not shown in this section, but present in appendix B, we can see the spatial patterns of the first modes for both CHAMP and Swarm for the sub-auroral latitudes. When comparing with the global modes, we do not see significant differences. This result is valid for all modes explained with internal harmonic fields, as would be expected. If they have an internal source, not specific to a particular region of the globe, as a field with origin in the core would have, removing a few observatories will not compromise the global view. This would not be true if the mode had a source in a specific region in the poles, as removing these data points would lead the mode to change drastically.

The fifth mode from CHAMP and fourth from Swarm both have semi-annual signals, but do not have consistent spatial features. Looking at the misfit to the internal and external harmonic field models (figure 7.8) we see that neither of these models explain those modes satisfactorily. Note also that those modes are quite dependent on the choice of region used for the PCA decomposition. Swarm brings a clearer semi-annual signal to this mode (see figure 7.7(c)), but the fit of its spatial structure to internal and external harmonic models did not allow us to better define it. For CHAMP, the annual signal is ordered fourth using a global grid and fifth when using a sub-auroral grid, changing places with the semi-annual mode. As we noticed in figure

7.2, these two modes are not completely separated using the North's rule of thumb. But the downgrading of the annual mode when using only VOs out of the auroral regions might also be due to it having a source largely represented there. The cropping of this region in the dataset would then deteriorate the resolution of the annual mode.

In the end, certain modes obtained in previous sections seem more interesting than others. Mode 1 from both datasets, mode 3 and mode 4 from CHAMP and mode 3 from Swarm are the ones that have features with more plausible interpretations. We will focus our interpretation on these modes, corresponding to two internal modes and one external according to previous section.

7.4.1 The linear mode from CHAMP and Swarm

The first mode of the PCA decomposition shows a linear trend (figures 7.4(a) and 7.7(a)) i.e. the time average secular variation. The spatial structure (in figures 7.3 and 7.6) associated with it, can be associated to a large extent with the movement of the eccentric dipole that we considered in chapters 5 and 6 to account for the motion of the particle flux anomaly in the South Atlantic region.

We modelled the field as a simple point dipole moving away from the Earth's center, in a direction opposite to the Atlantic sector, with its magnetic moment rotating relative to the geographic frame. The spatial signature we obtain for the associated secular variation (difference between the field obtained at consecutive epochs) is similar to the spatial pattern of mode 1.

To make simulations of the main field and the secular variation considering only this moving eccentric dipole, the CHAOS-6 model was used to calculate the position and tilt of the eccentric dipole for the period of 1997 to 2016. Using some arbitrary value for the magnetic dipole moment, the magnetic field was computed in the reference frame of the eccentric and tilted dipole and then rotated to the geographic reference frame and represented at the surface of the Earth. The three parameters that identify the eccentric dipole are its dipole moment intensity, the displacement relative to the

Earth's center and the inclination (or tilt) relative to the geographic frame. We fixed the dipole moment at some arbitrary value and considered the displacement and tilt separately and together and we compared the results with the results for mode 1 from the PCA analysis. Only when we consider the simultaneous variation of those two parameters, does the secular variation resulting from this calculation resemble, for all three components the components of the first mode of the PCA decomposition for both CHAMP and Swarm VO data.

R.m.s. values for the contribution of this empirical displacement and tilt of the eccentric dipole to the secular variation of the geomagnetic field during recent years are, from results in the previous section (see figure 7.4(a) and 7.7(a)), about 57.7 nT/yr from CHAMP and 50.6 nT/yr from Swarm. Note that this is a factor of about 3.5 larger than the much more familiar decay of the dipole moment.

To compute the tilt and displacement of the eccentric dipole at each epoch, the equations from [Fraser-Smith, 1987] were used. To calculate the position and inclination of the dipole based on the SH coefficients, we first define,

$$\begin{aligned}
 L_0 &= 2g_1^0g_2^0 + \sqrt{3}(g_1^1g_2^1 + h_1^1h_2^1) \\
 L_1 &= -g_1^1g_2^0 + \sqrt{3}(g_1^0g_2^1 + g_1^1g_2^2 + h_1^1h_2^2) \\
 L_2 &= -h_1^1g_2^0 + \sqrt{3}(g_1^0h_2^1 + g_1^1h_2^2 - h_1^1g_2^2) \\
 m^2 &= g_1^{02} + g_1^{12} + h_1^{12} \\
 E &= (L_0g_1^0 + L_1g_1^1 + L_2h_1^1)/4m^2
 \end{aligned} \tag{7.3}$$

where g_i^i and h_i^i are the SH coefficients, and L_0 , L_1 , L_2 , m^2 and E are variables introduced only for simplification.

Next we define the translation matrix A as:

$$\mathbf{A} = \begin{bmatrix} A_1 & A_2 & A_3 \\ A_1 & A_2 & A_3 \\ A_1 & A_2 & A_3 \end{bmatrix} \tag{7.4}$$

with $A_1 = a(L_1 - Eg_1^1)/3m^2$, $A_2 = a(L_1 - Eg_1^1)/3m^2$, $A_3 = a(L_0 - Eg_1^0)/3m^2$ and a the radius of the Earth.

The rotation matrix can be written as R ,

$$\mathbf{R} = \begin{bmatrix} \cos \theta \cos \phi & \cos \theta \sin \phi & -\sin \theta \\ -\sin \phi & \cos \phi & 0 \\ \sin \theta \cos \phi & \sin \theta \sin \phi & \cos \theta \end{bmatrix} \quad (7.5)$$

where $\theta = -g_1^0 / \sqrt{g_1^{0^2} + g_1^{1^2} + h_1^{1^2}}$ and $\phi = -h_1^1 / \sqrt{g_1^{1^2} + h_1^{1^2}}$. Finally we have the tools to calculate the cartesian coordinates of each point on the eccentric and tilted dipole frame, written in equation 7.6.

$$\mathbf{X}_f = \mathbf{R} \times (\mathbf{X}_i - \mathbf{A}) \quad (7.6)$$

The CHAOS-6 model is used to obtain matrices R and A at any given moment. With this, we can transform the coordinates of a regular grid of points on the Earth's surface into the reference frame of the eccentric dipole (equation 7.6). We then compute vector components of the dipole field at each grid point. Finally, these components are rotated back to the geocentric frame and represented at the Earth's surface. Figure 7.10 shows the secular variation computed from the eccentric dipole field model. The same large space scale structures can be seen when looking at the annual rate of change of the IGRF field model [Thébault et al., 2015].

In order to compare quantitatively the SV from the model to mode 1, the correlation between them was calculated according to equation 7.7.

$$R(P^k, P^M) = \frac{P^{kT} P^M}{\sqrt{P^{kT} P^k} \sqrt{P^{MT} P^M}}, \quad P^k = \begin{bmatrix} P_r^k \\ P_\theta^k \\ P_\phi^k \end{bmatrix} \quad (7.7)$$

where P^k is the array of all three components of mode k and P^M is the model.

Figure 7.11 shows the correlation coefficient (R) between the model and all modes from CHAMP and Swarm. It is clear that mode 1 is the one with highest correlation, with a peak during the first half of 2010. In figure 7.10

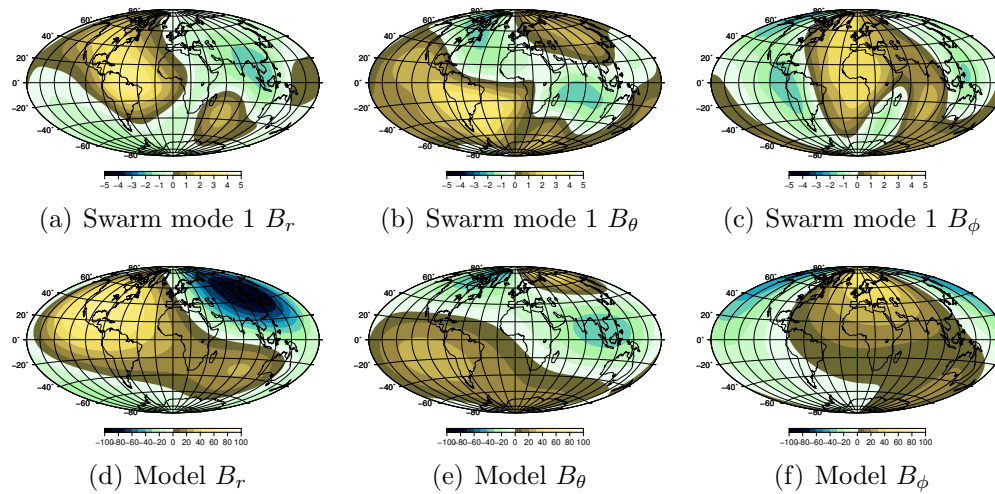


Figure 7.10 – Representation of the spatial charts (B_r , B_θ and B_ϕ) of the first mode of the PCA decomposition, for the global grid, using data from Swarm (top). Secular Variation due to translation and rotation of the eccentric dipole, for the first half of 2010 (bottom). The color scale ranges from -5 to 5 (normalised values) on the top row and from -100 to 100 (normalised values) on the bottom row.

the charts for B_r , B_θ and B_ϕ for this period are shown, and although the model features (bottom) are simplified versions of the modes, we can clearly see the same structures.

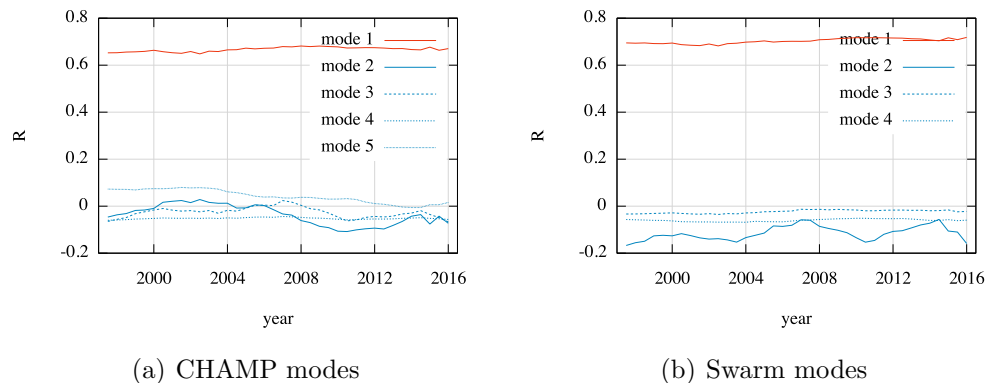


Figure 7.11 – Correlation between CHAMP (left) and Swarm (right) spatial features of PCA modes with the SV from the model based on the movement and rotation of the eccentric dipole. This was computed with the CHAOS-6 model, between 1997 and 2016.

7.4.2 The cubic polynomial mode from CHAMP

Mode 3 from CHAMP is the smallest lengthscale PCA mode of the internal part of the field that we can observe with our datasets (figure 7.12). The spatial structure of this mode is quite interesting, namely the radial component (figure 7.12(a)).

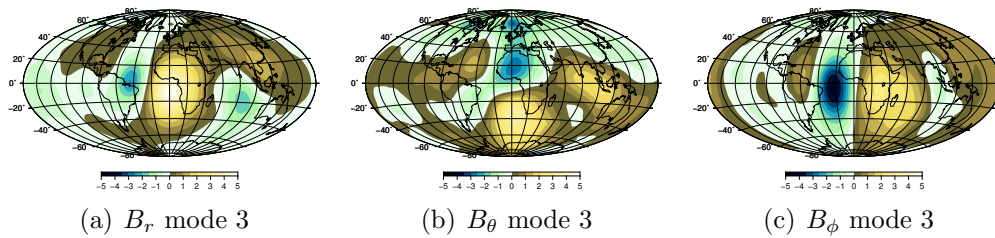


Figure 7.12 – Representation of the spatial charts (B_r , B_θ and B_ϕ) of the third mode of the PCA decomposition, for the global grid, using data from CHAMP. The color scale ranges from -5 to 5 (normalised values).

A similar structure can be found in [Lesur et al., 2008, Chulliat et al., 2010, Chulliat and Maus, 2014], and has been associated with pulses of secular acceleration (SA) in 2006 and 2009 and geomagnetic jerks in 2003, 2007 and 2011. In [Pais et al., 2015a], the same method used here was applied directly to SA models and a mode with a similar space structure appeared, reinforcing the association of mode 3 from CHAMP with oscillations or pulsations seen in the secular acceleration. There, pulses with the same geometry of the present mode 3 from CHAMP were detected around 1985 and 1996. In [Chulliat and Maus, 2014], several SA charts are shown, and those with similar structure to mode 3 occur in 2006 and 2009, with opposite phases. If we look at the time series of our mode 3, the local maximum and minimum of the cubic polynomial correspond to the years 2006 and 2009. The changes in sign of concavity occur close to 2004.7 and 2007, dates when jerks have been detected [Olsen and Mandea, 2008, Chulliat et al., 2010]. If we multiply the spatial mode and the corresponding time series, this would lead to different sign values in those two epochs, concurring with the results in [Chulliat and Maus, 2014]. Nonetheless, the hypothesis that these modes correspond to a wave do not agree well with our results. We only observe

a fixed spatial feature that oscillates in intensity over time. PCA is able to analyse wave signals, but only by associating two separate modes to a single wave. The two modes would have to be phase shifted by 90° both in time and space and with similar amplitudes. This is not the case in our work, we can only make a connection with the spatial features present in [Chulliat and Maus, 2014].

7.4.3 Annual oscillation modes from CHAMP and Swarm

Modes 4 from CHAMP and 3 from Swarm show spatial structures pulsating with an approximately annual period. They can not be simply due to a harmonic field of internal origin (relative to the VOs altitude), but the contribution of an internal component can not be excluded. Interpretation of these modes is not straightforward as external fields have been removed as much as possible during the construction of VO series. In the previous section, we showed that it is not simply an external harmonic field, neither. Possibly, contributions from internal (ionosphere) and external (magnetosphere) sources are present, as well as from electric currents crossing the altitude of the satellites. For this mode, the time series (figures 7.4 and 7.7) change significantly depending on the grid and show a clear annual dependence. The spatial structure, namely the radial component (figures 7.3(g) and 7.6(g)) is very interesting. The most identifiable structure is a ring around the equator, characteristic of a zonal quadrupolar geometry. This could be associated with auroral currents in the ionosphere, aligned along parallels. However, the complicated geometry of the corresponding B_θ is indicative of a more complex source for this mode.

The spatial structure of mode 3 from Swarm (figure 7.6) is similar to mode 4 from CHAMP (figure 7.3), but some differences can be observed. Focusing on the radial component, we see the ring aspect is much clearer with Swarm. The annual variation in the time series (figure 7.7(c)) is also much clearer. The difference in time series between global and sub-auroral grids is still present, with the sub-auroral region producing slightly lower amplitude, but both series show a smoother behaviour than in CHAMP. While in CHAMP

we observed a switch between the last two modes when changing grid, this does not happen in Swarm. This means that the modes are better separated using this dataset.

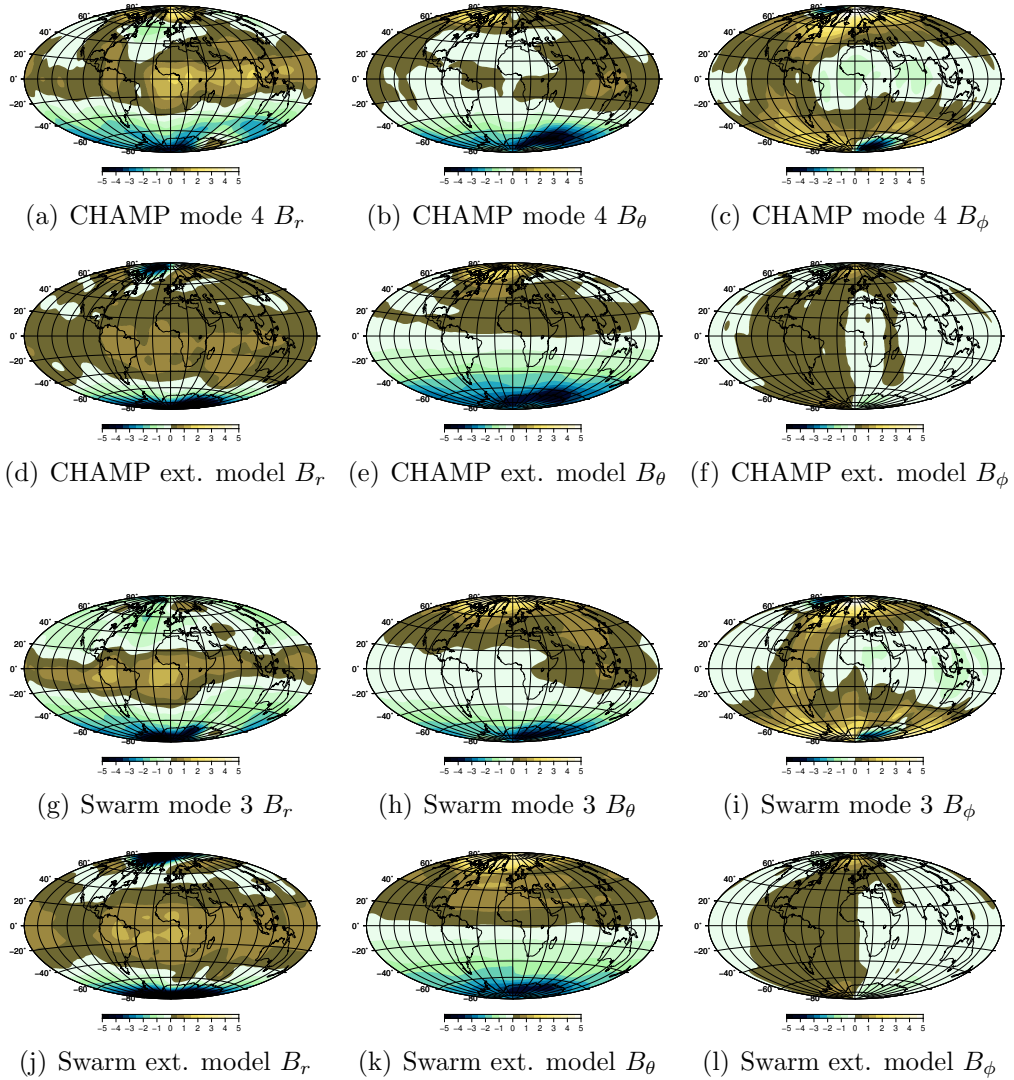


Figure 7.13 – Representation of the spatial patterns (B_r , B_θ and B_ϕ) from CHAMP mode 4 (top), the results of the fit to CHAMP considering an external harmonic field (top-middle), Swarm mode 3 (bottom-middle) and the results of the fit to Swarm considering an external harmonic field (bottom). The color scale ranges from -5 to 5 (normalised values).

Figure 7.13 shows the results of fitting an external harmonic field to both mode 4 from CHAMP and mode 3 from Swarm. The model for Swarm seems

to fit better to the data. This might be due to the increased height at which the VOs are calculated, where less currents are present. Also Swarm satellites sample twice as much local times allowing a better separation of ionospheric and magnetospheric fields. The spatial charts in figure 7.13(j) and figure 7.13(k) are consistent with two ring currents around the poles. The one in the North going westward and the one in the South going eastward. We have to remember that this model was constructed based on external sources, and ionospheric currents would appear as internal to the Swarm satellite. This could still represent the signal from such currents even though they would not be the sole source for this mode.

Chapter 8

Conclusions and Perspectives

In this final chapter, we summarise our results and mention further studies that could add on to them.

In chapter 5 we introduced the notion of a time varying L-shell reference frame. This choice originated from the difficulty to properly separate the PCA modes of particle flux data using a geographical grid. The L-shell reference frame proved to be very useful in allowing to separate the evolution of the proton flux over the South Atlantic Anomaly region into a component associated with the secular variation of the Earth's magnetic field, and another due to the variation of thermospheric density caused by solar activity. The drift of the magnetic field was obtained using the eccentric dipole model for the main field evolution, which is the main requirement to construct the L-shell reference frame.

From the PCA decomposition, we retrieved a main principal mode that represents the spatial location and time variation of the total flux of protons over the SAA and a second mode that represents the movement of the particle flux among different L-shells due to changes in thermospheric density. When considering a longer time series of the same kind of data, as was done in chapter 6, we validated the previous results and observed some new behaviours. The most striking one is the trend observed in the time series, when considering 26 years of data. The trend in mode 1 may be explained by the observed gradual contraction of the thermosphere, due to CO₂ accu-

mulation in the stratosphere and higher altitude layers of the atmosphere. In this chapter we also analysed two other datasets, from the Jason-2 satellite. This allowed us to investigate the variability of higher energetic particle flux and the changes in particle flux with altitude. At high altitude, the flux of particles above the SAA is much less variable. We interpret also our results from the distribution of the charged particles in the different L-shells as a function of their energy.

We also applied PCA on geomagnetic data and showed that without the need of considerations, the method allows for a good separation between internal and external sources of the field. We obtained three internal modes, but only on the longer dataset. Using even longer datasets, it is to be expected that further internal modes can be obtained. Mode 1 corresponds simply to the average secular variation, which is dominated by the evolution of the eccentric dipole (location, orientation and intensity). This is consistent with our previous observation that the evolution of the dipole is enough for describing the slow time variation of the particle flux. This PCA mode can then be used to create a model of the particle flux evolution. Mode three shows spatial features similar to other studies [Lesur et al., 2008, Chulliat et al., 2010, Pais et al., 2015b], but we do not associate this mode to a wave as previously suggested. The other interesting mode has mixed sources. It is neither completely external, nor internal. The annual signal of this mode, together with the spatial features suggests it is due to currents in the polar regions. These are sources external to the globe but not to the satellite orbits. The annual signal of geomagnetic field data is well known as it prevented modellers from investigating the main field at high frequency. The annual signal overshadows indeed signals with periods less than 2-3 years from the core (the third mode from CHAMP has period of about 5 years). from the core. With the PCA decomposition we have been able to associate a global geographical distribution to the annual signal and this might prove useful in correcting for it in future studies.

This work led to several interesting results, but many avenues remain open to explore. The construction of a model based on the SV of the eccentric dipole in order to predict the evolution of particle flux is one of them. Also,

we would like to explore further the application of PCA to geomagnetic data, possibly by combining different datasets (firstly the CHAMP and Swarm ones), much like in chapter 6, to produce a longer time series.

ESA has recently processed anew the records of the vectorial magnetometers of the Swarm satellites, using a new calibration that takes into account the variable heating of the instrument from the Sun. Once VO series are obtained from these new records, it will be enlightening to undertake a PCA analysis of these new VO series. There is still much to do using our PCA analysis in order to better compare CHAMP and Swarm records and to document the benefit of the Swarm multiple satellite configuration. Finally combining VO and ground observatories series, we may be able to estimate the magnetic field induced in the solid Earth and to improve our knowledge of the electrical conductivity of the globe.

References

- [Andrews et al., 1987] Andrews, D. G., Holton, J. R., and Leovy, C. B. (1987). *Middle Atmosphere Dynamics*. Academic Press. p. 82
- [Antonucci and Marocchi, 1978] Antonucci, E. and Marocchi, D. (1978). Phase reversals in the polar magnetic fields of the Sun and in the annual and semiannual variations in cosmic ray intensity. *The Astro. J.*, 220:712–718. p. 93
- [Aubert, 2015] Aubert, J. (2015). Geomagnetic forecasts driven by thermal wind dynamics in the Earth’s core. *Geophys. J. Int.*, 203:1738–1751. p. 76
- [Baker, 2004] Baker, D. N. (2004). *Effects of Space Weather on Technology Infrastructure*, chapter 1. Kluwer Academic Publishers. p. 28
- [Balasis et al., 2016] Balasis, G., Potirakis, S. M., and Mandea, M. (2016). Investigating Dynamical Complexity of Geomagnetic Jerks Using Various Entropy Measures. *Front. Earth Sci.*, 4. p. 27
- [Barraclough, 1974] Barraclough, D. (1974). Spherical harmonic analysis of the geomagnetic field for eight epochs between 1600 and 1910. *Geophys. J. Royal Astro. Soc.*, 36. p. 26
- [Bhavnani and Vancour, 1991] Bhavnani, K. H. and Vancour, R. P. (1991). Coordinate systems for space and geophysical applications. Technical report, Phillips laboratory air force systems command. p. xix, 10
- [Boscher et al., 2011] Boscher, D., Bourdarie, S., Falguère, D., Lazaro, D., Bourdoux, P., Baldran, T., Rolland, G., Lorfèvre, E., and Ecoffet, R.

- (2011). In Flight Measurements of Radiation Environment on Board the French Satellite JASON-2. *IEEE Transactions on Nucl. Science*, 58:916–922. p. 86, 87
- [Boscher et al., 2014] Boscher, D., Cayton, T., Maget, V. Bourdarie, S., Lazaro, D. Baldran, T. B. P., Lorfèvre, E., Rolland, G., and Ecoffet, R. (2014). In-Flight Measurements of Radiation Environment on Board the Argentinean Satellite SAC-D. *IEEE Transactions on Nucl. Science*, 61(6):3395–3400. p. 87
- [Bouligand et al., 2016] Bouligand, C., Gillet, N., Jault, D., Schaeffer, N., Fournier, A., and Aubert, J. (2016). Frequency spectrum of the geomagnetic field harmonic coefficients from dynamo simulations. *Geophys. J. Int.*, 207(2):1142–1157. p. 26
- [Bourdarie et al., 2014] Bourdarie, S., Falguere, D., Inguibert, C., Deneau, C., Vaillé, J.-R., Lorfèvre, E., and Ecoffet, R. (2014). Correlation of in-flight displacement damage on the OSL sensor with space environment on-board Jason-2 spacecraft. *IEEE Transactions on Nucl. Science*, 61. p. 44
- [Bullard et al., 1950] Bullard, E. C., Freedman, C., Gellman, H., and Nixon, J. (1950). The westward drift of the Earth’s magnetic field. *Phil. Trans. R. Soc. Lond. A*, 243(859). p. 26, 37
- [Casadio and Arino, 2011] Casadio, S. and Arino, O. (2011). Monitoring the South Atlantic Anomaly using ATSR instrument series. *Adv. Space Res.*, 48:1056–1066. p. 91, 94, 137
- [Chulliat and Maus, 2014] Chulliat, A. and Maus, S. (2014). Geomagnetic secular acceleration, jerks, and a localized standing wave at the core surface from 2000 to 2010. *J. Geophys. Res. Solid Earth*, 119(3). p. 114, 115
- [Chulliat et al., 2010] Chulliat, A., Thébaud, E., and Hulot, G. (2010). Core field acceleration pulse as a common cause of the 2003 and 2007 geomagnetic jerks. *Geophys. Res. Lett.*, 37(7). p. 114, 120

- [Emmert, 2015] Emmert, J. T. (2015). Altitude and solar activity dependence of 1967-2005 thermospheric density trends derived from orbital drag. *J. Geophys. Res. Space Physics*, 120(4). p. xxi, xxiii, 49, 82, 83, 84, 91, 93, 94
- [Emmert et al., 2012] Emmert, J. T., Stevens, M. H., Bernath, P. F., Drob, D. P., and Boone, C. D. (2012). Observations of increasing carbon dioxide concentration in Earth's thermosphere. *Nature Geoscience*, 5(868-871). p. 82
- [eoPortal Directory, 2017a] eoPortal Directory (2017a). CALIPSO (Cloud-Aerosol Lidar and Infrared Pathfinder Satellite Observations). p. 43
- [eoPortal Directory, 2017b] eoPortal Directory (2017b). CHAMP (Challenging Minisatellite Payload). p. 44, 45
- [eoPortal Directory, 2017c] eoPortal Directory (2017c). Jason-2 / OSTM. p. 44
- [eoPortal Directory, 2017d] eoPortal Directory (2017d). NOAA POES Series - 5th Generation Satellites. p. 42, 43
- [eoPortal Directory, 2017e] eoPortal Directory (2017e). Swarm (Geomagnetic LEO Constellation). p. 46, 47
- [Evans et al., 2008] Evans, D., Garrett, H., Jun, I., Evans, R., and Chow, J. (2008). Long-term observations of the trapped high-energy proton population ($L < 4$) by the NOAA Polar Orbiting Environmental Satellites (POES). *Adv. Space Res.*, 41(8):1261–1268. p. 41
- [Finlay et al., 2016] Finlay, C. C., Olsen, N., Kotsiaros, N., Gillet, N., and Toffner-Clausen, L. (2016). Recent geomagnetic secular variation from *Swarm* and ground observatories as estimated in the CHAOS-6 geomagnetic field model. *Earth Planets Space*, 68(112). p. 35, 36, 38, 96
- [Finlay et al., 2015] Finlay, C. C., Olsen, N., and Tøffner-Clausen, L. (2015). DTU candidate field models for IGRF-12 and the CHAOS-5 geomagnetic field model. *Earth, Planets and Space*, 67(1):1–17. p. 50

- [Fraser-Smith, 1987] Fraser-Smith, A. C. (1987). Centered and eccentric geomagnetic dipoles and their poles, 1600 - 1985. *Rev. Geophys.*, 25:1–16. p. 37, 39, 111
- [Fürst et al., 2009] Fürst, F., Wilms, J., Rothschild, R., Pottschmidt, K., Smith, D., and Lingenfelter, R. (2009). Temporal variations of strength and location of the South Atlantic Anomaly as measured by RXTE. *Earth Planet. Sci. Lett.*, 281:125–133. p. 63, 76
- [Gillet et al., 2015a] Gillet, N., Barrois, O., and Finlay, C. C. (2015a). Stochastic forecasting of the geomagnetic field from the COV-OBS.x1 geomagnetic field model, and candidate models for IGRF-12. *Earth, Planets and Space*, 67. p. 36
- [Gillet et al., 2015b] Gillet, N., Jault, D., and Finlay, C. C. (2015b). Planetary gyre and time-dependent midlatitude eddies at the Earth’s core surface. *J. Geophys. Res.*, 120(6). p. 36
- [Gillet et al., 2013] Gillet, N., Jault, D., Finlay, C. C., and Olsen, N. (2013). Stochastic modeling of the Earth’s magnetic field: Inversion for covariances over the observatory era. *Geochem. Geophys. Geosyst.*, 14(4). p. 36
- [Gillet et al., 2009] Gillet, N., Pais, M. A., and Jault, D. (2009). Ensemble inversion of time-dependent core flow models. *Geochem. Geophys. Geosyst.*, 10(6). p. 36
- [Glassmeier et al., 2004] Glassmeier, K., Vogt, J., Stadelmann, A., and Buchert, S. (2004). Concerning long-term geomagnetic variations and space climatology. *Ann. Geophys.*, 22:3669–3677. p. 76
- [Gledhill, 1976] Gledhill, J. A. (1976). Aeronomic Effects of the South Atlantic Anomaly. *Rev. Geophys. Space Phys.*, 14(2):173–187. p. 64, 74
- [Gubbins et al., 2006] Gubbins, D., Jones, A. L., and Finlay, C. C. (2006). Fall in earth’s magnetic field is erratic. *Science*, 312:900–902. p. 26

- [Guo et al., 2008] Guo, J., Wan, W., Forbes, J. M., Sutton, E., Nerem, R. S., and Bruinsma, S. (2008). Interannual and latitudinal variability of the thermosphere density annual harmonics. *J. Geophys. Res.*, 113. p. 92
- [Halley, 1692] Halley, E. (1692). An Account of the Cause of the Change of the Variation of the Magnetic Needle; With an Hypothesis of the Structure of the Internal Parts of the Earth. *Phil. Trans. R. Soc. Lond. A*, 17(195):563–578. p. 26, 37
- [Hannachi et al., 2007] Hannachi, A., Jolliffe, I. T., and Stephenson, D. B. (2007). Empirical orthogonal functions and related techniques in atmospheric science: A review. *International Journal of Climatology*, 27:1119–1152. p. 55
- [Hartmann and Pacca, 2009] Hartmann, G. and Pacca, I. (2009). Time evolution of the South Atlantic magnetic anomaly. *Anais de Academia Brasileira de Ciências*, 81:243–255. p. 27
- [Hell, 2010] Hell, N. (2010). The Evolution of the South Atlantic Anomaly Measured by RHESSI. Master’s thesis, Erlangen Centre for Astroparticle Physics. p. 27, 29
- [Holme, 2007] Holme, R. (2007). *Treatise on Geophysics: Large-Scale Flow in the Core*, volume 8, chapter 8.04. Elsevier. p. 25
- [Hulot et al., 2010] Hulot, G., Finlay, C. C., Constable, C. G., Olsen, N., and Manda, M. (2010). The magnetic field of planet Earth. *Space Sci. Rev.*, 152:159–222. p. xx, 34, 35
- [Hulot et al., 2015] Hulot, G., Sabaka, T. J., Olsen, N., and Fournier, A. (2015). *Treatise on Geophysics: The Present and Future Geomagnetic field*, volume 1, chapter 5.02. Elsevier. p. 31, 33
- [Hunt et al., 2009] Hunt, W. H., Winker, D. M., Vaughan, M. A., Powell, K. A., Lucker, P. L., and Weimer, C. (2009). CALIPSO Lidar Description and Performance Assessment. *J. Atmos. Oceanic Technol.*, 26:1214–1228. p. 43

- [Jackson and Finlay, 2007] Jackson, A. and Finlay, C. C. (2007). *Treatise on Geophysics: Geomagnetic Secular Variation and Its Applications to the Core*, volume 5, chapter 5.05. Elsevier. p. 27, 33
- [Jackson et al., 2000] Jackson, A., Jonkers, R. T., and Walker, M. R. (2000). Four centuries of geomagnetic secular variation from historical records. *Phil. Trans. R. Soc. Lond. A*, 358:957–990. p. 36
- [Jault et al., 1988] Jault, D., Gire, C., and Mouël, J.-L. (1988). Westward drift, core motions and exchanges of angular momentum between core and mantle. *Nature*, 333:353–356. p. 26
- [Jentsch and Wibberenz, 1980] Jentsch, V. and Wibberenz, G. (1980). An Analytic Study of the Energy and Pitch Angle Distribution of Inner-Zone Protons. *J. Geophys. Res. Space Physics*, 85:1–8. p. 86, 89, 90, 93
- [Jolliffe, 2002] Jolliffe, I. T. (2002). *Principal Component Analysis*. Springer. p. 57, 58
- [Jones et al., 2017] Jones, A. D., Kanekal, S. G., Baker, D. N., Klecker, B., Looper, M. D., M. J. E., and Schiller, Q. (2017). SAMPEX observations of the South Atlantic anomaly secular drift during solar cycles 22-24. *Space Weather*, 15(1). p. 88
- [Jonkers et al., 2003] Jonkers, R. T., Jackson, A., and Murray, A. (2003). Four Centuries of Geomagnetic data from Historical Records. *Rev. Geophys.*, 41(2). p. 31
- [Kallenrode, 2004] Kallenrode, M.-B. (2004). *Space Physics*. Springer. p. 12
- [Kan and Lee, 1979] Kan, J. R. and Lee, L. C. (1979). Energy coupling function and solar wind-magnetosphere dynamo. *Geophys. Res. Lett.*, 6(7):577–580. p. 96
- [Kappenman, 2012] Kappenman, J. (2012). A perfect storm of planetary proportions. *IEEE Spectrum*, 49:26–31. p. 2

- [Kauristie et al., 2017] Kauristie, K., Morschhauser, A., Olsen, N., Finlay, C. C., McPherron, R. L., Gjerloev, J. W., and Opgenoorth, H. J. (2017). On the Usage of Geomagnetic Indices for Data Selection in Internal Field Modelling. *Space Sci. Rev.*, 206:61–90. p. 49, 50, 51
- [Kivelson and Russel, 1995] Kivelson, M. G. and Russel, C. T. (1995). *Introduction to Space Physics*. Cambridge University Press. p. xx, 13
- [Korte et al., 2005] Korte, M., Genevey, A., Constable, C. G., Frank, U., and Schnepf, E. (2005). Continuous geomagnetic field models for the 7 millennia: 1. A new global data compilation. *Geochem. Geophys. Geosyst.*, 6(2). p. 26
- [Koskinen, 2011] Koskinen, H. (2011). *Physics of Space Storms: From the Solar Surface to the Earth*. Springer. p. xix, 5, 6, 8, 10, 11, 12, 22
- [Lean, 1991] Lean, J. (1991). Variations in the Sun’s radiative output. *Rev. Geophys.*, 29(4). p. xix, 7
- [Leopardi, 2006] Leopardi, P. (2006). A partition of the unit sphere into regions of equal area and small diameter. *Electronic Trans. on Num. Analysis*, 25:309–327. p. 96
- [Lesur et al., 2017] Lesur, V., Wardinski, I., Baerenzung, J., and Holschneider, M. (2017). On the frequency of spectra of the core magnetic field Gauss coefficients. *Phys. of the Earth and Plan. Int.* p. 26
- [Lesur et al., 2008] Lesur, V., Wardinski, I., Rother, M., and Mandea, M. (2008). GRIMM: The GFZ Reference Internal Magnetic Model based on vector satellite and observatory data. *Geophys. J. Int.*, 173(2):382–394. p. 114, 120
- [Livermore et al., 2017] Livermore, P. W., Hollerbach, R., and Finlay, C. C. (2017). An accelerating high-latitude jet in Earth’s core. *Nature Geoscience*, 10:62–68. p. 47

- [Lockwood, 2005] Lockwood, M. (2005). Solar Outputs, Their Variations and Their Effects on Earth. In *The Sun, Solar Analogs and the Climate*. Springer. p. xix, 7
- [Loves, 1994] Loves, F. J. (1994). The geomagnetic eccentric dipole: fact and fallacies. *Geophys. J. Int.*, 118:671–679. p. 39
- [Luhmann et al., 2013] Luhmann, J. G., Petrie, G., and Riley, P. (2013). Solar origins of solar wind properties during the cycle 23 solar minimum and rising phase of cycle 24. *J. Adv. Res.*, 4:221–228. p. xix, 8
- [Mandea et al., 2000] Mandea, M., Bellanger, E., and Mouël, J.-L. (2000). A geomagnetic jerk for the end of the 20th century? *Earth Planet. Sci. Lett.*, 183:369–373. p. 27
- [Mandea et al., 2007] Mandea, M., Korte, M., Mozzoni, D., and Kotzé, P. (2007). The magnetic field changing over the southern African continent: a unique behaviour. *S. Afric. J. Geol.*, 110:193–202. p. 27
- [Mandea and Mayaud, 2004] Mandea, M. and Mayaud, P.-N. (2004). Guillaume le Nautonnier, un précurseur dans l’histoire du géomagnétisme. *Revue d’histoire des sciences*, 57:161–173. p. 31
- [Mandea and Olsen, 2006] Mandea, M. and Olsen, N. (2006). A new approach to directly determine the secular variation from magnetic satellite observations. *Geophys. Res. Lett.*, 33(15). p. 41, 95
- [Mcllwain, 1961] Mcllwain, C. E. (1961). Coordinates for Mapping the Distribution of Magnetically Trapped Particles. *J. Geophys. Res.*, 66(11):3681–3691. p. 20, 39
- [Mitchell, 1994] Mitchell, D. G. (1994). *Fundamentals of space systems: The space environment*, pages 45–98. Oxford Univ. Press. p. xx, 14
- [Miyoshi et al., 2000] Miyoshi, Y., Morioka, A., and Misawa, H. (2000). Long term modulation of low altitude proton radiation belt by the Earth’s atmosphere. *Geophys. Res. Lett.*, 27:2169–2172. p. 73, 75

- [Newell et al., 2007] Newell, P. T., Sotirelis, T., Liou, K., Meng, C.-I., and Rich, F. J. (2007). A nearly universal solar wind-magnetosphere coupling function inferred from 10 magnetospheric state variables. *J. Geophys. Res.*, 112. p. 96
- [Noel et al., 2014] Noel, V., Chepfer, H., Hoareau, C., Reverdy, M., and Cesana, G. (2014). Effects of solar activity on noise in CALIOP profiles above the South Atlantic Anomaly. *Atmos. Meas. Tech.*, 7:1597–1603. p. 63
- [North et al., 1982] North, G. R., Bell, T. L., and Cahalan, R. F. (1982). Sampling Errors in the Estimation of Empirical Orthogonal Functions. *American Meteo. Soc.*, 110:699–706. p. 55
- [Oliveria et al., 2014] Oliveria, J. S., Langlais, B., Pais, M. A., and Amit, H. (2014). A modified Equivalent Source Dipole method to model partially distributed magnetic field measurements, with application to Mercury. *J. Geophys. Res. Planets*, 120:1075–1094. p. 35
- [Olsen et al., 2015] Olsen, N., Hulot, G., Lesur, V., et al. (2015). The Swarm initial field model for the 2014 geomagnetic field. *Geophys. Res. Lett.*, 42:1092–1098. p. 35
- [Olsen et al., 2014] Olsen, N., Lühr, H., Finlay, C. C., Sabaka, T. J., Michaelis, I., Rauberg, J., and Tøffner-Clausen, L. (2014). The CHAOS-4 geomagnetic field model. *Geophys. J. Int.*, 197(2):815–827. p. 50, 96
- [Olsen et al., 2006] Olsen, N., Lühr, H., Sabaka, T., Manda, M., Rother, M., Tøffner-Clausen, L., and Choi, S. (2006). CHAOS - a model of Earth's magnetic field derived from CHAMP, Ørsted, and SAC-C magnetic satellite data. *Geophys. J. Int.*, 166:67–75. p. 35
- [Olsen and Manda, 2008] Olsen, N. and Manda, M. (2008). Rapidly changing flows in the Earth's core. *Nature Geoscience*, 1:390–394. p. 114
- [Olsen et al., 2017] Olsen, N., Ravat, D., Finlay, C. C., and Kother, L. K. (2017). LCS-1: a high-resolution global model of the lithospheric magnetic

- field derived from CHAMP and Swarm satellite observations. *Geophys. J. Int.*, 211:1461–1477. p. 47
- [Olsen and Stolle, 2012] Olsen, N. and Stolle, C. (2012). Satellite Geomagnetism. *Annual Review of Earth and Planetary Sciences*, 40:441–465. p. 3
- [Pais et al., 2015a] Pais, M. A., Alberto, P., and Pinheiro, F. J. G. (2015a). Time-correlated patterns from spherical harmonic expansions: Application to geomagnetism. *J. Geophys. Res. Solid Earth*, 120. p. 114
- [Pais et al., 2015b] Pais, M. A., Morozova, A. L., and Schaeffer, N. (2015b). Variability modes in core flows inverted from geomagnetic field models. *Geophys. J. Int.*, 200:402–420. p. 53, 120
- [Parks, 1991] Parks, G. K. (1991). *Physics of Space Plasmas*. Addison-Wesley. p. xix, 9
- [Prölss, 2004] Prölss, G. (2004). *Physics of the Earth’s Space Environment*, chapter 5. Springer. p. xx, xxix, 12, 15, 16, 17, 18, 19, 20, 21
- [Qin et al., 2014] Qin, M., Zhang, X., Ni, B., Song, H., Zou, H., and Sun, Y. (2014). Solar cycle variations of trapped proton flux in the inner radiation belt. *J. Geophys. Res. Space Physics*, 119(12):9658–9669. p. 75, 137
- [Richmond, 1995] Richmond, A. D. (1995). Ionospheric electrodynamics using magnetic apex coordinates. *J. Geomagn. Geoelectr.*, 47:191–212. p. 96
- [Roederer and Zhang, 2014] Roederer, J. G. and Zhang, H. (2014). *Dynamics of Magnetically Trapped Particles*. Springer, 2 edition. p. 15, 76
- [Sabaka et al., 2002] Sabaka, T. J., Olsen, N., and Langel, R. A. (2002). A comprehensive model of the quiet-time, near-Earth magnetic field: phase 3. *Geophys. J. Int.*, 151:32–68. p. 36

- [Sabaka et al., 2004] Sabaka, T. J., Olsen, N., and Purucker, E. (2004). Extending comprehensive models of the Earth’s magnetic field with Ørsted and CHAMP data. *Geophys. J. Int.*, 159:521–547. p. 97
- [Sabaka et al., 2015] Sabaka, T. J., Olsen, N., Tyler, R. H., and Kuvshinov, A. (2015). CM5, a pre-Swarm comprehensive geomagnetic field model derived from over 12 yr of CHAMP, Ørsted, SAC-C and observatory data. *Geophys. J. Int.*, 200:1596–1626. p. 31, 36
- [Schaefer et al., 2016] Schaefer, R., Paxton, L., Selby, C., Ogorzalek, B., Romeo, G., Wolven, B., and Hsieh, S.-Y. (2016). Observation and modeling of the South Atlantic Anomaly in low Earth orbit using photometric instrument data. *Space Weather*, 14:330–342. p. 63, 91, 93
- [Selesnick et al., 2014] Selesnick, R. S., Baker, D. N., Jaynes, A., Li, X., Kanekal, S. G., Hudson, M. K., and Kress, B. T. (2014). Observations of the inner radiation belt: CRAND and trapped solar protons. *J. Geophys. Res. Space Physics*, 119:6541–6552. p. 14, 88, 89
- [Shea and Smart, 2006] Shea, M. A. and Smart, D. F. (2006). Geomagnetic cutoff rigidities and geomagnetic coordinates appropriate for the Carrington flare epoch. *Adv. Space Res.*, 38:209–214. p. 2
- [Shore et al., 2016] Shore, R. M., Whaler, K. A., Macmillan, S., Beggan, C., Velínský, J., and Olsen, N. (2016). Decadal period external magnetic field variations determined via eigenanalysis. *J. Geophys. Res. Space Physics*, 121:5172–5184. p. 56
- [Solomon et al., 2013] Solomon, S. C., Qian, L., and Burns, A. G. (2013). The anomalous ionosphere between solar cycles 23 and 24. *J. Geophys. Res. Space Physics*, 118(10):6524–6535. 2013JA019206. p. xx, xxii, 24, 72
- [Storch and Zwiers, 2003] Storch, H. v. and Zwiers, F. W. (2003). *Statistical Analysis in Climate Research*, chapter 4. Cambridge University Press. p. 99

- [Sugiura, 1964] Sugiura, M. (1964). Hourly values of equatorial Dst for IGY. *Ann. Int. Geophys. Yr.*, 35. p. 96
- [Thébault et al., 2015] Thébault, E., Finlay, C. C., Beggan, C. D., Alken, P., Aubert, J., Barrois, O., Bertrand, F., Bondar, T., Boness, A., Brocco, L., Canet, E., Chambodut, A., Chulliat, A., Coisson, P., Civet, F., Du, A., Fournier, A., Fratter, I., Gillet, N., Hamilton, B., Hamoudi, M., Hulot, G., Jager, T., Korte, M., Kuang, W., Lalanne, X., Langlais, B., L ger, J.-M., Lesur, V., Lowes, F. J., Macmillan, S., Manda, M., Manoj, C., Maus, S., Olsen, N., Petrov, V., Ridley, V., Rother, M., Sabaka, T. J., Saturnino, D., Schachtschneider, R., Sirol, O., Tangborn, A., T ffner-Clausen, L., Vigneron, P., Wardinski, I., and Zvereva, T. (2015). International Geomagnetic Reference Field: the 12th generation. *Earth, Planets and Space*, 67. p. 112
- [Tsyganenko and Sitnov, 2005] Tsyganenko, N. A. and Sitnov, M. I. (2005). Modeling the dynamics of the inner magnetosphere during strong geomagnetic storms. *J. Geophys. Res. Space Physics*, 110. p. 50
- [UNOOSA, 2017] UNOOSA (2017). United Nations Office for Outer Space Affairs: Online Index of Objects Launched into Outer Space. p. 1
- [Vacaresse et al., 1999] Vacaresse, A., Boscher, D., Bourdarie, S., Blanc, M., and Sauvaud, J. A. (1999). Modeling the high-energy proton belt. *J. Geophys. Res.*, 104(A12):28601–28613. p. 66
- [Vernov et al., 1967] Vernov, S. N., Gorchakov, E. V., Shavrin, P. I., and Sharvina, K. N. (1967). Radiation Belts in the Region of the South-Atlantic Magnetic Anomaly. *Space Sci. Rev.*, 7:490–533. p. 64, 74
- [Willis et al., 2016] Willis, P., Heflin, M. B., Haines, B. J., Bar-Sever, Y. E., Bertiger, W. I., and Manda, M. (2016). Is the Jason-2 DORIS oscillator also affected by the South Atlantic Anomaly? *Adv. Space Res.*, 58:2617–2627. p. 41
- [Winker et al., 2007] Winker, D. M., Hunt, W. H., and McGill, M. J. (2007). Initial performance assessment of CALIOP. *Geophys. Res. Lett.*, 34. p. 41

- [Zawadzki et al., 2016] Zawadzki, L., Ablain, M., Carrere, L., Ray, R. D., Zelensky, N. P., Lyard, F., Guillot, A., and Picot, N. (2016). Reduction of the 59 -day error signal in the Mean Sea Level derived from TOPEX/Poseidon, Jason-1 and Jason-2 data with the latest FES and GOT ocean tide models. *Ocean Sci. Discuss.* p. 44, 90, 94

Appendix A

Application of PCA on simulated data

The movement of the South Atlantic particle flux anomaly, although not strictly a gaussian distribution with a changing center position, total amplitude and variance, it can be to a certain extent approximated as such. This was done in [Casadio and Arino, 2011] and [Qin et al., 2014].

To validate some of the assumptions made in the interpretation of the PCA modes calculated from the particle flux charts of POES and Jason-2 satellites, similar charts were created but this time with synthetic data represented by artificial gaussian distributions.

Several runs were conducted, changing the three main parameters mentioned above. First having a simple drift along a westward direction with a similar rate to the one documented in several articles about the South Atlantic Anomaly (run D). Second, a fluctuation of the total amplitude of the gaussian distribution, this oscillation being tied to the solar cycle for reference (run I). Then, a change in the area of the anomaly (through a change in the variance of the gaussian function, run S), which was also tied with the solar cycle. Lastly, all three parameters were taken into account at the same time in the last test to represent the actual evolution of the anomaly.

In the drift test (figure A.1(a), A.1(b), A.1(c) and figure A.2(a)), the only mode of importance is the second one, the first having no significant time

variation and the third being just an echo of the second with much lower energy. This corresponds to the second mode seen in the calculations with real data from POES 15, the dipole mode. The time series is very different, only a linear trend is present, but we have to consider that in this simple simulation, only a linear drift was introduced. It does not vary according to the solar cycle in the same way that the actual SAA particle flux does.

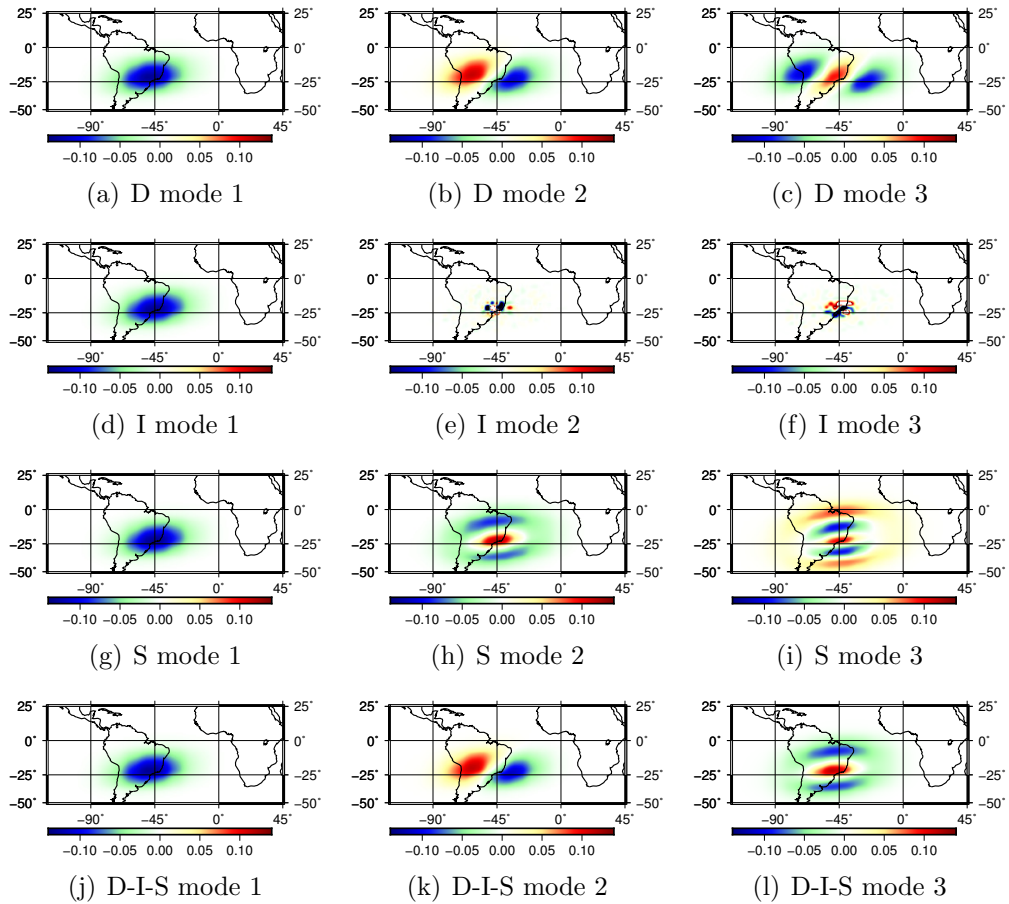


Figure A.1 – First three PCA spatial features from the gaussian test models. Drift (D) only test (top), intensity (I) only test (top middle), size (S) only mode (bottom middle) and all three behaviours (D-I-S) together (bottom).

From the intensity test (figure A.1(d), A.1(e), A.1(f) and figure A.2(b)), as expected, we only obtain a mode representing the variation of the intensity, the other two are low energy noise. This mode is the one always observed as the first mode in calculations with real data, and by far the most energetic,

containing more than 99% of the evolution of the system.

In the size test (figure A.1(g), A.1(h), A.1(i) and figure A.2(c)), the second mode is the most important one, with the first mode having a small variation just due to the fact that the changing in area affects the total intensity, and the third is a low energy echo, much like mode 3 in the drift test. This mode explains in some extent the third mode in the real data calculations, although it is not so clear there, as modes from different origins are all mixed.

By changing all the different parameters (figures A.1(j), A.1(k), A.1(l) and figure A.2(d)) at the same time we can see that the three modes are ordered as the real data ones when using a geographic reference frame. The time series do not fit perfectly, as a better modulation of the effects of the solar cycle would have to be taken into account. But the purpose of this simulation was to determine what kind of modes we would obtain with simple models for the variation of the particle flux geometry and position. We believe this strengthens the considerations made in chapter 5 regarding the source of the observed real modes.

The gaussians were calculated following equation A.1:

$$G(x, y) = A \exp^{-a(x-x_0)^2 - 2b(x-x_0)(y-y_0) + c(y-y_0)^2} \quad (\text{A.1})$$

where A denotes the amplitude of the gaussian and a , b and c are variables defined by:

$$a = \frac{\cos^2 \theta}{2c_x^2} + \frac{\sin^2 \theta}{2c_y^2} \quad (\text{A.2})$$

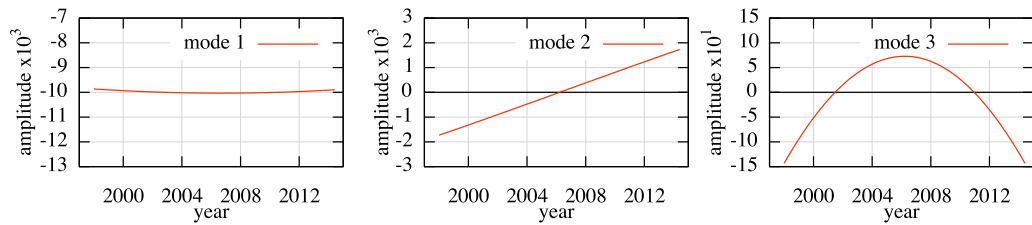
$$b = -\frac{\sin 2\theta}{4c_x^2} + \frac{\sin 2\theta}{4c_y^2} \quad (\text{A.3})$$

$$c = \frac{\sin^2 \theta}{2c_x^2} + \frac{\cos^2 \theta}{2c_y^2} \quad (\text{A.4})$$

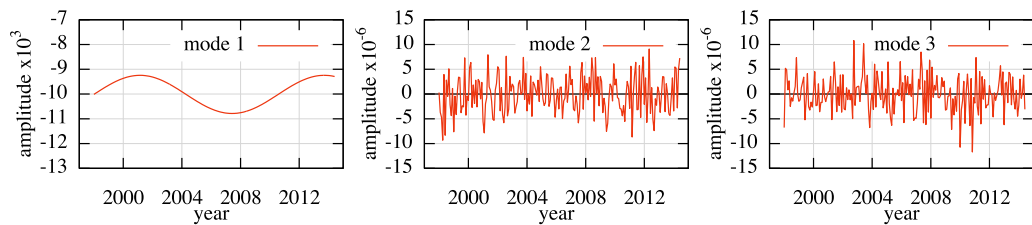
Here θ is a chosen fixed value of $\pi/20$, and c_x and c_y are factors responsible for the width of the gaussian in the x and y direction respectively for the longitude and latitude, using a local plane approximation.

For the drift test all these variables are kept constant and only the relative

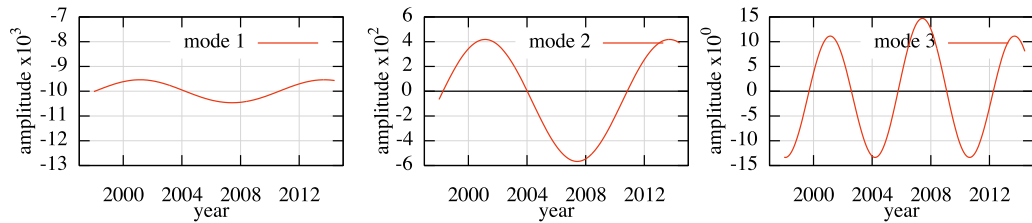
position of the gaussian changes. For the intensity test, only A varies, and for the size test the variables c_x and c_y are varied. The final test consists in applying all these variations at the same time.



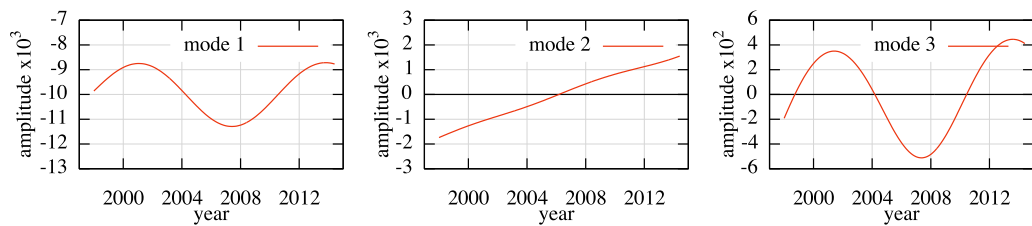
(a) Drift only (D)



(b) Intensity only (I)



(c) Size only (S)



(d) Complete model (D-I-S)

Figure A.2 – First three PCA time series from the gaussian test models. Drift (D) only test (top), intensity (I) only test (top middle), size (S) only mode (bottom middle) and all three behaviours (D-I-S) together (bottom).

Appendix B

CHAMP and Swarm PCA modes - supplementary material

The spatial modes from the PCA decomposition of the two datasets (CHAMP and Swarm) were analysed in both a global grid (using all the available VOs) and a sub-auroral grid (selecting only VOs between -60° and 60° latitude). This was done to look for the influence of auroral observatories in the decomposition. The figures below compare the spatial structures obtained with global and sub-auroral grids for each of the three components. Only the first five modes of CHAMP and the first four of Swarm are shown.

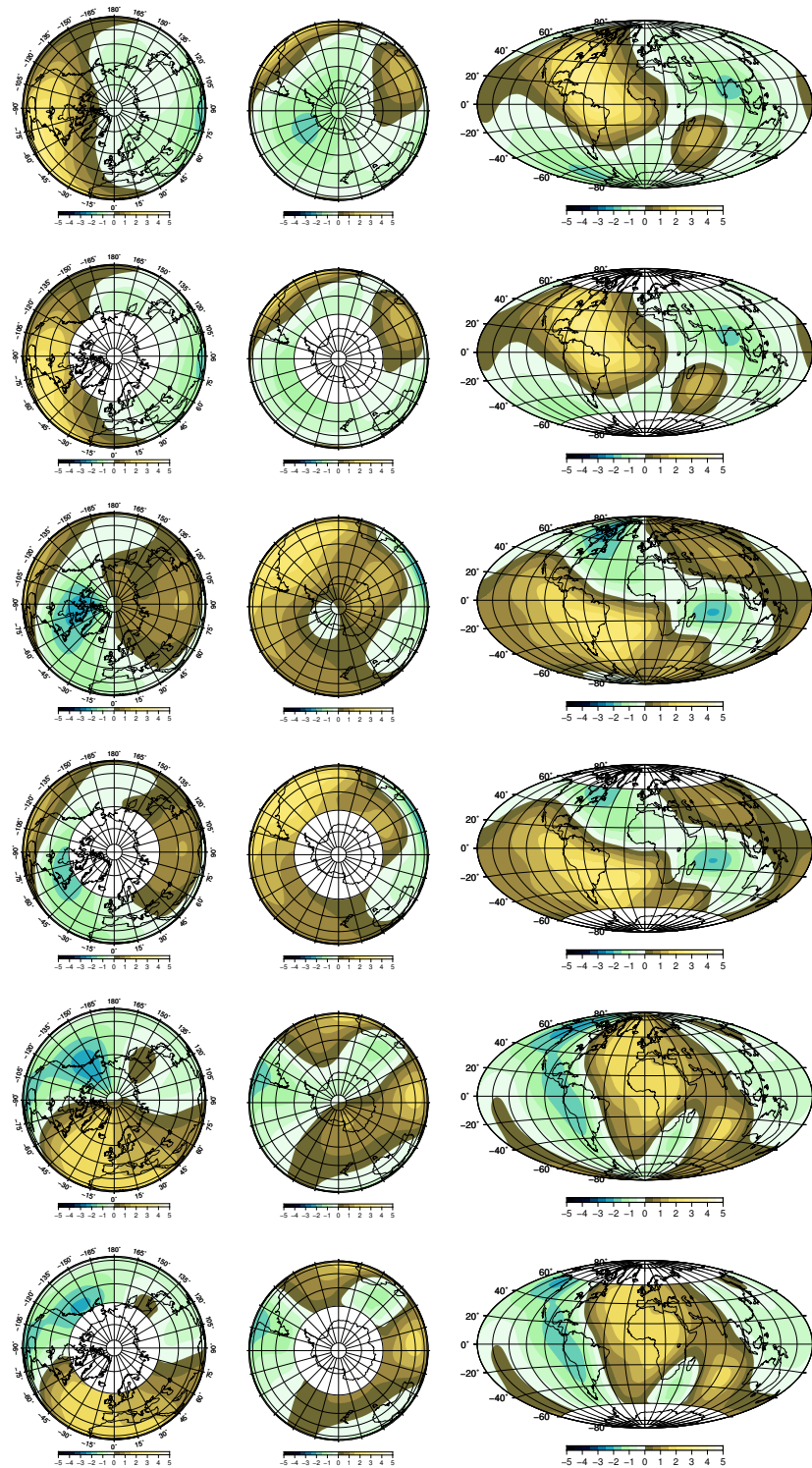


Figure B.1 – Representation of the spatial features (B_r (top two rows), B_θ (middle two rows) and B_ϕ (bottom two rows)) of PCA mode 1 for the global (1st, 3rd and 5th rows) and sub-auroral (2nd, 4th and 6th rows) grids from CHAMP data.

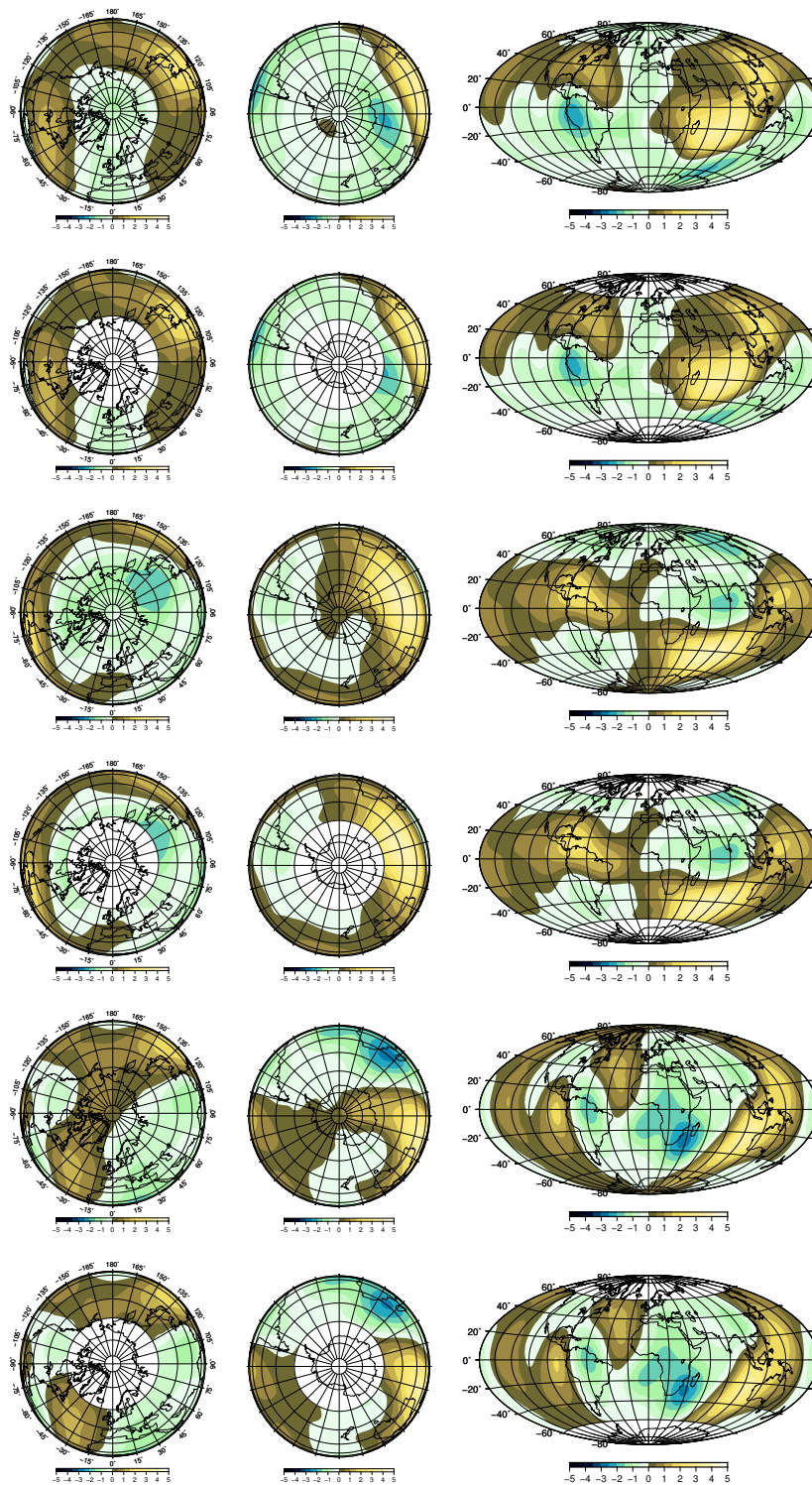


Figure B.2 – Representation of the spatial features (B_r (top two rows), B_θ (middle two rows) and B_ϕ (bottom two rows)) of PCA mode 2 for the global (1st, 3rd and 5th rows) and sub-auroral (2nd, 4th and 6th rows) grids from CHAMP data.

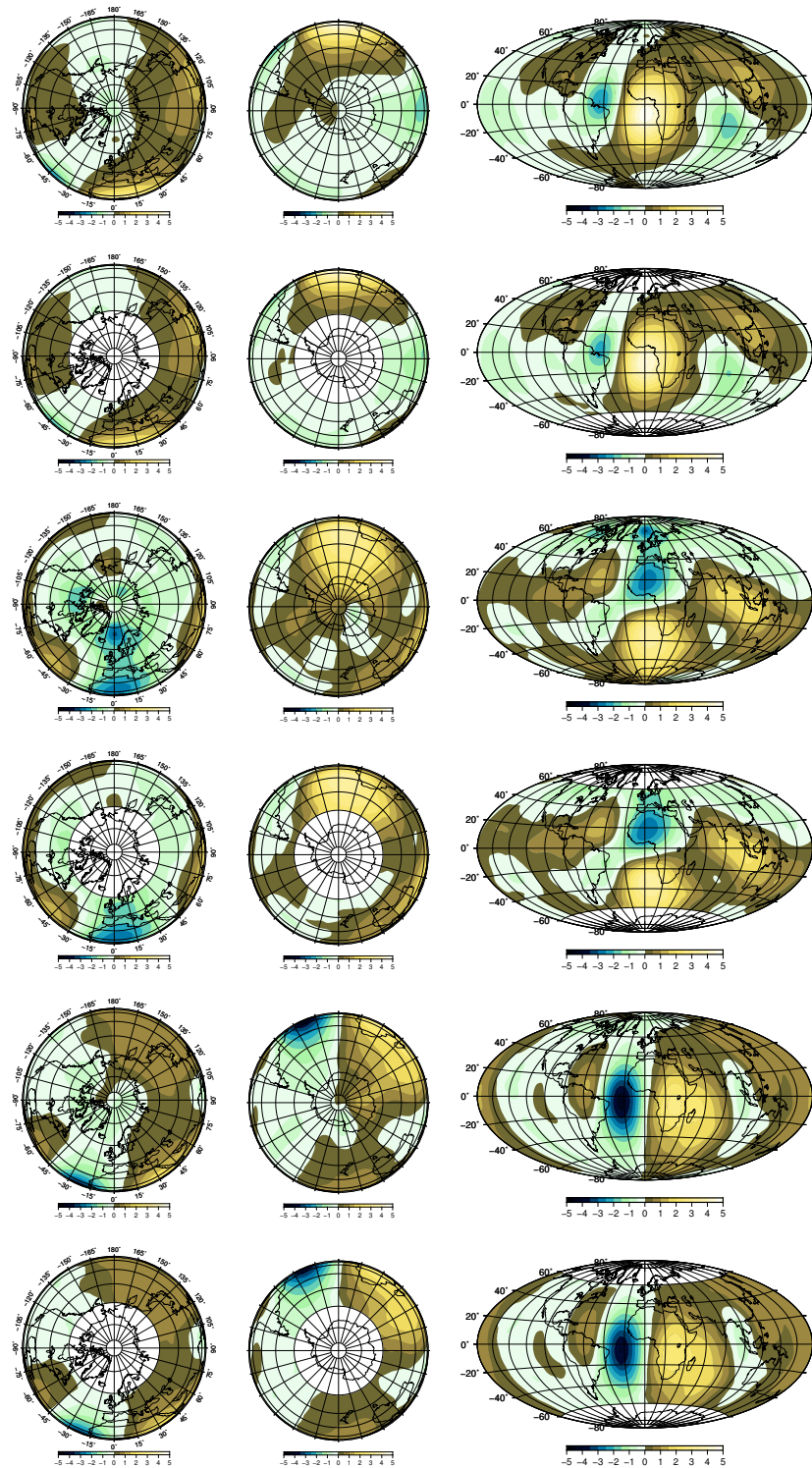


Figure B.3 – Representation of the spatial features (B_r (top two rows), B_θ (middle two rows) and B_ϕ (bottom two rows)) of PCA mode 3 for the global (1st, 3rd and 5th rows) and sub-auroral (2nd, 4th and 6th rows) grids from CHAMP data.

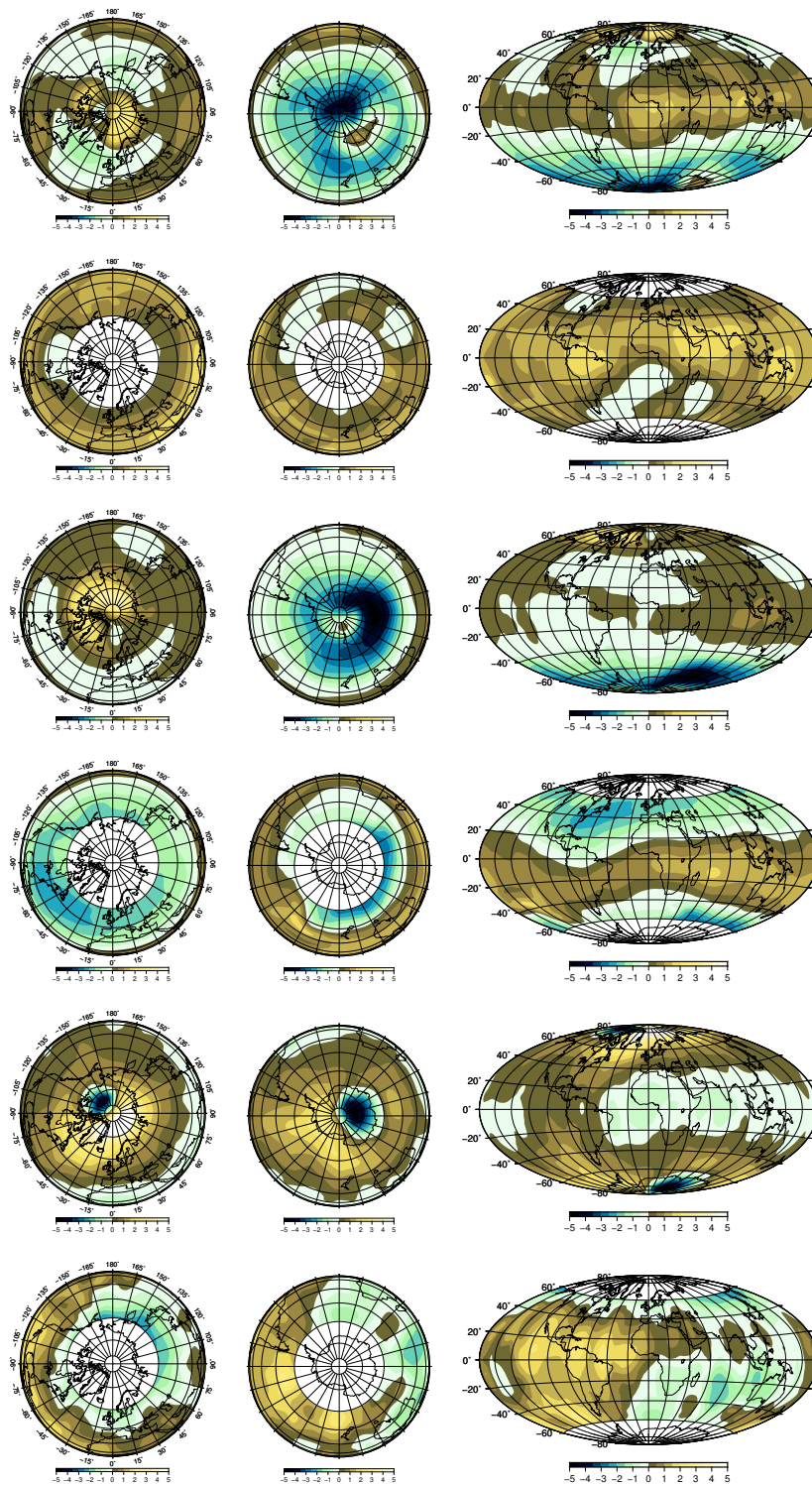


Figure B.4 – Representation of the spatial features (B_r (top two rows), B_θ (middle two rows) and B_ϕ (bottom two rows)) of PCA mode 4 for the global (1st, 3rd and 5th rows) and sub-auroral (2nd, 4th and 6th rows) grids from CHAMP data.

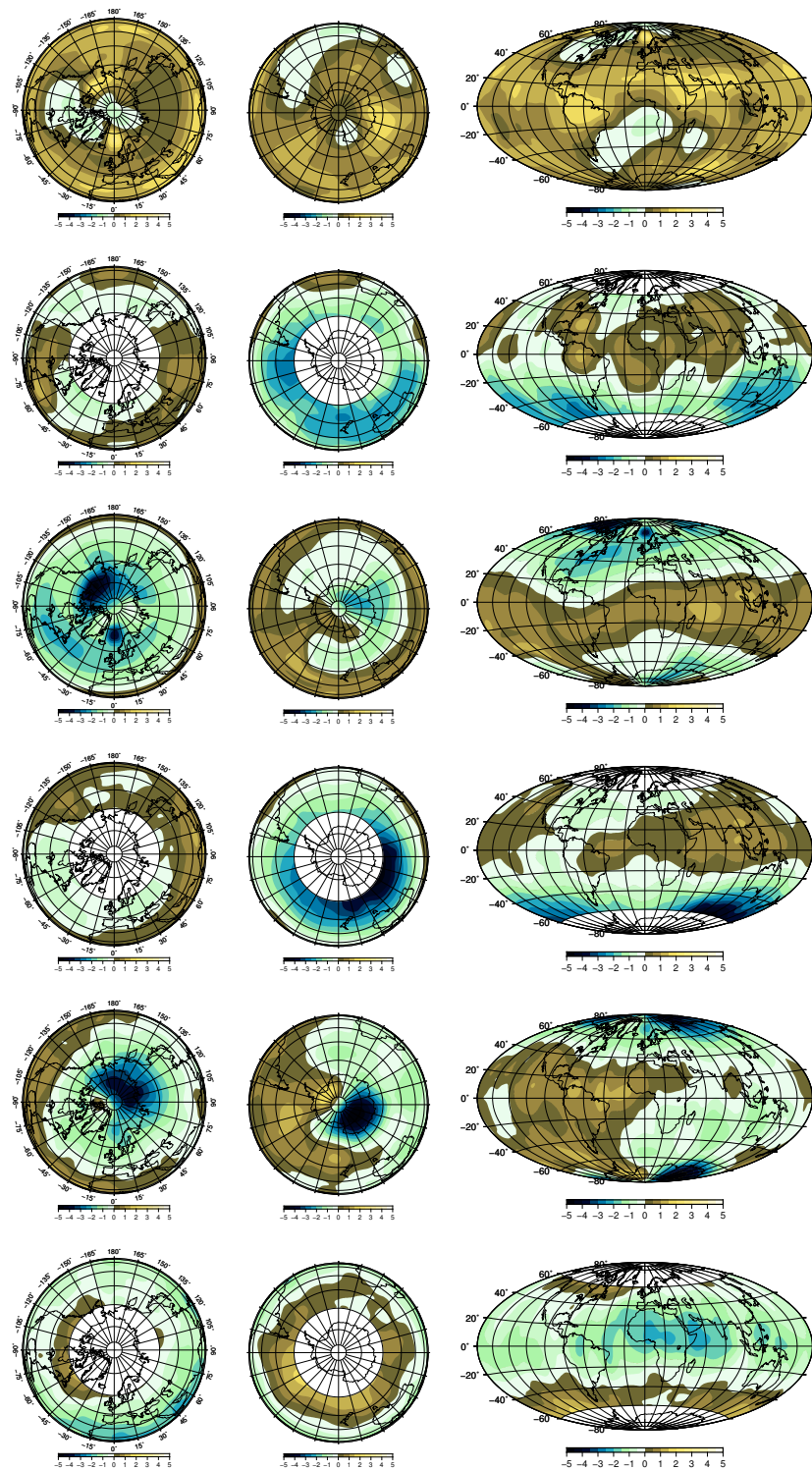


Figure B.5 – Representation of the spatial features (B_r (top two rows), B_θ (middle two rows) and B_ϕ (bottom two rows)) of PCA mode 5 for the global (1st, 3rd and 5th rows) and sub-auroral (2nd, 4th and 6th rows) grids from CHAMP data.

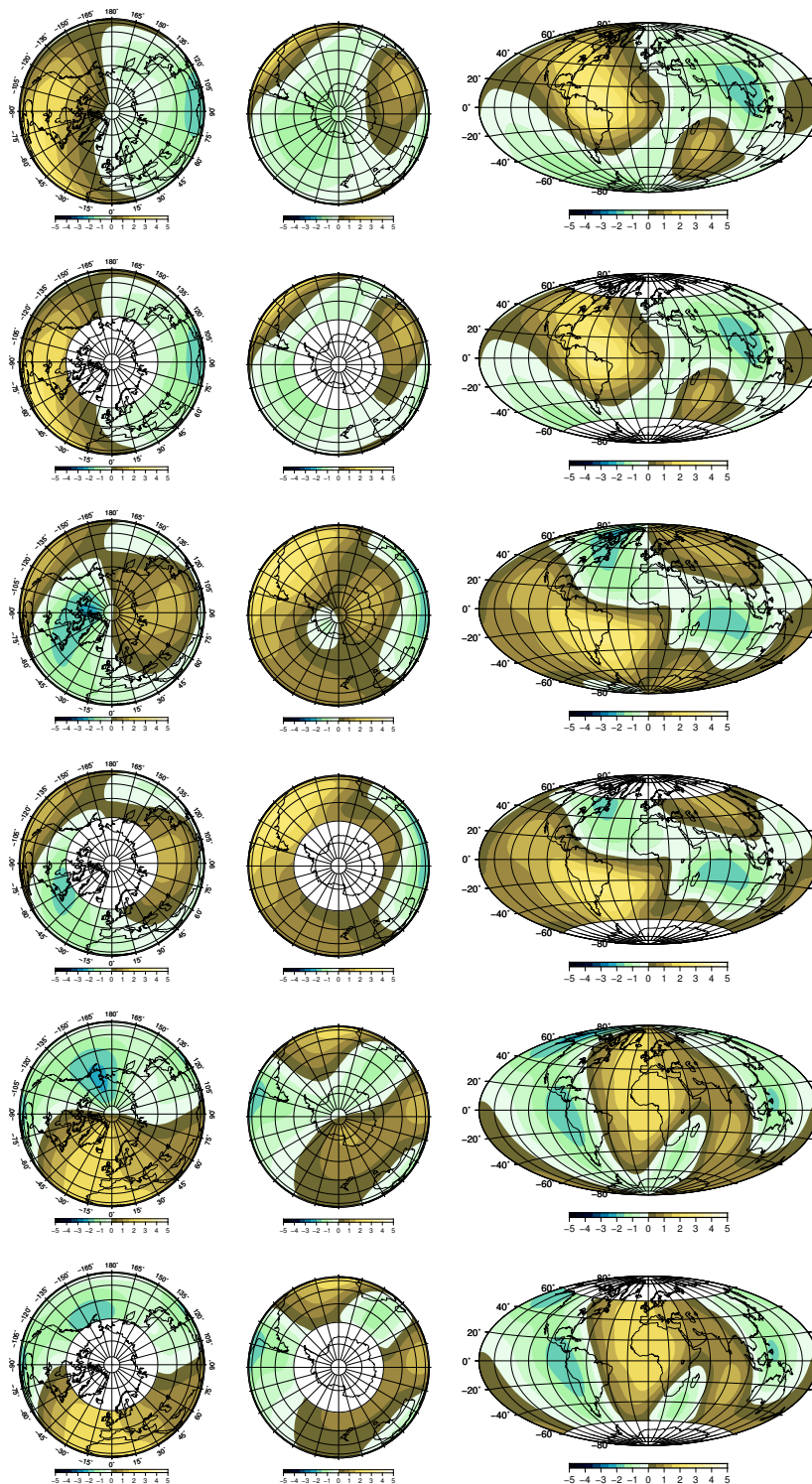


Figure B.6 – Representation of the spatial features (B_r (top two rows), B_θ (middle two rows) and B_ϕ (bottom two rows)) of PCA mode 1 for the global (1st, 3rd and 5th rows) and sub-auroral (2nd, 4th and 6th rows) grids from Swarm data.

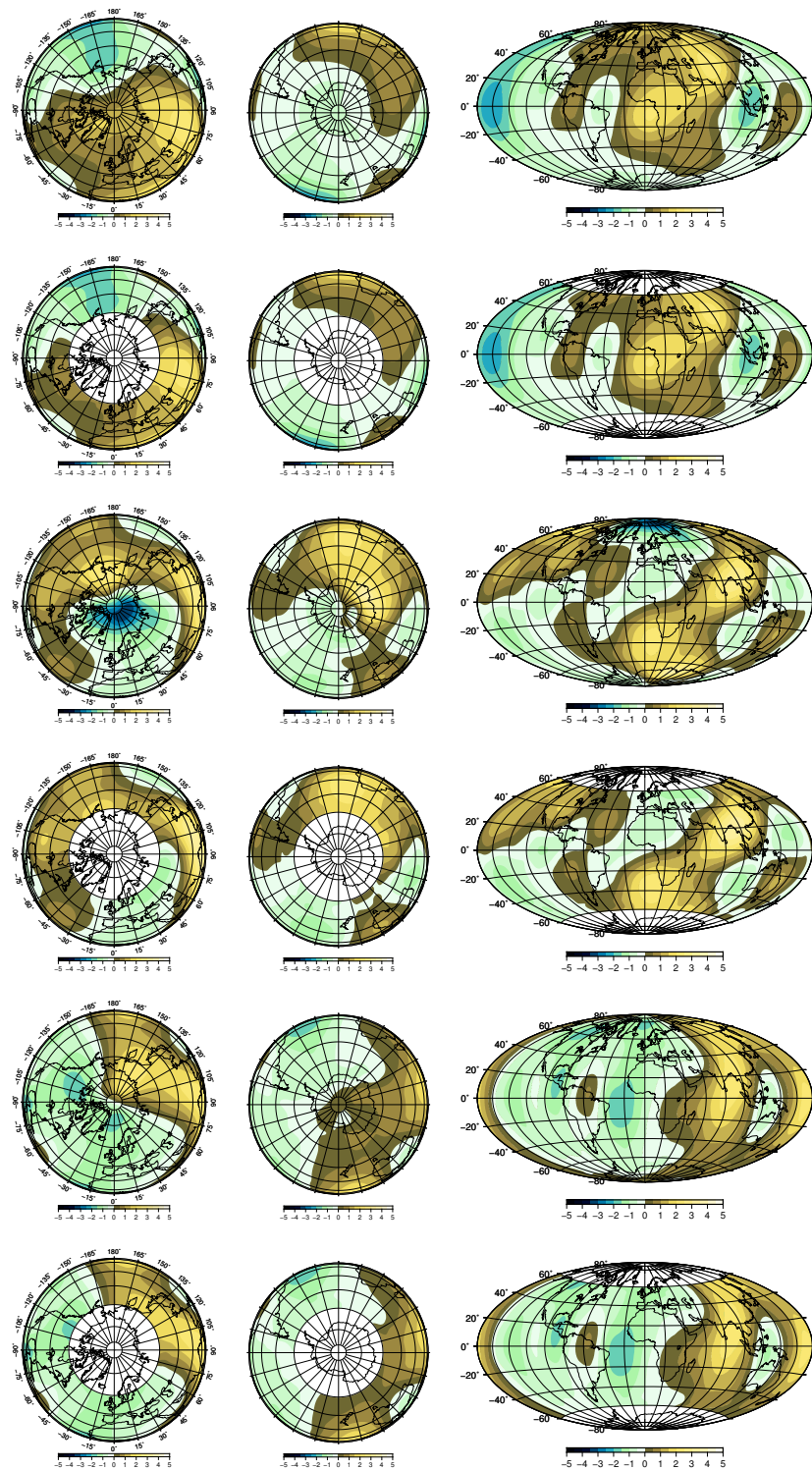


Figure B.7 – Representation of the spatial features (B_r (top two rows), B_θ (middle two rows) and B_ϕ (bottom two rows)) of PCA mode 2 for the global (1st, 3rd and 5th rows) and sub-auroral (2nd, 4th and 6th rows) grids from Swarm data.

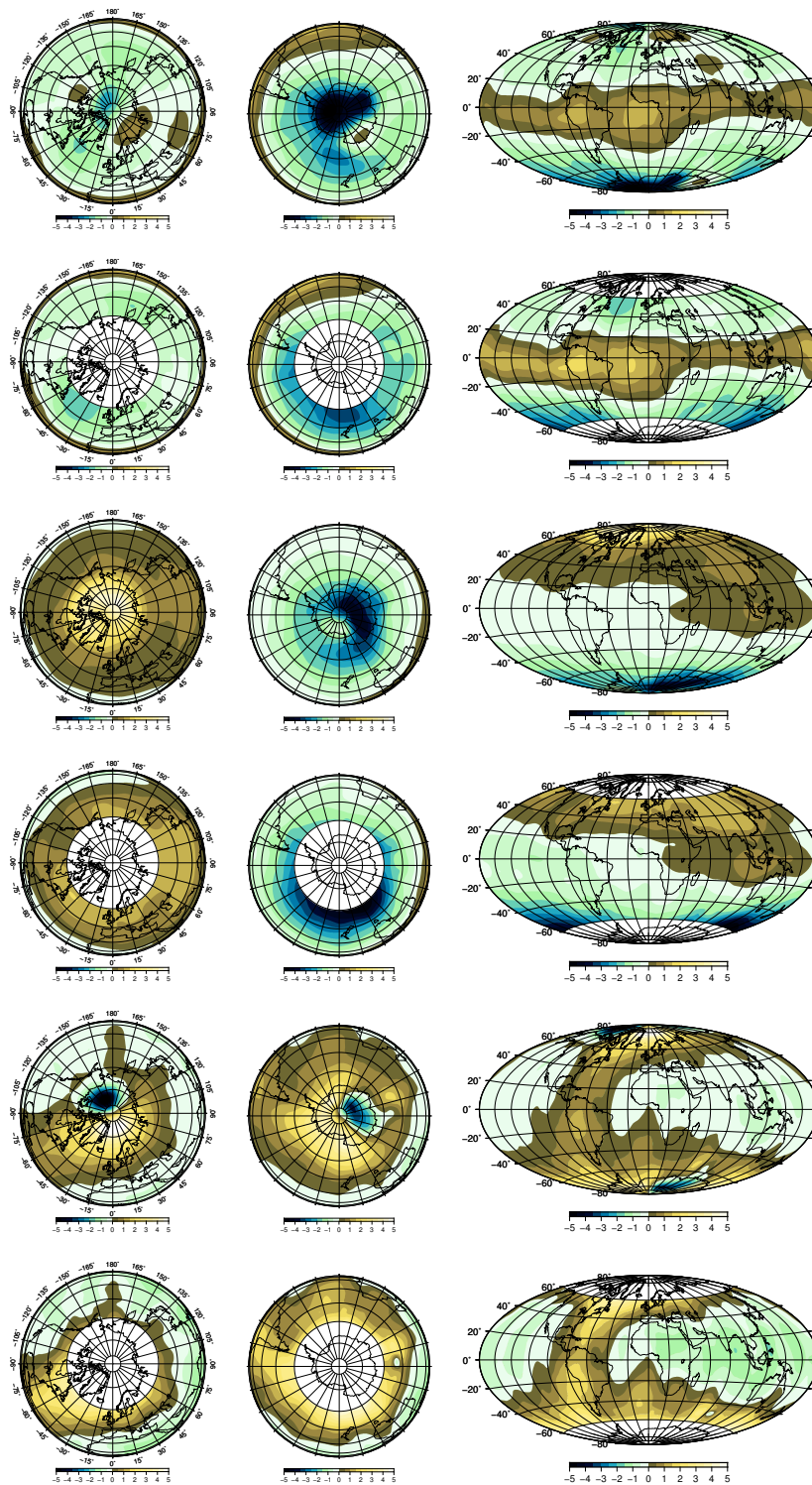


Figure B.8 – Representation of the spatial features (B_r (top two rows), B_θ (middle two rows) and B_ϕ (bottom two rows)) of PCA mode 3 for the global (1st, 3rd and 5th rows) and sub-auroral (2nd, 4th and 6th rows) grids from Swarm data.

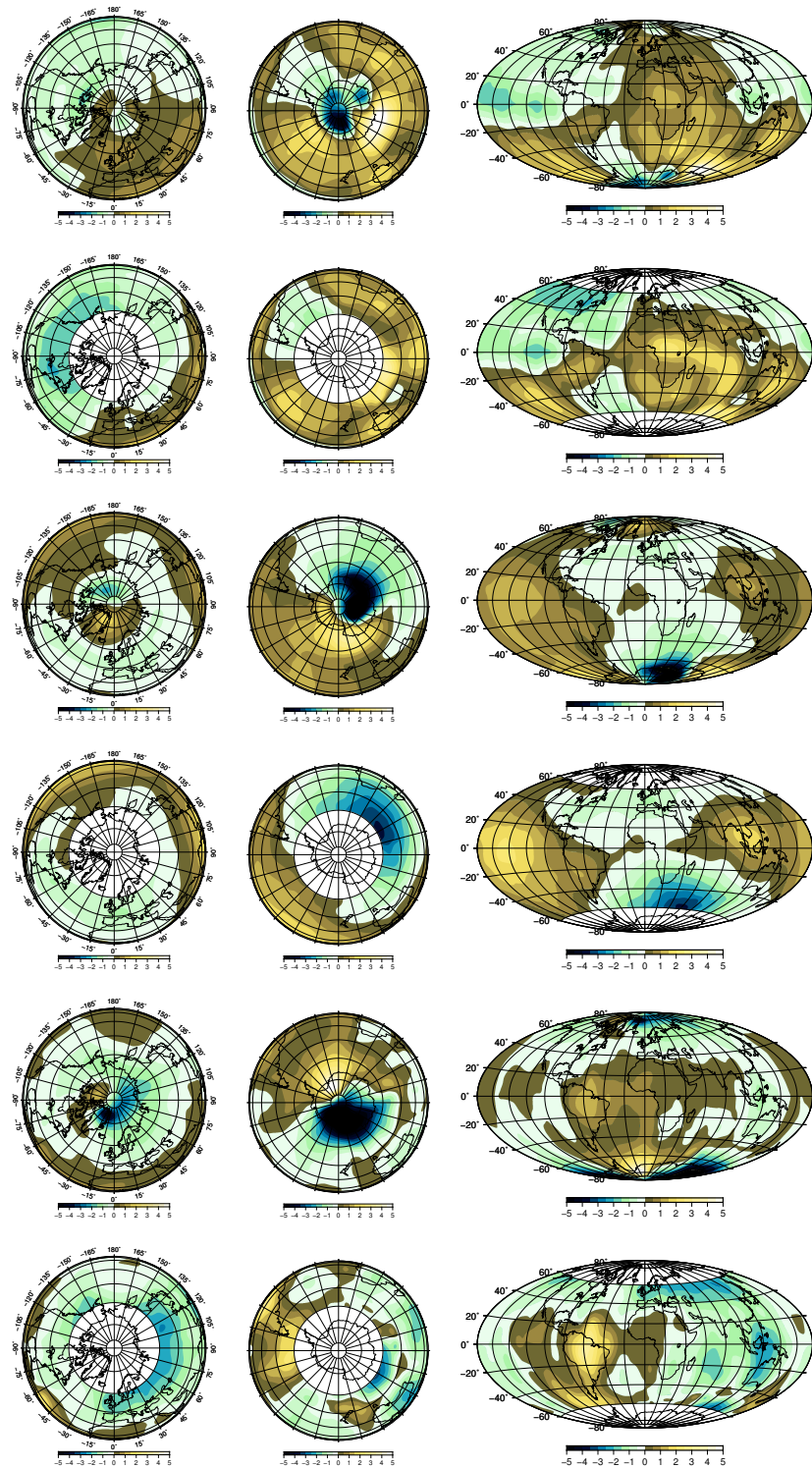


Figure B.9 – Representation of the spatial features (B_r (top two rows), B_θ (middle two rows) and B_ϕ (bottom two rows)) of PCA mode 4 for the global (1st, 3rd and 5th rows) and sub-auroral (2nd, 4th and 6th rows) grids from Swarm data.